On November 11, 1974 the $J/\Psi$ charmonium particle was discovered simultaneously on both coasts of the United States. This state is mainly built up from a charm quark and an anti-charm quark. Until then only three so-called flavors of quarks were known experimentally: up, down and strange. Since then several new charmonium resonances have been detected whose properties could mostly be accounted for by nonrelativistic potential models with a confining force. However, many of the very recent discoveries are at variance with this simplistic picture. One such example is the so-called $X$ (3872) particle. Future dedicated experiments like *PANDA* at *FAIR* in Darmstadt are expected to produce large charmonium data samples that will help to further explore the properties of old and new such states.

Quarks are an elementary building block of visible matter. They interact via the strong interaction, which is described by the theory of *Quantum Chromo Dynamics* (QCD). With the help of numerical simulations in the framework of *Lattice QCD*, i.e. QCD on a discretized spacetime, this work tries to shed light on the masses and structure of charmonium states, including the more exotic ones.

Universitätsverlag Regensburg

ISBN 978-3-86845-052-1

gefördert von:

Alumni der physikalischen Fakultät der Universität Regensburg e.V.

Universität Regensburg

Dissertationsreihe Physik - Band 14

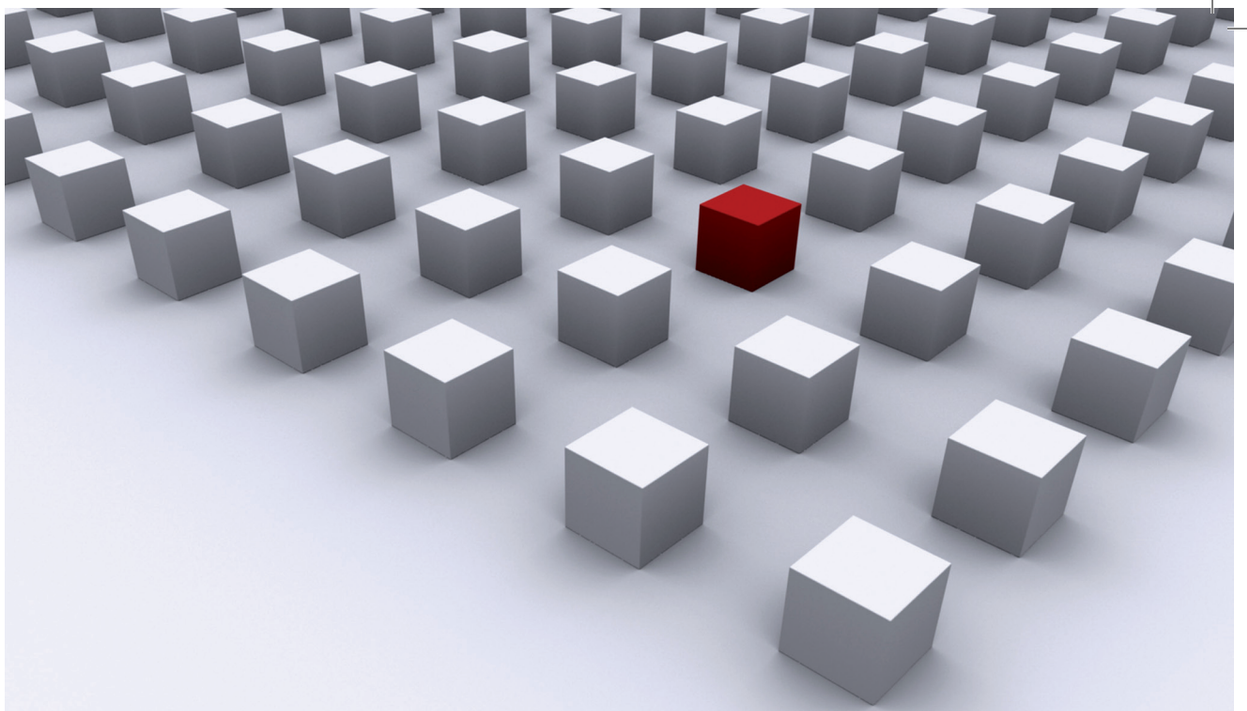

Christian Ehmann

# A Lattice QCD Calculation of the Charmonium Spectrum

Universitätsverlag Regensburg

Christian Ehmann

14

Dissertationsreihe Physik

Christian Ehmann

A Lattice QCD Calculation
of the Charmonium Spectrum

**A Lattice QCD Calculation of the Charmonium Spectrum**

Dissertation zur Erlangung des Doktorgrades der Naturwissenschaften (Dr. rer. nat.)
der naturwissenschaftlichen Fakultät II - Physik der Universität Regensburg
vorgelegt von

Christian Ehmann

aus Teublitz
Februar 2010

Die Arbeit wurde von Prof. Dr. G. Bali angeleitet.
Das Promotionsgesuch wurde am 21.09.2009 eingereicht.
Das Kolloquium fand am 15.04.2010 statt.

Prüfungsausschuss:

| | | |
|---|---|---|
| Vorsitzender: | Prof. Dr. Ch. Strunk |
| 1. Gutachter: | Prof. Dr. G. Bali |
| 2. Gutachter: | Prof. Dr. V. Braun |
| weiterer Prüfer: | Prof. Dr. M. Grifoni |


**Dissertationsreihe der Fakultät für Physik der Universität Regensburg, Band 14**

Herausgegeben vom Präsidium des Alumnivereins der Physikalischen Fakultät:
Klaus Richter, Andreas Schäfer, Werner Wegscheider, Dieter Weiss

Christian Ehmann

# A Lattice QCD Calculation of the Charmonium Spectrum

Universitätsverlag Regensburg

Bibliografische Informationen der Deutschen Bibliothek.
Die Deutsche Bibliothek verzeichnet diese Publikation
in der Deutschen Nationalbibliografie. Detailierte bibliografische Daten
sind im Internet über http://dnb.ddb.de abrufbar.

1. Auflage 2010

Leibnitzstraße 13, 93055 Regensburg

Konzeption: Thomas Geiger
Umschlagentwurf: Franz Stadler, Designcooperative Nittenau eG
Layout: Christian Ehmann
Druck: Docupoint, Magdeburg
ISBN: 978-3-86845-052-1



Weitere Informationen zum Verlagsprogramm erhalten Sie unter:
www.univerlag-regensburg.de

# A Lattice QCD Calculation of the Charmonium Spectrum


DISSERTATION ZUR ERLANGUNG DES DOKTORGRADES DER NATURWISSENSCHAFTEN (DR. RER. NAT.)
DER FAKULTÄT II - PHYSIK

DER UNIVERSITÄT REGENSBURG

vorgelegt von

Christian Ehmann

aus
Teublitz

im Jahr 2010

Promotionsgesuch eingereicht am: 21.09.2009
Die Arbeit wurde angeleitet von: Prof. Dr. G. Bali

| | | |
|---|---|---|
| Prüfungsausschuss: | Vorsitzender: | Prof. Dr. Ch. Strunk |
| | 1. Gutachter: | Prof. Dr. G. Bali |
| | 2. Gutachter: | Prof. Dr. V. Braun |
| | weiterer Prüfer: | Prof. Dr. M. Grifoni |

# Contents

*I know an eighteenth charm, and that charm is the greatest of all, and that charm I can tell no man, for a secret that no one knows but you is the most powerful secret there can ever be.*
*– American Gods*

Neil Gaiman

# 1 Introduction

Elementary particle physics is on the frontier to new grounds. The state of the art theory is the *Standard Model (SM)* of particle physics. Despite its incredible success, both qualitatively and quantitatively, the SM fails to answer some crucial open questions like the unification of the three elementary forces or the hierarchy problem, not to mention its inability to describe gravitation. Furthermore, the $CP$ violating terms included in the SM can account for only a small portion of the $CP$ violation needed to explain the observed matter-antimatter imbalance in our universe.

The upcoming results from the *Large Hadron Collider (LHC)*, especially the potential detection of the Higgs Boson, will hopefully indicate whether the SM merely needs to be expanded or completely replaced by some theory lying beyond.

Although the LHC will allow for the search of new physics at energy scales of several TeVs, there is still a sector of the SM that evades our control: the sector of strongly interacting particles, i.e. quarks and gluons. Thus, in addition to the various experiments at the LHC, there are some interesting accelerator projects in their starting phases. One example of particular relevance to the physics of charmonia is the *PANDA* experiment at the *Facility for Antiproton and Ion Research (FAIR)* in Darmstadt [1], expected to go online in 2014. One of the main programs of the PANDA collaboration is to study the spectroscopy of charmonia by investigating hadronic antiproton annihilation processes in the high energy storage ring *HESR*.

The relation between theorists working in the charm sector and future experimental projects like PANDA is a symbiotic one. Current and upcoming insights from the theory side can help to optimize the design of the detector, in return qualified results can be expected once the machine is running.

One may ask why charm physics has garnered so much interest recently. Not unlike many other cases, experimental findings have guided the way.
The first milestone of charm history was the simultaneous discovery of the $J/\Psi$ particle on November 11, 1974 on the east and west coasts of the United States [2, 3]. Although the existence and even the properties of this charmonium state, a state built up mainly from a charm-anticharm quark pair, had been predicted by theorists, the news spread like wildfire all across the physics world.
Until 1974, three kinds of quarks had appeared in experiment: up, down and strange. The materialization of the charm quark evened up the quark score, which was essential for a consistent theory of the weak interaction, and furthermore explained why neutral kaons only very rarely decay into a pair of muons. Besides filling these theoretical gaps, charmonia were hoped to, and in part did, play the same important role for understanding hadronic dynamics as the hydrogen atom played for atomic physics. Hadrons are particles made of quarks held together by the strong force, similarly to how molecules are held together by the electromagnetic force.
It is the only quark[1] with charge $+2/3$ that is both unstable and yet survives long enough to form hadronic bound states. The analysis of the properties of charmonium and of its heavier sibling, bottomonium, is directly related to the development of many methods in QCD.
After a golden age from 1974-1977, when ten charmonium resonances were discovered, interest gradually faded and the sector finally seemed to be exhausted, primarily because no new states were observed in the following two decades due to the lack of precision experiments.
The charmonium sector experienced an amazing revival in the 21st century. Since 2002 several new resonances have been detected [4, 5, 6], many of these appearing not to be mainly a conventional $c\bar{c}$ state, but to have significant contribution from hybrids or four quark (molecules/tetraquarks) configurations. In fact, some of these are exotic, implying that these states cannot be built up from a quark and an antiquark only. The most prominent example is the $X(3872)$ [7], first discovered by Belle in 2003, with a mass close to the $D\overline{D}^*$ threshold. Its inner structure is far from being understood, supposedly it receives large contributions from higher Fock states. Even its quantum numbers have not yet been pinned down. Further puzzling $X$,$Y$,$Z$-,$D_s$-,$B_c$-,

[1] Known so far.

and charmed baryon states are challenging both for experimentalists and theorists [8, 9].

Analyzing the production and decays of charmed states furthermore provides scientists with rich information about how the strong interaction manifests itself in ordinary matter [10]. For example, the fusion of two gluons in hadron-hadron interactions is the dominant process for producing charm quarks in that environment. Since this process obviously depends on the gluon distributions in the involved hadrons, a careful backtracking gives us valuable information about these universal quantities.

Especially heavy quark-antiquark bound states as multiscale systems are an ideal laboratory where our understanding of nonperturbative QCD and its interplay with perturbative QCD may be tested in a controlled framework. In the last few years a wealth of new experimental results have become available. There are several different ways charmonium states can be produced. Quarkonium researchers can rely on dedicated experiments in the most important high energy physics facilities [5].

$e^+e^-$-collisions at $\tau$-charm factories like *BES*, *CLEO/CLEO-c* or *KEDR* allow for the accumulation of very large data samples of vector states. This production mechanism is limited in the sense that other states can only be produced through decay cascades.

Experiments not bound to the $J^{PC} = 1^{--}$ channel are, amongst others, the various B-factories and *E835* at *Fermilab*. The latter one exploits the antiproton accumulator of the Tevatron to scan all known narrow charmonium states in formation from $p\bar{p}$ annihilation.

The B-factories have turned out to be an amazingly powerful and clean production machinery for a wide range of charmonium states through a rich variety of reactions like B-decays, photon-photon fusion, initial-state-radiation and the quantitatively still not fully explained phenomenon of double $c\bar{c}$ production. Prominent examples of these types of experiments are *BaBar* at *SLAC* and *Belle* at *KEK*, where most of the new charmonium resonances since 2002 have been discovered.

Other non-dedicated experiments at several facilities provide valuable information for the mechanisms of quarkonium production: e.g., gluon-gluon fusion in $p\bar{p}$ annihilation investigated by the *CDF* and *D0* experiments at the Tevatron, photon-gluon fusion in electron-proton collision investigated by *ZEUS* and *H1* experiments at *HERA*, photon-photon fusion at *LEP*, to

mention just a few.
In the quest of the nature of the very early universe, the prospering field of QCD in media relies on heavy quarkonia as a promising playground. For instance, $J/\Psi$ suppression long ago was suggested as a signal of deconfinement at high temperatures and densities [11]. The *PHENIX* and *STAR* experiments at *RHIC* or the *NA60* experiment at *CERN* exploit the charmonium production in heavy-ion collisions to achieve the desired environment.
Following this brief summary of the present experimental status and challenges, we will introduce the theoretical tools that are required to handle the experimental input. This will lead us to the method of our choice to investigate the nature of charmonium states: *Lattice Quantumchromodynamics (LQCD)* [12].

*Thank you for allowing me to use colors as rich and deep as you please... Now that I have done it, I don't think I'll ever go back.*
*– Letter to Gertrude Whitney*

Maxfield Parrish

# 2 Continuum QCD

The force responsible for the binding of a charm and an anticharm quark is the strong interaction, which is described by *Quantum Chromo Dynamics (QCD)*. This quantum field theory postulates that quarks carry an additional charge, the so-called color (*Greek: chroma*) charge, and interact via gauge bosons called gluons. Although many phenomena like confinement cannot at present be derived analytically from QCD, calculations confirm and predict experimental data to very high precision.
In the following we will address the basic principles of QCD. All formulations will be in Euclidean spacetime (see App. B.1), since this is most suitable for lattice calculations, to which we will turn later.
For a detailed account of QCD, we refer the reader to standard textbooks like [13, 14, 15, 16].

## 2.1 The QCD Action

The incredible success of *Quantumelectrodynamics (QED)*, which is based on the assumption of a local gauge symmetry, suggested to promote the same principle to a theory of the strong interaction. In the case of QCD, the symmetry group $SU(3)$ turned out to represent the known particle spectrum. The postulation of a color charge, carried by the partons inside hadrons called quarks, was necessary to explain the existence of the $\Delta^{++}$ baryon without violating the Pauli exclusion principle.
In the Eightfold Way [17] it was proposed that all physical states should be in a color-singlet, i.e. invariant under local $SU(3)$ color transformations. One consequence of promoting the $SU(3)$ symmetry to a local gauge symmetry is the existence of bosonic particles, named gluons, which mediate the

interaction between the quarks. In contrast to QED, where the photons are electrically neutral, these bosons carry color charge themselves due to the nonabelian nature of the color $SU(3)$ group. This nonlinearity of the QCD Lagrangian generates some peculiar phenomena like confinement and makes a theoretical treatment very difficult.
Actually, no single approach to solve QCD is applicable to the entire energy range of interest. Perturbative methods, for instance, become unfeasible at small momentum transfers, since the magnitude of the QCD coupling constant increases with the distance or equivalently with the inverse momentum. Nonperturbative methods like Lattice QCD can treat strong interactions at all energy scales (up to some cutoff), but introduce other difficulties as we will see later.
As a starting point we will present the QCD continuum action.
Describing both quarks and gluons, the QCD action is build up from a fermionic and a bosonic (gauge) part:

$$S_{\mathrm{QCD}} \quad = \quad S_{\mathrm{ferm}} + S_{\mathrm{gauge}} \tag{2.1}$$

### 2.1.1 The Fermion Action

Strongly interacting fermions, the quarks, are described by Dirac 4-spinors

$$\psi^f_{\alpha,c}(x),$$

that carry three different indices and depend on the spacetime position,

$$\begin{array}{cc} f & \text{flavor index } (1,...,N_f) \\ \alpha & \text{spinor index } (1,...,4) \\ c & \text{color index } (1,...,3) \\ x & \text{spacetime} \end{array}$$

$N_f$ is the number of flavors in the theory.
Quarks are in the fundamental representation of the color SU(3) group; hence, their color index runs from 1 to 3.
Antiquarks are represented by

$$\bar{\psi}^f_{\alpha,c}(x)$$

and lie in the conjugate representation.
Naively, one could build up an action from quarks and antiquarks only.

However, a dynamic theory of quark-antiquark interactions requires a kinetic term. Derivatives of the quark fields would break the local gauge invariance, unless a vector particle, the so-called gauge boson, is included.
The corresponding field is denoted by

$$A^a_\mu(x),$$

where its indices stand for

$$\begin{array}{ll} \mu & \text{Lorentz index (1,...,4)} \\ a & \text{color index (1,...,8)} \\ x & \text{spacetime} \end{array}$$

This time the color index runs from 1 to 8 because the gauge field is in the adjoint representation of the color group, which is eight-dimensional.

The task is to construct an action which is invariant under the following transformations of the fermionic fields:

$$\psi(x) \longrightarrow \psi'(x) = \Lambda^{-1}(x)\psi(x), \tag{2.2}$$
$$\bar{\psi}(x) \longrightarrow \bar{\psi}'(x) = \bar{\psi}(x)\Lambda(x), \tag{2.3}$$

where $\Lambda \in SU(3)$ is a local color transformation matrix of $SU(3)$.
These group elements can also be parametrized by introducing the generators $t_a$ (see App. B.3) of the group:

$$\Lambda(x) = e^{i\omega(x)^a t^a}. \tag{2.4}$$

$\omega(x)$ lies in the so-called Lie algebra of the group.[1]
We also demand the action to be invariant under the corresponding transformation of the gauge fields

$$A_\mu(x) \longrightarrow A'_\mu(x) = \Lambda^{-1}(x)A_\mu(x)\Lambda(x) + i\left(\partial_\mu\Lambda^{-1}(x)\right)\Lambda(x), \tag{2.5}$$

with $A_\mu(x) = gA^a_\mu(x)t_a$ . $g$ is the strong coupling constant, which determines the strength of the interaction part of the QCD Lagrangian with respect to the kinetic part.
Keeping these considerations in mind, we can write down the fermionic part

[1] Throughout the whole thesis we will use the Einstein sum convention.

of the QCD continuum action which is invariant under the simultaneous application of (2.2), (2.3) and (2.5) (and also translations/rotations)[2]:

$$S_{\text{ferm}}[\psi, \bar{\psi}, A] = \sum_f \int d^4x \bar{\psi}^f(x)\, \mathrm{D}_m^f(x)\, \psi^f(x), \tag{2.6}$$

where $\mathrm{D}_m(x)$ is the Dirac operator, which is given by

$$\mathrm{D}_m(x) = \gamma_\mu D_\mu(x) + m. \tag{2.7}$$

Here the covariant derivative

$$D_\mu(x) = \partial_\mu + iA_\mu(x). \tag{2.8}$$

appears. It is called covariant since $D_\mu(x)\psi(x)$ transforms under color rotations in exactly the same way as $\psi(x)$ does.
Let us write out (2.6) more explicitly to realize the meaning of the individual terms:

$$\begin{aligned} S_{\text{ferm}}[\psi, \bar{\psi}, A] &= \sum_f \int d^4x \\ &\quad [\bar{\psi}^f(x)\, \gamma_\mu \partial_\mu\, \psi^f(x) && (2.9)\\ &+ m^f\, \bar{\psi}^f(x)\, \psi^f(x) && (2.10)\\ &+ i\, \bar{\psi}^f(x)\, \gamma_\mu A_\mu(x)\, \psi^f(x)]. && (2.11) \end{aligned}$$

(2.9) and (2.10) represent the kinetic term, (2.11) describes the interaction between quarks and gluons. It gives rise to the $q\bar{q}g$ 3-point vertex in perturbation theory.
So we see that the necessary introduction of the gauge field automatically includes its coupling to the quarks.
However, the gluons do not only interact, but they also propagate. Therefore, we have to add a further part to our QCD action.

### 2.1.2 The Gauge Action

We are looking for a gauge invariant kinetic term for the gluons. A possible candidate is the contraction of two field strength tensors, in analogy to QED. In QED the field strength tensor is given by

$$F_{\mu\nu}^{\text{QED}}(x) = \partial_\mu A_\nu(x) - \partial_\nu A_\mu(x), \tag{2.12}$$

[2]Color and spinor indices are suppressed for the sake of clarity.

where $A\mu$ now stands for the photon field.
This can also be written in terms of covariant derivatives:

$$F_{\mu\nu}^{\mathrm{QED}}(x) \quad = \quad -i\,[D_\mu(x), D_\nu(x)]\,. \tag{2.13}$$

If we generalize this to QCD, we obtain:

$$\begin{aligned} F_{\mu\nu}(x) &= -i\,[D_\mu(x), D_\nu(x)] \\ &= [\partial_\mu A_\nu^a(x) - \partial_\nu A_\mu^a(x) - f^{abc} A_\mu^b(x) A_\nu^c(x))]t^a. \end{aligned} \tag{2.14}$$

As a commutator of two covariant derivatives, it is clear that $F_{\mu\nu}(x)$ transforms under (2.5) as

$$F_{\mu\nu}(x) \quad \longrightarrow \quad F'_{\mu\nu}(x) \quad = \quad \Lambda(x)\, F_{\mu\nu}(x)\, \Lambda^{-1}(x). \tag{2.15}$$

Thus we contract two field strength tensors to maintain Lorentz symmetry and take the trace to preserve gauge symmetry, as the trace is invariant under cyclic permutations. With a suitable prefactor we obtain our final gauge action:

$$S_{\mathrm{gauge}}[A] \quad = \quad -\frac{1}{2g^2} \int d^4x\, \mathrm{Tr}\,[F_{\mu\nu}(x)\, F_{\mu\nu}(x)]\,. \tag{2.16}$$

If we compare (2.12) and (2.14), we see that, due to the noncommuting nature of the generators of the $SU(3)$, we have an additional term in the QCD field strength tensor. This term is of utmost importance, since it leads to three and four gluon interactions. Far ranging consequences are that QCD is an asymptotically free theory and that quarks and gluons are confined.
Of course one could imagine including further terms in the action, but they are forbidden by either restrictions of dimensionality or of symmetries, e.g. Lorentz symmetry or parity, or they complicate our theory unnecessarily[3]. In fact, if we require renormalizability, than $F^{\mu\nu}F_{\mu\nu}$ and $F^{\mu\nu}\widetilde{F}_{\mu\nu}$ are the only possibilities. The latter one violates $CP$, but why it is so small is a mystery (strong $CP$ problem, see for instance [18]).

## 2.2 Symmetries

Besides the local color $SU(3)$, the QCD action exhibits further interesting global symmetries.

[3] This does not hold for a theory in discrete spacetime. As we will see later on, additional terms can help to reduce discretization errors, for instance.

### 2.2.1 Flavor Symmetry

The strong interaction is flavor blind, it distinguishes the quark flavors only by their different masses. Thus if all quark masses were identical, rotations in flavor space would not change the QCD action. For up and down quarks this holds reasonably well, resulting in a $SU(2)$ flavor symmetry, also called isospin symmetry. Assuming the strange quark mass to be degenerate, too, leads to a $SU(3)$ flavor symmetry, which helps to explain hadronic spectra through its multiplets. For $N_f$ degenerate quark masses, the QCD Lagrangian is invariant under the following global vector transformations:

$$\psi_f \to \psi'_f = e^{i\alpha^a t^a_{ff'}}\psi_{f'} \ , \qquad \overline{\psi}_f \to \overline{\psi}'_f = \overline{\psi}_{f'} e^{-i\alpha^a t^a_{ff'}} \ , \tag{2.17}$$

$$\psi_f \to \psi'_f = e^{i\alpha^0 \mathbb{1}_{ff'}}\psi_{f'} \ , \qquad \overline{\psi}_f \to \overline{\psi}'_f = \overline{\psi}_{f'} e^{-i\alpha^0 \mathbb{1}_{ff'}} \ , \tag{2.18}$$

where the coefficients $\alpha^a$ are real, space-time independent angles.

### 2.2.2 Chiral Symmetry and its Spontaneous Breaking

Let us define the chirality of a quark by introducing the following projectors:

$$P_\pm = \frac{1}{2}(\mathbb{1} \pm \gamma_5) = P_{\mathrm{L,R}} \text{ with } P_\pm^2 = P_\pm \ , \ P_+P_- = P_-P_+ = 0 \ , \ P_+ + P_- = \mathbb{1} \ . \tag{2.19}$$

By applying these projectors to a quark field, we obtain the left- and right-handed components, respectively:

$$\psi_{\mathrm{L,R}} = P_{\mathrm{L,R}}\psi \qquad \text{with} \qquad \gamma_5\psi_{\mathrm{L,R}} = \pm\psi_{\mathrm{L,R}} \ . \tag{2.20}$$

The chiral transformations are defined as follows:

$$\psi_f \to \psi'_f = e^{i\gamma_5\beta^a t^a_{ff'}}\psi_{f'} \ , \qquad \overline{\psi}_f \to \overline{\psi}'_f = \overline{\psi}_{f'} e^{i\gamma_5\beta^a t^a_{f'f}} \ , \tag{2.21}$$

$$\psi_f \to \psi'_f = e^{i\gamma_5\beta^0 \mathbb{1}_{ff'}}\psi_{f'} \ , \qquad \overline{\psi}_f \to \overline{\psi}'_f = \overline{\psi}_{f'} e^{i\gamma_5\beta^0 \mathbb{1}_{f'f}} \ , \tag{2.22}$$

where the coefficients $\beta^a$ are again real, spacetime independent angles.
The difference between these transformations and the flavor transformations in (2.17) and (2.18), respectively, is the $\gamma_5$ appearing in the exponent.
Obviously, these transform left- and right-handed components differently. If the fermion action anticommutes with $\gamma_5$,

$$\{\mathrm{D}_m(x), \gamma_5\} \ = \ 0, \tag{2.23}$$

than $\mathrm{D}_m(x)$ is invariant under the chiral rotations. This only holds for $m = 0$, since a mass term would allow left- and right-handed components to mix.
Thus in the chiral limit, i.e. when all quark masses vanish, we have an additional global symmetry called chiral symmetry:

$$U(N_f)_\mathrm{L} \times U(N_f)_\mathrm{R} = U(N_f)_\mathrm{V} \times U(N_f)_\mathrm{A} \ , \tag{2.24}$$

equivalent to

$$SU(N_f)_\mathrm{V} \times U(1)_\mathrm{V} \times SU(N_f)_\mathrm{A} \times U(1)_\mathrm{A} \ . \tag{2.25}$$

For arbitrary masses the $U(1)_V$ symmetry still holds and one can easily show that its conserved quantity is the baryon number $\mathcal{B}$. One of the consequences of this is that there is no proton decay into leptons within the standard model.
Although the classical Lagrangian exhibits the full symmetry in (2.25), one finds that in the fully quantized theory the $U(1)_\mathrm{A}$ is explicitly broken due to the chiral (or Adler-Bell-Jackiw) anomaly. This anomaly is due to the non-invariant fermion integration measure in the path integral (see next section). So the chiral symmetry reduces to

$$SU(N_f)_\mathrm{V} \times U(1)_\mathrm{V} \times SU(N_f)_\mathrm{A} \ . \tag{2.26}$$

However, it turns out that the remaining $SU(N_f)_\mathrm{A}$ is also broken, due to a non-vanishing chiral condensate $\langle\overline{\psi}\psi\rangle \neq 0$ . Although this is a quantum symmetry of the action, it does not hold for the non-perturbative ground state. In this context one speaks of spontaneous breaking of a global symmetry. The order parameter for the spontaneous breaking of chiral symmetry is the chiral condensate, which is not invariant under chiral transformations. The spontaneous breaking of a continuous global symmetry is always accompanied by the appearance of so-called *Nambu-Goldstone Bosons* [19]. Each generator of the symmetry group broken by the vacuum state results in a Goldstone Boson. For $N_f = 2$ these are identified with the pion triplet. Because $U(1)_\mathrm{A}$ is broken explicitly, it is no symmetry to start with and consequently the $\eta$ meson, which represents the corresponding flavor singlet state, is no Goldstone Boson. In fact, the pion is not exactly massless due to the finite quark masses, but its mass is significantly smaller than those of other mesons, leading to the term *Pseudo-Goldstone Bosons*.

We will see that realizing exact chiral symmetry on the lattice even in the case $m = 0$ is complicated.

## 2.3 The Path Integral Formalism

The classical field theory can be quantized in a canonical approach by promoting the fields $\bar{\psi}$, $\psi$ and $A_\mu$ to operators and imposing appropriate commutation relations.
A different formalism, which is more suitable for non Abelian quantum field theories and the lattice formulation, is quantization by functional methods. In this formalism the expectation value of an observable $\mathcal{O}$ can be expressed as a Feynman path integral

$$\langle \mathcal{O}[\psi, \bar{\psi}, A] \rangle = \frac{1}{Z} \int [d\psi][d\bar{\psi}][dA] \mathcal{O}[\psi, \bar{\psi}, A] \exp(-S[\bar{\psi}, \psi, A]), \tag{2.27}$$

with the partition function

$$Z = \int [d\psi][d\bar{\psi}][dA] \exp(-S[\bar{\psi}, \psi, A]). \tag{2.28}$$

The integration measures are formally defined as

$$\begin{aligned} [d\psi] &= \prod_{f,c,\alpha} \prod_{x \in \mathbb{R}^4} d\psi_{f\,(\alpha,c)}(x), \\ [d\bar{\psi}] &= \prod_{f,c,\alpha} \prod_{x \in \mathbb{R}^4} d\bar{\psi}_{f\,(\alpha,c)}(x), \\ [dA] &= \prod_{a,\mu} \prod_{x \in \mathbb{R}^4} dA^a_\mu(x). \end{aligned} \tag{2.29}$$

(2.27) is a weighted average of the observable over all possible paths, or, in quantum field theory, over all possible field configurations with the weighting factor being the exponent of the negative action. Configurations with minimal action consequently contribute most to the path integral.
Unfortunately, this integral cannot be solved analytically, however, one can try to find a "good" approximation.
One possibility is to look for some small parameter, one can expand in, and treat the corresponding terms in the Lagrangian as perturbations. The most obvious parameter is the coupling constant $g$, appearing in the quark-gluon and also in the three- and four-gluon interactions[4]. The renormalized

[4] Remember that we defined $A_\mu(x) = g A^a_\mu(x) t_a$.

coupling constant depends on the energy scale of the process under consideration and it can be shown that only for sufficiently large scales its value is small enough for the perturbation theory to work. This phenomena is known as *asymptotic freedom*.
Other approaches to tackle QCD are lattice calculations, sum rules, the large $N_c$ expansion, potential models or effective theories. Examples for the last method are *Chiral Perturbation Theory ($\chi PT$)* [20], if one is interested in the light quark regime, or *Non-Relativistic QCD (NRQCD)* [21] or *Heavy Quark Effective Theory (HQET)* [22], if heavy quarks are involved.

## 2.4 Hadron Structure

Nature only allows color singlet states, since these are the only finite energy states[5]. The constituent quarks in a group cannot be separated from their parent hadron, and this is why quarks can never be studied or observed in any direct way but only within hadronic bound states. This phenomenon widely known as confinement still has not been rigorously proven, starting from QCD. Some intuitive approaches suggest the existence of a gluonic flux tube between two quarks, binding them together. The color force remains constant, regardless of their distance from each other. However, if the two quarks become sufficiently separated, as happens in high energy collisions for instance, the string rips and an additional quark-antiquark pair is created from the vacuum.
There are infinitely many ways to construct a color singlet state by combining quarks and gluons, and consequently hadrons exhibit complex inner structure. One goal of this work is to grasp at least a few possible combinations.
Let us regard the easiest example: piecing together a quark and an antiquark.
In the language of group theory, we have to build a tensor product of the fundamental and conjugate representations. The resulting product can then be reduced to other irreducible representations:

$$3 \otimes \bar{3} \quad = \quad 1 \oplus 8. \tag{2.30}$$

[5] At least in the confined phase. In the deconfined phase a quark-gluon plasma prevails, where the mesons and baryons dissolve into a fluid of quarks and gluons.

We see that even for this simple combination we obtain a singlet. This represents a contribution to the wavefunction of a meson state.
What about the octet? Combining this octet with an octet representing a gluon, we get a further physical state:

$$8 \otimes 8 \quad = \quad 1 \oplus 8 \oplus 8 \oplus 10 \oplus \overline{10} \oplus 27 \tag{2.31}$$

Again, we spot an octet after the reduction. Therefore, by successively adding an octet to the octet obtained by (2.30) one can always form a singlet state:

$$3 \otimes \bar{3} \otimes 8 \otimes \ldots \otimes 8 \quad = \quad 1 \oplus \ldots \quad . \tag{2.32}$$

Such mesonic states with valence gluons are called hybrid mesons, but they represent only some possible configurations of a physical meson state. They are built up of a quark, an antiquark and a gluonic excitation. The term "constituent glue" is also commonly used, meaning that the gluonic content as a whole contributes to the overall quantum numbers of the hybrid.
One can think of many more higher Fock state contributions to a meson like a tetra quark or molecule state, which both contain two quarks and two antiquarks. In the first one the quarks form a color singlet as a whole, whereas a molecule in the sense of QCD is an object built from two weakly bound mesons.
Since gluons carry color charge, a state without any valence quark content is possible. These so-called glueballs only consist of gluonic excitations and represent interesting probes for investigating the strong interaction.
The important point is now that as long as all these different configurations exhibit the same quantum numbers, they are allowed to mix with each other. Let us consider a physical state like the pion, which looks rather trivial at first sight. In many textbooks the pion singlet wavefunction is given by[6]:

$$|\pi_0\rangle \quad = \quad \frac{1}{2}(|u\bar{u}\rangle - |d\bar{d}\rangle) \tag{2.33}$$

That is only part of the truth, reality is far more complex.
The pion as a pseudoscalar state has $J^{PC} = 0^{-+}$, isospin $I = 1$, $I_3 = 0$, strangeness, charm, topness and bottomness $S = C = B = T = 0$, and principle quantum number $n = 1$. All Fock states with the same quantum

[6]For simplicity any Gamma structure is omitted.

numbers[7] can contribute to the pion wavefunction:

$$|\pi_0\rangle \;=\; \frac{1}{\mathcal{N}}\left(C_1|u\bar{u}\rangle + C_2|uG\bar{u}\rangle + C_3|(u\bar{u}u\bar{u})\rangle + \ldots\right) \qquad (2.34)$$

and the same for the down quark. Furthermore Fock states containing both up- and down-quarks, like $u\bar{d}d\bar{u}$ are possible. For $I = I_3 = 0$ also mixing with glueballs is allowed.

But again, this is not the end of the story. First of all, we did not specify the localization of the partons. In fact, we have to integrate over all possible spacetime configurations. Then, are the quarks/gluons in a S-wave or do they have nonzero relative angular momenta? What inner spin structure do they exhibit? And so on, we could continue this list ad infinitum.

Furthermore, we still have not taken the contributions from other flavors into account. Although the quark masses differ by a significant amount (except for up and down) and hence mixing is suppressed, one *a priori* cannot neglect these contributions without running the risk of missing a relevant part of the physical state. Later on we will in fact extensively address the case of charmonia mixing with light mesons and charm-light molecule states.

Summing up, we see that the distinction between eigenstates of the strong interaction like the pion and of "partonic" Fock states, like $q\bar{q}$, which can be represented with appropriate interpolating operators, is crucial.

In this context we want to make a remark on the common nomenclature of states. Consider a certain meson channel, $J^{PC} = 0^{-+}$ for instance. One will encounter a tower of states in this channel and we can order them by their masses, starting with the lowest one. Historically motivated we want to call the groundstate $\pi(1S)$. The 1S designation is according to atomic physics and indicates that the quarks are in a relative S-wave and in the lowest radial vibration mode. However, after the above discussion we know that this is quite imprecise. The $\pi(1S)$ most likely contains nonzero contributions from quark pairs in 2S, 3S, ..., 1P, 2P, ..., higher Fock states, including hybrids, tetraquarks, etc. As long as they obey the condition to have quantum numbers $J^{PC} = 0^{-+}$, they will contribute. The reason, why the lowest lying state is indexed with "1S", is the assumption that the expansion of the groundstate in parton Fock states is dominated by the quark-antiquark pair being in a 1S configuration, i.e. this part of the wavefunction has the largest coefficient in front. The same holds for hybrids, for example. Although the

[7] In general these are no eigenstates of the full QCD action.

coefficient of $qG\bar{q}$ dominates, also $q\bar{q}$ in a 1S configuration etc. can appear in their wavefunctions.
The issue simplifies for so-called exotic states. These are states whose quantum numbers cannot be obtained by the combination of a quark and an antiquark and thus only higher Fock states are allowed to contribute.

*The existing scientific concepts cover always only a very limited part of reality, and the other part that has not yet been understood is infinite.*
*– Physics and Philosophy*

Werner Heisenberg

# 3 Lattice QCD

In this chapter we will introduce the lattice as a regulator of our theory. First, we show how to discretize the QCD continuum action and what problems arise thereby. Since the discretization procedure is not unambiguous, it is necessary to specify our way of implementation. Finally, the calculation of observables on the lattice is addressed.

When describing space and time as a continuum, certain quantum mechanical constructions are ill defined. This issue becomes obvious in perturbation theory. In calculations beyond tree level one encounters divergent momentum integrals due to ultraviolet virtual particles. In order to handle these infinite parts, a regularization scheme is introduced. The most popular regularization scheme is dimensional regularization, where the spacetime dimension $d = 4$ is modified to $d = 4 - \epsilon$. At the end of the calculation, thanks to renormalizability [23], all divergent parts inherent in poles $\sim 1/\epsilon$ can be absorbed in physical parameters like the quark mass or the coupling constant[1]. One nice thing about dimensional regularization is that it preserves all symmetries of the action. Other possibilities are Pauli-Villars-regularization or the above mentioned momentum cutoff.

Closely related to the last one is the introduction of a discrete spacetime. Realization by a lattice with spacing $a$ as a regulator only allows for fluctuations with a wavelength larger than $a$ and thus caps the possible momenta. All the continuum regularization schemes are based on the Feynman diagram expansion of a given process. To go beyond this diagrammatic approach, a nonperturbative cutoff is necessary. The lattice regularization, as the only known non-perturbative regularization, takes place before any expansion or

[1] Due to this, the coupling constant is actually not constant, but depends on the respective scale.

approximation has begun. Renormalizability on the lattice is equivalent to the existence of a continuum limit.
A very useful, and for our purposes crucial, feature of this approach is the fact that we can implement it on computers. Limiting the degrees of freedom to a finite number makes the theory accessible to binary computations.
In the following, the idea of putting QCD on a finite lattice is discussed in detail, based on textbooks like [24, 25, 26, 27].

## 3.1 Discretization of the QCD Action

First of all we discretize the continuous four-dimensional spacetime. To do so, a hypercubic lattice is introduced, see Fig. 3.1.
The coordinates are given by

$$x = a \begin{pmatrix} n_1 \\ n_2 \\ n_3 \\ n_4 \end{pmatrix}, \; n_\mu = 0, 1, \ldots, L_\mu - 1, \tag{3.1}$$

where $a$ is the lattice spacing. The topology is the one of a four dimensional torus.
The lattice points are called sites. We make the fermion fields live on them:

$$\psi(na) \equiv \psi(x),$$

where $n$ denotes a discrete spacetime vector.
Since gauge invariance should be conserved on the lattice, gauge fields are needed too. However, on the lattice they are not part of the $su(3)$ algebra (see (B.3)), but group valued:

$$U_\mu(x) = e^{iaA^a_\mu(x)t^a} \in SU(3). \tag{3.2}$$

These so-called *link variables* are located between the sites.
Under (2.5) they transform like

$$U_\mu(x) \rightarrow \Lambda(x) U_\mu(x) \Lambda^{-1}(x + a\hat{\mu}), \tag{3.3}$$

where $\Lambda(x)$ is an element of the group and the hat denotes a unit vector.
Next we discuss the fermionic lattice action and thereby we will see which complications arise and how the link variables come into play.

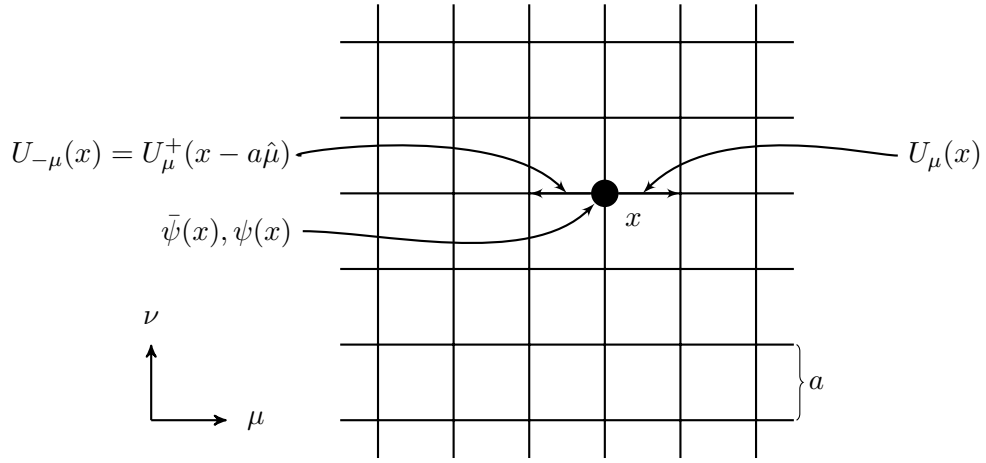


Figure 3.1: On the lattice the fermion fields $\bar{\psi}(x)$ and $\psi(x)$ live on the sites of a hypercubic lattice. The gluonic degrees of freedom, represented by the link variables $U_\mu(x)$, live on the links connecting the sites. Here we show the $\mu$-$\nu$-plane of the lattice. The separation of the sites is given by the lattice spacing $a$.

### 3.1.1 Dirac Fields on the Lattice

As a first try we discretize the Dirac action neglecting the gauge fields.
Integrals are replaced by sums and derivatives by finite (symmetric) differences:

$$\int d^4x \quad \longrightarrow \quad a^4 \sum_x \qquad \text{and} \tag{3.4}$$

$$\partial_\mu \psi(x) \quad \longrightarrow \quad \frac{\psi(x + a\hat{\mu}) - \psi(x - a\hat{\mu})}{2a}. \tag{3.5}$$

The symmetric form of (3.5) reduces discretization errors.
Equipped with this foundation we go about discretizing the naive fermion action:[2]

$$S_{\text{ferm}}[\psi, \bar{\psi}] \quad = \quad \int d^4x \, \bar{\psi}(x) \left(\gamma_\mu \partial_\mu + m\mathbb{1}\right) \psi(x) \tag{3.6}$$

$$\longrightarrow \quad a^4 \sum_x \left( \bar{\psi}(x) \sum_{\mu=1}^{4} \gamma_\mu \frac{\psi(x + a\hat{\mu}) - \psi(x - a\hat{\mu})}{2a} + \bar{\psi}(x)\, m\mathbb{1}\, \psi(x) \right)$$

[2]For convenience we assume only one flavor.

$$= \quad a^4 \sum_{x,y} \bar{\psi}(x) \mathrm{D}_{\mathrm{naive}}(x,y) \psi(y),$$

with

$$\mathrm{D}_{\mathrm{naive}}(x,y) \quad = \quad \sum_{\mu=1}^{4} \gamma_\mu \frac{\delta_{x+a\hat{\mu},y} - \delta_{x-a\hat{\mu},y}}{2a} + m\mathbb{1}\delta_{x,y}. \tag{3.7}$$

The sums $\sum_{x,y}$ run over all lattice points. $\mathbb{1}$ represents a unit matrix in Dirac space.
In the limit $a \to 0$ the continuum action is restored.

### 3.1.2 The Doubling Problem

Superficially all seems fine so far. However, there is a serious problem with this naive discretization, which can be seen most easily by regarding the quark propagator.
The propagator in coordinate space is simply given by the inverse of the Dirac operator:

$$\langle\, \bar{\psi}(x)\psi(y) \,\rangle \quad = \quad \mathrm{D}^{-1}_{\mathrm{naive}}(x,y), \tag{3.8}$$

where we use the Euclidean versions of the $\gamma$-matrices (see App. B.2).
To make things easier, we Fourier transform the Dirac operator to momentum space, where it becomes diagonal. Then the inversion is trivial.

$$\begin{aligned}
\tilde{\mathrm{D}}'_{\mathrm{naive}}(p,q) &= a^8 \sum_{x,y} e^{-ip\cdot x} \mathrm{D}_{\mathrm{naive}}(x,y) e^{iq\cdot y} \\
&= a^8 \sum_{x} e^{-i(p-q)\cdot x} \left( \sum_{\mu} \gamma_\mu \frac{e^{iq_\mu a} - e^{-iq_\mu a}}{2a} + m\mathbb{1} \right) \\
&= a^4\, \delta_{p,q}\, V \left( \frac{i}{a} \sum_{\mu=1}^{4} \gamma_\mu \sin(q_\mu a) + m\mathbb{1} \right),
\end{aligned} \tag{3.9}$$

where $V = L_1 L_2 L_3 N_t$ is the overall number of sites. By absorbing the prefactors and keeping in mind that $\tilde{\mathrm{D}}'_{naive}(p,q)$ is diagonal, we may redefine the Dirac operator in momentum space:

$$\tilde{\mathrm{D}}_{\mathrm{naive}}(q) \quad = \quad m\mathbb{1} + \frac{i}{a} \sum_{\mu=1}^{4} \gamma_\mu \sin(q_\mu a). \tag{3.10}$$

The inversion gives

$$\tilde{\mathrm{D}}^{-1}_{\mathrm{naive}}(q) \;=\; \frac{m\mathbb{1} - ia^{-1}\sum_\mu \gamma_\mu \sin(q_\mu a)}{m^2 + a^{-2}\sum_\mu \sin(q_\mu a)^2}. \tag{3.11}$$

Of particular interest is the case of massless quarks:

$$\tilde{\mathrm{D}}^{-1}_{\mathrm{naive}}(q)|_{m=0} \;=\; \frac{-ia^{-1}\sum_\mu \gamma_\mu \sin(q_\mu a)}{a^{-2}\sum_\mu \sin(q_\mu a)^2}. \tag{3.12}$$

It is worth noting that the lattice propagator has the correct continuum limit:

$$\tilde{\mathrm{D}}^{-1}_{\mathrm{naive}}(q)|_{m=0} \;\stackrel{a\to 0}{\longrightarrow}\; \frac{-i\sum_\mu \gamma_\mu q_\mu}{q^2}. \tag{3.13}$$

The continuum propagator has one pole at $q^2 = (0,0,0,0)$. However, for finite $a$ we observe 15 further ones within the Brillouin zone:

$$q \;=\; \left(\frac{\pi}{a},0,0,0\right), \left(0,\frac{\pi}{a},0,0\right), \ldots, \left(\frac{\pi}{a},\frac{\pi}{a},\frac{\pi}{a},\frac{\pi}{a}\right).$$

Since we know that poles of the propagator correspond to real particles, we realize that we have obtained 15 additional fermions, so-called *doublers*, by our discretization procedure. Obviously these are unphysical and we want to get rid of them.

A possible way for removing these lattice artefacts is to add an additional term to the Dirac operator, which decouples the doublers from the theory. Wilson [28] proposed the following one:

$$-a^4 \sum_{\mu=1}^{4} \mathbb{1}\frac{\delta_{x+a\hat{\mu},y} - 2\delta_{x,y} + \delta_{x-a\hat{\mu},y}}{2a}. \tag{3.14}$$

Note its similarity to a discretized version of a second derivative. This breaks the degeneracy between the physical and artificial modes.

So the new operator for the *Wilson fermions* is given by

$$\begin{aligned} \mathrm{D}_W(x,y) \;&=\; \sum_{\mu=1}^{4} \gamma_\mu \frac{\delta_{x+a\hat{\mu},y} - \delta_{x-a\hat{\mu},y}}{2a} + m\mathbb{1}\delta_{x,y} \\ &-\; \sum_{\mu=1}^{4} \mathbb{1}\frac{\delta_{x+a\hat{\mu},y} - 2\delta_{x,y} + \delta_{x-a\hat{\mu},y}}{2a}. \end{aligned} \tag{3.15}$$

When we again perform a Fourier transformation, we obtain

$$\tilde{\mathrm{D}}_W(q) \;=\; \frac{i}{a}\sum_{\mu=1}^{4} \gamma_\mu \sin(aq_\mu) + \frac{1}{a}\sum_{\mu=1}^{4} \mathbb{1}(1 - \cos(aq_\mu)) + m\mathbb{1}. \tag{3.16}$$

First we note that the additional term is an irrelevant operator that vanishes in the limit $a \to 0$ and hence the full action still has the appropriate continuum limit.
To comprehend the effect of the new term, we may consider the mass spectrum of our states.
If we expand $\tilde{\mathrm{D}}_W(q)$ for small $q$ we obtain $\tilde{D}_W = m\mathbb{1} + i\gamma_\mu q_\mu + O(a)$, as it is correct for our physical states. However, in the case where $q_\mu \to \frac{\pi}{a}$ for $l$ components $\mu$, we get

$$\tilde{\mathrm{D}}_W(q) \quad = \quad \frac{2l}{a} + O(1). \tag{3.17}$$

So the leading term for the mass of the doublers is of order $O(\frac{1}{a})$. Common lattices have an inverse lattice spacing $a^{-1} \gg 1$ GeV, so the unphysical states acquire a huge mass compared to light quark flavors, which are usually used to construct the action. Since the action increases linearly with the mass, these very heavy doublers will have a vanishing contribution to the path integral (see Sec. 2.3), which is the central quantity for any lattice calculation.
However, removing the doublers has an insidious downside. Since the Wilson term acts like a mass term in the Lagrangian, chiral symmetry is broken explicitly even for zero quark masses.
According to the Nielsen-Ninomiya theorem [29] it is not possible in an ultralocal, hermitian formulation to remove the doublers and to conserve the continuum chiral symmetry simultaneously.
One way out is to give up ultra-locality and to use a different, lattice specific chiral transformation, which leads to the Ginsparg-Wilson [30] equation for the Dirac operator. The *Overlap operator*, for example, satisfies this equation exactly [31, 32].
Wilson fermions explicitly break chiral symmetry even for vanishing quark mass due to the Wilson term. This has serious consequences, both technically and conceptionally, for simulations with Wilson fermions: fluctuations of the low-lying eigenvalues of the Dirac operator lead to a huge increase of the numerical efforts of simulations. This does not only occur when propagators are calculated but also during the generation of configurations with a Hybrid Monte-Carlo algorithm, leading to so-called *exceptional configurations* on a finite volume, which limit the quark masses one can reach.
Furthermore, due to the explicit breaking of the chiral symmetry the quark

mass is not protected from additive mass renormalization [33]. Therefore, one usually does not consider the bare quark mass but instead defines

$$m = m_0 - m_{\text{crit}}, \tag{3.18}$$

with the critical quark mass $m_{\text{crit}}$. It is defined as the quark mass where the mass of the pseudoscalar meson vanishes and its value has to be determined for each simulation separately.

### 3.1.3 Gauge Invariance on the Lattice

We have seen that we have to include additional terms in our action to remove lattice artefacts. However, an even more fundamental goal is to preserve gauge invariance. The action (3.15) is obviously not invariant under (2.2) and (2.3).

Again we need gauge bosons, but this time we cannot use just $A_\mu(x)$. The discrete derivative is a non-local object and therefore we need so-called *gauge transporters* to maintain gauge symmetry. These are nothing more than the link variables (3.2).

Now we can investigate the behavior of a gauge link sandwiched between two fermion fields, that are located at adjacent sites. This non-local object transforms like

$$\bar{\psi}(x)\, U_\mu(x)\, \psi(x+\hat{\mu}) \;\longrightarrow\; \bar{\psi}(x)\Lambda^{-1}(x)\, \Lambda(x) U_\mu(x) \Lambda^{-1}(x+a\hat{\mu})\, \Lambda(x+a\hat{\mu})\psi(x+\hat{\mu}) \tag{3.19}$$

The link provides the appropriate transformation matrices to its left and right in order to make the whole object gauge invariant.

Similarly, we put the link variables between all non-local objects in the Wilson Dirac operator. We thereby obtain

$$\begin{aligned} \mathrm{D}_W(x,y) &= \sum_{\mu=1}^{4} \gamma_\mu \frac{U_\mu(x)\delta_{x+a\hat{\mu},y} - U_{-\mu}(x)\delta_{x-a\hat{\mu},y}}{2a} + m\mathbb{1}\delta_{x,y} \\ &- \sum_{\mu=1}^{4} \mathbb{1}\, \frac{U_\mu(x)\delta_{x+a\hat{\mu},y} - 2\delta_{x,y} + U_{-\mu}(x)\delta_{x-a\hat{\mu},y}}{2a}, \end{aligned} \tag{3.20}$$

where $U_{-\mu}(x) = U_\mu^+(x - a\hat{\mu})$.

### 3.1.4 The Gauge Action

As in the continuum case, we also want to include kinetic terms for the gauge bosons. We saw that it is suitable to use link variables on the lattice.

Therefore, we search for a gauge invariant combination of them. The transformation behavior (3.3) suggests the use of closed loops of links. The easiest possibility is a square with one link at each side. This object is named a *plaquette* $P_{\mu\nu}$:

$$P_{\mu\nu}(x) = U_\mu(x)U_\nu(x+a\hat{\mu})U_{-\mu}(x+a\hat{\mu}+a\hat{\nu})U_{-\nu}(x+a\hat{\nu}), \quad (3.21)$$

with the convention

$$U_{-\mu}(x) = U_\mu(x-a\hat{\mu})^\dagger. \quad (3.22)$$

For non-Abelian gauge theories like QCD, taking the trace of the plaquette is necessary to obtain an invariant quantity.
A gauge action built from plaquettes was first proposed by Wilson [34]:

$$S_{\text{gauge}} = \beta a^4 \sum_x \sum_{1\le\mu<\nu\le 4} \left\{ 1 - \frac{1}{3}\text{Re}[\text{Tr}(P_{\mu\nu}(x))] \right\}, \quad (3.23)$$

where

$$\beta = \frac{6}{g^2}. \quad (3.24)$$

But ultimately a specific action must have the correct continuum limit. For small $a$, (3.23) reduces to

$$S_{\text{gauge}} = -\frac{\beta}{12}\int d^4x \text{Tr}[F_{\mu\nu}(x)\, F_{\mu\nu}(x)] + O(a^2). \quad (3.25)$$

Using the Wilson gauge action we have to cope with discretization errors of orders $O(a^2)$.
Of course one may also consider more complicated loops. This was actually done for the Lüscher and Weisz gauge action [35, 36], which reduces the discretization errors to $O(a^4)$, if the coefficients of the extra terms are determined non-perturbatively.

### 3.1.5 The Action of Choice: Clover Wilson

In principle the number of possible ways to regularize the theory is unlimited. Thus one has a range of choices of how to discretize the QCD action, as long as the correct continuum limit is maintained.
Today a bunch of different lattice actions exist, each with its up- and downsides. State of the art are actions which fully preserve the chiral symmetry, like *Domain Wall* [37, 38][3] or the above mentioned *Overlap* formalism. How-

[3] At least in the limit $L_5 \to \infty$.

ever, as these implementations are rather expensive in terms of computer time, simulations are limited to small lattice volumes and/or low statistics. Another possibility was suggested by Kogut and Susskind [39, 40, 41] and is quite popular for groups in the United States nowadays (see [42, 43], for instance). The idea is to spin diagonalize the Dirac operator leading to a distribution of the individual spinor components among different lattice sites within a hypercube. Very low computer time costs of this so-called *Staggered Fermion* formalism allow for very high statistics runs with reasonable lattice sizes and spacings. Unfortunately, until now there is no proof of the validity of the the *fourth root trick* (see [44], for example) which is necessary for dynamical staggered simulations. Actually, there is a lot of evidence of the contrary [45], which lead to an intensive discussion recently [46].
Approximately chiral formulations like the the *Chirally Improved Action* [47] or renormalization group inspired ones like the *Fixed Point Action* [48] are also in use, though with inferior popularity.
A clever idea, especially when simulating heavy quarks, is to generate configurations with different spacings for time and space. The drawback of using these so-called anisotropic lattices is the necessity of intricate tuning to fix the parameters, especially in the dynamical case.
The action of choice naturally should always comply with the intent of the project. Since we are concentrating on charm quarks, which can be regarded as rather heavy, simulating with a fully chiral action would be overkill, as chiral symmetry and its spontaneous breaking play a minor role in this regime and as we aspire to reasonable statistics.
On the other side of the spectrum lies the possibility of implementing an effective theory for heavy quarks like NRQCD, which works perfectly fine for bottomonia [49, 50], for example. However, it is easy to see that charmonium is not suited for such a non-relativistic treatment. The average squared relative velocity of the quarks can be estimated to be $\langle v^2 \rangle \approx 0.4$, which leads to huge radiative and relativistic corrections. For comparison, this number is $\langle v^2 \rangle \approx 0.1$ for bottomonium.
As all these approaches do not fit our requirements, an old-fashioned candidate seems opportune. The Wilson action offers cheap and reliable simulations and thus turns out to be very suitable for charmonium, especially on very fine lattices. Furthermore, the freedom of discretization can be utilized to reduce lattice artefacts.

In 1985, Sheikholeslami and Wohlert [51] generalized the Symanzik improvement program [52] to lattice fermion fields. Similar to Lüscher and Weisz, they added higher dimensional operators to the naive lattice fermion action, which vanish in the continuum limit. Through symmetry considerations and by using the equations of motion this set of operators is reduced to only one, the Clover term.
The resulting *Clover-Wilson* action then reads

$$S_{ferm}^{SW} = S_{ferm}^{W} + c_{SW}\frac{i}{4}a^5\sum_x \bar{\psi}(x)\sigma_{\mu\nu}F_{\mu\nu}\psi(x). \tag{3.26}$$

For $F_{\mu\nu}$ one usually chooses the simplest lattice realization which is given by

$$F_{\mu\nu}(x) = \frac{1}{8a^2}\left[Q_{\mu\nu}(x) - Q_{\nu\mu}(x)\right], \tag{3.27}$$

with

$$\begin{aligned} Q_{\mu\nu}(x) = {} & U_\mu(x)U_\nu(x+a\hat{\mu})U_{-\mu}(x+a\hat{\mu}+a\hat{\nu})U_{-\nu}(x+a\hat{\nu}) \\ & + U_\mu(x)U_{-\nu}(x+a\hat{\mu})U_{-\mu}(x+a\hat{\mu}-a\hat{\nu})U_\nu(x-a\hat{\nu}) \\ & + U_{-\mu}(x)U_{-\nu}(x-a\hat{\mu})U_\mu(x-a\hat{\mu}-a\hat{\nu})U_\nu(x-a\hat{\nu}) \\ & + U_{-\mu}(x)U_\nu(x-a\hat{\mu})U_\mu(x-a\hat{\mu}+a\hat{\nu})U_{-\nu}(x+a\hat{\nu}). \end{aligned} \tag{3.28}$$

The field strength tensor can be depicted as in Fig. 3.2, which roughly resembles four-leaved clovers. After this improvement, discretization errors are reduced to $O(a^2)$, if $c_{SW}$ is determined non-perturbatively [53].
It is worth to mention that the Fermilab collaboration reinterpreted the Clover action [54]. The Fermilab action creates a smooth connection between the light and heavy fermion regimes by identifying and correctly renormalizing nonrelativistic operators present in the Clover action. Discretization errors are then $O(a\Lambda_{QCD})$ and not $O(am_Q)$ like in NRQCD. In the light quark limit the Clover action is recovered.

## 3.2 The Path Integral on the Lattice

As mentioned above, in the Feynman path integral formalism we have to integrate over all degrees of freedom, namely quark, antiquark and gluon fields. On the lattice the integration over the gluon fields is replaced by one

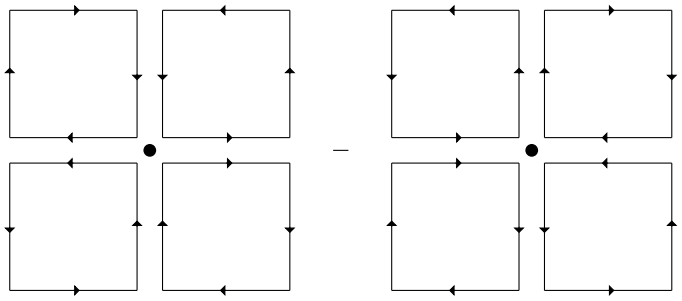

Figure 3.2: Picture of the simplest formulation of the field strength tensor on the lattice. The clover-like shapes are responsible for the name of the clover improved Wilson action.

over the link variables. So the expectation value of an observable evaluated with the help of the path integral is given by

$$\langle \mathcal{O}[\psi,\bar{\psi},U]\rangle \;=\; \frac{1}{Z}\int [d\psi]\,[d\bar{\psi}]\,[dU]\,\mathcal{O}[\psi,\bar{\psi},U]\;e^{-S_{\mathrm{QCD}}}\;, \qquad (3.29)$$

where

$$[dU] \;=\; \prod_x \prod_\mu dU_\mu(x). \qquad (3.30)$$

$dU_\mu(x)$ is the measure invariant under group transformations, the so-called *Haar measure*. All three measures are well defined on the lattice.
Note the obvious similarity to statistical mechanics, where $Z$ corresponds to the partition function and the weighting factor is given by $e^{-E/k_bT}$. This makes it possible to apply all the techniques developed for calculating thermodynamical quantities to quantum field theory. The Monte Carlo method described in the next section is probably the most important one for numerical calculations.
However, one part of the path integral can be solved analytically. After an integration over the fermion fields we are left with an effective action for the gluons. To do so, we separate the fermionic and the gauge field part:

$$\langle \mathcal{O}[\psi,\bar{\psi},U]\rangle = \frac{\int [dU]\,e^{-S_{\mathrm{gauge}}[U]}\,(\int\,[d\psi]\,[d\bar{\psi}]\,e^{-S_{\mathrm{ferm}}[\psi,\bar{\psi},U]}\,\mathcal{O}[\psi,\bar{\psi},U])}{\int [dU]\,e^{-S_{\mathrm{gauge}}[U]}(\int [d\psi]\,[d\bar{\psi}]\;e^{-S_{\mathrm{ferm}}[\psi,\bar{\psi},U]})}. \qquad (3.31)$$

It is a welcome feature that the fermion action depends on both the fermionic and gauge degrees of freedom, whereas the gauge action only depends on the

latter ones. Therefore, we can perform the so-called *fermion contraction*; i. e., we integrate out the fermionic part. Consider the integral

$$I_f = \int [d\psi]\,[d\bar{\psi}]\, e^{-S_{\text{ferm}}[\psi,\bar{\psi},U]}\mathcal{O}[\psi,\bar{\psi},U]. \tag{3.32}$$

Since the action is a bilinear functional in the fermion fields, this integral is similar to a Gaussian one, albeit in Grassmann variables, and can be solved analytically:

$$I_f = \det \mathrm{D}[U]\ \mathcal{O}[D^{-1},U]. \tag{3.33}$$

$\mathcal{O}[D^{-1},U]$ is now a functional of the quark propagator and link variables, but it no longer depends on the fermionic fields.
The determinant is referred to as the *fermion determinant*. The calculation of this determinant is extremely expensive, since $D[U]$ is usually a huge matrix. If we, for example, consider an isotropic lattice with 20 sites in each direction, the dimension of $D[U]$ is $20^4 \cdot 3 \cdot 4 \sim O(10^6)$.
In order to save computer time, the determinant is often set equal to one. This is called the *quenched approximation*. The fermion determinant describes closed fermion loops. Working in the quenched approximation therefore omits contributions of sea quarks. Nevertheless, this approximation gives surprisingly good results for many applications.
If enough computer power is available, then so-called *dynamical* simulations are possible. The determinant can for instance be calculated by rewriting it as bosonic Gaussian integrals over *pseudofermion* fields $\Psi$ [55]:

$$\det \mathrm{D}[U] = \int [d\Psi^* d\Psi]\, e^{[-\Psi^* D^{-1}\Psi]}. \tag{3.34}$$

## 3.3 Ensemble Creation

By integrating out the fermionic degrees of freedom we have reduced (3.29) to an average with respect to the gauge configurations:

$$\langle \mathcal{O}[\psi,\bar{\psi},U]\rangle = \frac{\int [dU]\, e^{-S_{\text{gauge}}[U]}\ \det \mathrm{D}[U]\, \mathcal{O}[D^{-1},U]}{\int [dU]\, e^{-S_{\text{gauge}}[U]}\ \det \mathrm{D}[U]} \tag{3.35}$$

$$= \langle \mathcal{O}[U]\rangle_U. \tag{3.36}$$

A complete numerical integration is hopeless, since the number of degrees of freedom exceeds all capacities.

A much more efficient way is the use of *importance sampling Monte Carlo methods*. The idea is to pick the configurations which give the largest contribution to the path integral. This is done by creating the configurations with a probability distribution $P[U]$:

$$P[U_i] = \frac{e^{-S_{\text{gauge}}[U_i]} \det \mathrm{D}[U_i]}{\sum_{j=1}^{N} e^{-S_{\text{gauge}}[U_j]} \det \mathrm{D}[U_j]}. \tag{3.37}$$

The simplest and oldest technique for this purpose is the *Metropolis* algorithm [56]. Nowadays the *Hybrid Monte Carlo* method, which combines both the *Molecular Dynamics* and Metropolis algorithm, is very popular [57].
The sample average of the observable on this subset of possible configurations is

$$\bar{\mathcal{O}}_N = \tfrac{1}{N} \textstyle\sum_{i=1}^{N} \mathcal{O}[\{U\}_i]. \tag{3.38}$$

The weighting factor $e^{-S_{\text{gauge}}} \det \mathrm{D}[U]$ has disappeared, because it is already included into the generation of the configuration.
The law of large numbers then guarantees that the sample average becomes the expectation value $\langle \mathcal{O} \rangle_U$ in the limit of infinitely many configurations

$$\langle \mathcal{O} \rangle_U = \lim_{N \to \infty} \bar{\mathcal{O}}_N. \tag{3.39}$$

For a finite number of configurations all results are affected by a statistical error, which has to be treated by a careful error analysis, see App. C. Furthermore, since all configurations originate from the same updating process (*Markov chain*), they are correlated. *Autocorrelation times* quantify this. Obviously, for reliable results one should strive for low autocorrelation times and large statistics $N$.

*You can know the name of a bird in all the languages of the world, but when you're finished, you'll know absolutely nothing whatever about the bird... I learned very early the difference between knowing the name of something and knowing something.* – *The Physics Teacher Vol. 7*

Richard Feynman

# 4 Analysis

As discussed in the previous chapter, configurations can be generated independently of the observable one intends to measure. Equipped with an ensemble, one can start doing measurements on innumerably many different quantities.
In this work we focus on two types of observables: spectroscopic ones, i.e. masses, and matrix elements. Both can in principle be extracted from single two point functions, however, this often turns out to be a delicate and sometimes even impossible task, especially for excited states. Much more effective is the use of a variational method, addressed later on.
We start the discussion by explaining the calculation of a usual correlator.

## 4.1 Standard Spectroscopy

*Euclidean correlators* are defined as the vacuum expectation values of the product of two operators separated in time:

$$C(\hat{O}_1, \hat{O}_2, t) \quad = \quad \langle \hat{O}_2(t) \hat{O}_1(0) \rangle. \tag{4.1}$$

For example, let $\hat{O}_1$ be a meson creation operator at time zero and $\hat{O}_2$ the corresponding annihilation operator at time $t$. The so-constructed correlator would simply represent the meson propagating from time 0 to $t$.
It is also possible to show that

$$C(\hat{O}_1, \hat{O}_2, t) \quad = \quad \lim_{T \to \infty} \frac{1}{Z(T)} \mathrm{Tr} \left[ e^{-(T-t)\hat{H}} \hat{O}_2 e^{-t\hat{H}} \hat{O}_1 \right], \tag{4.2}$$

with

$$Z(T) \quad = \quad \mathrm{Tr} \left[ e^{-T\hat{H}} \right] , \tag{4.3}$$

and $\hat{H}$ being the full QCD Hamiltonian and $T = N_t a$ is the maximal time extent.

By manipulating (4.2) we get:

$$\begin{aligned} \frac{1}{Z(T)}\mathrm{Tr}\left[e^{-(T-t)\hat{H}}\hat{O}_2 e^{-t\hat{H}}\hat{O}_1\right] &= \frac{\sum_{n,m} e^{-(T-t)E_m}\langle m|\hat{O}_2|n\rangle e^{-tE_n}\langle n|\hat{O}_1|m\rangle}{\sum_m e^{-TE_m}} \\ &= \frac{\sum_{n,m}\langle m|\hat{O}_2|n\rangle\langle n|\hat{O}_1|m\rangle e^{-t\Delta E_n} e^{-(T-t)\Delta E_m}}{1 + e^{-T\Delta E_1} + e^{-T\Delta E_2} + \dots}. \end{aligned}$$

The trace is evaluated in the basis of eigenstates $|m\rangle$ of the Hamiltonian. Another complete set of mass eigenstates $|n\rangle$ was inserted between the operators. In the second step, the energy difference between the state $|n\rangle$ and the vacuum $|0\rangle$ is written as $\Delta E_n = E_n - E_0$. Since we can only measure energy differences, we shift the vacuum energy to zero $E_0 = 0$ and identify $\Delta E_n$ as $E_n$.

Taking the limit $T \to \infty$ only the vacuum state $|m\rangle = |0\rangle$ survives:

$$\lim_{T\to\infty} \frac{1}{Z(T)}\mathrm{Tr}\left[e^{-(T-t)\hat{H}}\hat{O}_2 e^{-t\hat{H}}\hat{O}_1\right] = \sum_n \langle 0|\hat{O}_2|n\rangle\langle n|\hat{O}_1|0\rangle\, e^{-tE_n}\,. \qquad (4.4)$$

So we are left with a sum over energy eigenstates, where the summands are products of amplitudes and exponential factors. The amplitudes determine the overlap of the respective operator with the respective physical state $n\rangle$. Non-vanishing amplitudes only arise from states with the same quantum numbers as the operators $\hat{O}_1$ and $\hat{O}_2$, respectively. The exponent is the energy of the state times the separation of the operators in Euclidean time. If one is only interested in the ground state, one may exploit the fact that with some optimized operators for large enough times the excited states become suppressed and one only observes a single exponential belonging to the lowest state.

From Sec. 3.2 we know that expectation values can also be evaluated with the help of the path integral:

$$\langle \hat{O}_2(t)\hat{O}_1(0)\rangle = \frac{1}{Z}\int [d\psi]\,[d\bar{\psi}]\,[dU]\, O_2[\psi,\bar{\psi},U;t]\, O_1[\psi,\bar{\psi},U;0]\; e^{-S_{QCD}}\,. \qquad (4.5)$$

By evaluating (4.5) numerically and comparing with the right hand side of (4.4), one can extract amplitudes and masses, e. g., by multi-exponential fits. An important quantity for spectroscopy is the *effective mass* of a correlator, defined by

$$m_{\mathrm{eff}}\left(t + \frac{a}{2}\right) = \ln\frac{C(t)}{C(t+a)}\,. \qquad (4.6)$$

With the help of effective mass plots one can determine appropriate fitting ranges for ground state masses. When the curve has reached a plateau, contributions of higher excited states have become sufficiently suppressed.
It is important to remember that the above mentioned interpolating fields are defined on the lattice, which breaks the continuous rotational symmetry $O(3)$ down to the cubic group $O_h$ (see [58], for instance). Thus the states coupling to these interpolators can be classified according to one of the five irreducible representations of $O_h$, which in the continuum limit generally do not correspond to a single $J^{PC}$. For mesons this non-unique mapping can for example be found in [59]:

$$\begin{aligned} A_1 &\rightarrow J = 0, 4, \ldots \\ A_2 &\rightarrow J = 3, \ldots \\ T_1 &\rightarrow J = 1, 3, 4, \ldots \\ T_2 &\rightarrow J = 2, 3, 4, \ldots \\ E &\rightarrow J = 2, 4, \ldots \end{aligned} \tag{4.7}$$

The identification of states in a correlator can be a delicate task, in particular for charmonia. The lowest mass does not always corresponds to the lowest $J$ number. For instance, in Chap. 5 we will encounter an operator in the $T_2$ representation, which projects out both, $2^{+-}$ and $3^{+-}$. The $2^{+-}$ is an exotic quantum number and thus the respective state is much heavier than the $3^{+-}$ state, which will dominate the correlator.

## 4.2 The Variational Method

As can be seen from (4.4) every correlation function contains a tower of states. For ground state spectroscopy the unwanted contributions from higher lying states may represent a serious problem. If they do not die out at sufficient small times than the signal to noise ratio will be reduced to an unbearable value. Thus, it is desirable to see the ground state dominating right from the beginning or at least to reduce the contaminations from higher states.
Furthermore, extracting excited states from a single correlators is very challenging, due to their short Euclidean lifetime.
To gain information both on the ground and excited states, a variety of approaches have been tried. They reach from brute force multi-exponential fits

to more sophisticated techniques like *Bayesian priors* [60] or *maximum entropy* [61] methods. The Bayesian priors method makes use of conditionally biased fits, i.e. one starts with simple one-exponential fits at large Euclidean time values and then continues with two-exponential fits including the result of the earlier fit as a bias. The maximum entropy method is based on the representation of the correlation function as the Laplace transform of a spectral density, which is fitted to the lattice data. Experience from statistical physics shows that large statistics are necessary for reliable results and significant ambiguities arise when one tries to extract more energy levels from moderately precise correlation data.

Probably the most powerful method to disentangle the states is to apply a variational method to the system. This approach was first proposed by Michael [62] and later refined by Lüscher and Wolff [63].

The variational method has successfully been applied, amongst others, in [64, 65, 66, 67]. The idea is to choose a set of different interpolating fields for a specific channel and build a cross correlation matrix from these, whose eigenvalues and eigenvectors then provide the information needed.

We choose a basis of operators[1] $O_i$, $i = 1, \ldots, N$, destroying a color singlet state within a given lattice $O_h \otimes C$ representation. The operators may differ for example by their spatial extent or their Fock structure and usually are not mutually orthogonal.

These are then used to construct a cross correlation matrix,

$$C_{ij}(t) = \langle O_i(t) O_j^\dagger(0) \rangle \ , \tag{4.8}$$

which can be spectrally decomposed,

$$C_{ij}(t) = \sum_n v_i^n v_j^{n*} e^{-E_n t}. \tag{4.9}$$

The $v_i^n = \langle 0|\hat{O}_1|n\rangle$ are the matrix elements coupling the $i$th operator with the $n$th state (see (4.4)). $E_n$ is the corresponding energy eigenvalue.

Since $C_{ij}$ is a real[2] Hermitian matrix[3], the $v^n$ are mutually orthogonal.

We want to emphasize that $C$ is actually defined on the infinite dimensional

[1] For convenience the term "operator" is often used synonymously for the state created from the vacuum by the respective operator.

[2] In general $C_{ij}$ is complex, however for the operators we use, it only has real entries.

[3] This only holds in the limit of infinite statistics. We symmetrize $C(t)$ by hand, after checking that violations are consistent with zero, within the statistical errors.

Hilbert space, whereas $C_{ij}$ is projected onto the subspace spanned by the finite dimensional, not necessarily orthogonal basis of operators. Thus a large portion of the Hilbert space is left out, which leads to corrections to the eigenvalues and -vectors (see (4.12) and (4.13)). However, by choosing a suitable basis of interpolators, one hopes to grip the essential parts of the wavefunction of the physical state, thereby minimizing these corrections. How to find such a suitable basis will be shown in Sec. 4.7.
In order to obtain the eigenvalues and -vectors we solve the symmetric generalized eigenvalue problem

$$C^{-1/2}(t_0)\, C(t)\, C^{-1/2}(t_0)\, \psi^\alpha(t,t_0) = \lambda^\alpha(t,t_0)\, \psi^\alpha(t,t_0)\,, \tag{4.10}$$

where $t_0$ is the normalization timeslice. If we choose $t_0$ too large, the rank of $C(t_0)$ will not be maximal anymore as excited states will die out in Euclidean time. For $t_0$ chosen too small, $C(t)$ will receive contributions from more than the $N$ lowest lying states, resulting in unstable eigenvectors and effective masses.
The original eigenvalue problem was proposed without symmetrization:

$$C(t)\widetilde{\psi}^\alpha(t,t_0) = \widetilde{\lambda}^\alpha(t,t_0) C(t_0) \widetilde{\psi}^\alpha(t,t_0)\,, \tag{4.11}$$

Although this version yields the identical eigenvalues, the eigenvectors are only orthogonal on the metric $C(t_0)$ and hence do not fulfill the same orthogonality condition as the physical states.
Please note that we switched the index notation from $n$ to $\alpha$, just to take account of the difference between the physical eigenstates and the eigenstates coming from the projected $C$.
It can be shown that the eigenvalues behave like

$$\lambda^\alpha(t,t_0) \propto e^{-(t-t_0)\, E_\alpha}[1 + \mathcal{O}(e^{-(t-t_0)\, \Delta E_\alpha})]\,, \tag{4.12}$$

where $\Delta E_\alpha$ is the energy difference of $E_\alpha$ and the first state not contained in the operator basis[4].
The correction factor arises from the finite dimensionality and non-orthogonality of the operator basis. Fortunately, these are exponentially suppressed in Euclidean time. With a sophisticated choice of the basis their magnitude can be decreased from the beginning.

[4] At least to first order in perturbation theory. To second order also states within the basis can contribute.

The eigenvectors also approach their physical counterparts asymptotically [68]:

$$\psi^{\alpha}(t,t_0) = v^{\alpha} + \mathcal{O}(e^{-(t-t_0)\,\Delta E_{\alpha}})\,. \tag{4.13}$$

We take notice that for large enough times we can extract the physical masses and couplings[5], elevating the variational method to the central tool in our analysis.

## 4.3 Quark Propagators

We have not yet explained how to explicitly calculate a correlation function on the lattice. For example, consider a meson, interpolated by a local operator of the form $O = \bar{q}\,\Gamma q$, where $\Gamma$ is an element of the Clifford algebra, propagating from spacetime point $y$ to $x$[6]:

$$\begin{aligned}
\langle O(x)\bar{O}(y)\rangle &= \langle \bar{q}(x)\,\Gamma\, q(x)\, q(y)\,\Gamma\,\overline{q}(y)\rangle \\
&= \langle \overbrace{\overline{q}(x)\,\Gamma\, \overbrace{q(x)\, q(y)}\,\Gamma\,\overline{q}(y)}\rangle - \langle \overbrace{\overline{q}(x)\,\Gamma\, q(x)}\, \overbrace{q(y)\,\Gamma\,\overline{q}(y)}\rangle \\
&= \langle M^{-1}(x,y)\,\Gamma\, M^{-1}(y,x)\,\Gamma\rangle - \langle M^{-1}(x,x)\,\Gamma\, M^{-1}(y,y)\,\Gamma\rangle\ ,
\end{aligned} \tag{4.14}$$

where in the second step we contracted the fields according to *Wick's theorem*. $M^{-1}(x,y)$ denotes a quark propagator from $x$ to $y$[7].

We are left with two contributions, a connected and a disconnected one (see Fig. 4.1). The interpretation of the connected part is that the quark-antiquark pair, with quantum numbers defined by the Gamma matrix, is created at $y$ and propagates to $x$, where it is annihilated. The disconnected part can be seen as the $q\bar{q}$ pair being created at $y$, annihilated at some intermediate point, just to be created again from the vacuum at some other intermediate point and eventually being annihilated at $x$. The term "disconnected" should not be understood in the sense of perturbation theory. Actually, the two quark loops are connected by arbitrarily many gluons, whose effect is implicitly contained in the gauge configuration.

Also remember in this context that according to the path integral formalism

[5] Actually, only renormalized couplings make true physical sense. But this is beyond the scope of this work.

[6] In Minkowski space.

[7] In the following, the full Dirac operator will be indicated by $M$ and the massless Dirac operator by $D$.

the correlation function takes all possible paths into account: for instance, all higher order couplings to gluons or virtual quark loops on dynamical configurations. Furthermore, the quarks, since they are simulated fully relativistically, are allowed to propagate backwards in time which can lead to contributions interpreted as intermediate multiple quark states [69]. Thus, Fig. 4.1 shows only one of infinitely many possibilities.
As can be seen in (4.14) we have reduced the calculation of a correlation function to the determination and combination of quark propagators. The quark propagator is the inverse of the Dirac matrix $M$. Consequently, we just have to invert $M$ with established numerical tools on a computer and we are done. This, however, is just wishful thinking with today's capacities. Even holding a matrix with a dimension comparable to the one of the Dirac matrix[8] in the memory is impossible[9].
Ways out are either to be content with only part of the propagator or to estimate the full propagator with stochastic methods. Both are addressed in the following sections.

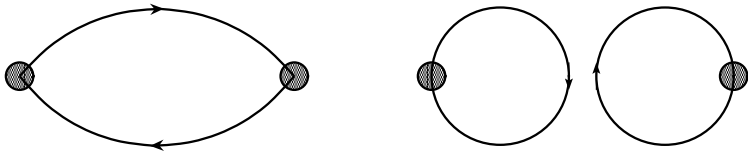

Figure 4.1: Sketch of a connected (left) and a disconnected (right) part of a meson two point function. The horizontal axis corresponds to Euclidean time.

## 4.4 One-to-All Propagators

Instead of inverting the full Dirac matrix, solving for one source vector $\eta$ is a common technique to circumvent the computational restrictions:

$$\chi = M^{-1}\eta \ . \tag{4.15}$$

This is equivalent solving the linear system:

$$M\chi = \eta, \tag{4.16}$$

[8] For a typical lattice size of $24^3 \times 48$ the dimension of $M$ is of order $O(10^6)$.

[9] For most lattice actions $M$ is a sparse matrix; thus it is in principle possible to hold it in memory. However, $M^{-1}$ is not sparse any more.

by iterative methods like *conjugate gradient (CG)* [70] or some of its improved versions like *stabilized biconjugate gradient (BiCGStab)* [71], which also works for nonhermitian matrices. CG gives an exact solution for $\chi$ after at most $N$ iterations, where $N$ is the dimension of $M$. However, as there is a statistical error inherent in our simulation anyway, a certain relative accuracy $\epsilon$ (also called *residuum*) is sufficient:

$$\frac{||M\eta - \chi||}{||\chi||} < \epsilon. \tag{4.17}$$

The speed of convergence is governed by the condition number of $\kappa(M)$

$$\kappa(M) = \left|\frac{\lambda_{max}}{\lambda_{min}}\right|, \tag{4.18}$$

where $\lambda_{max}$ and $\lambda_{min}$ are the largest and smallest eigenvalues of the matrix $M$, respectively. For small quark masses the lowest eigenvalue of $M$ is nearly zero, leading to a very large condition number, in turn resulting in many more iterations in order to reach a given relative accuracy. This is one of the reasons why simulations at the physical pion mass have become possible only recently [72].

The form of the source vector is arbitrary. A natural choice is just to fill one spin-color component at one lattice site:

$$\eta_{\alpha a x} = \delta_{\alpha\alpha'}\,\delta_{aa'}\,\delta_{xx'} \tag{4.19}$$

The inversion on this vector projects out one row of the full propagator. Inverting on a set of 12 such vectors, each filled at a different spin-color component, but at the same site, yields a propagator reaching from one to all lattice points. Consequently it is called a one-to-all propagator (see Fig. 4.2).

Of course, one is free to construct the source vector according to one's needs. In order to control the overlap with physical states, the local source can for example be smeared to a Gaussian, which will be discussed in detail in section 4.7.

Another possibility is a so-called *wall source*. The source vector is filled at all sites of one timeslice with a "1" in each spin-color component, leading to an incoherent sum of contributions when constructing a correlator from these. This source is useful in association with hybrid interpolating fields, i.e. interpolators containing an explicit gluonic content represented by some

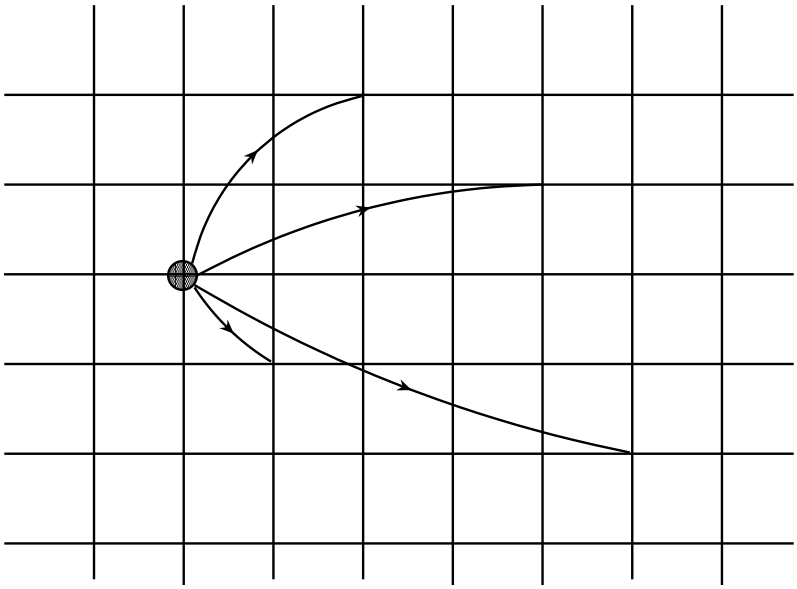

Figure 4.2: Two-dimensional sketch of a one-to-all propagator.

combination of links. Gauge configurations may exhibit so-called *dislocations* [73], which can lead to a poor signal for local hybrid operators. By utilizing a wall source their impact is averaged away.
In all cases, in order to boost statistics and to project to definite momentum, we sum the sink over a spatial hyper-plane including an appropriate phase factor:

$$O(t,\mathbf{p}) = \sum_{\mathbf{x}} O(t,\mathbf{x})\, e^{-i\mathbf{p}\mathbf{x}} \ . \tag{4.20}$$

In this work we only consider zero momentum states $\mathbf{p} = 0$.
The source does not need to be summed due to translational invariance of expectation values. This is how one often can get away with one-to-all propagators.

## 4.5 All-to-All Propagators

For some applications traditional one-to-all propagators are not sufficient. Consider, for example, the disconnected part of (4.14). Performing a momentum projection over the sink as for the connected part is not possible due to the lack of corresponding propagators. No reasonable results can be expected for a quantity that is very noisy anyway. A propagator going from

every point on the lattice to any other point, a so-called *all-to-all propagator (A2AP)* is necessary (see Fig. 4.3). For an introduction into A2AP and applications see [74, 75, 76, 77, 78], for instance.
With the present computer power the only possibility for realization is the estimation by stochastic methods. The procedure is as follows.
We can start out by creating a set of random-noise source vectors $\eta_j,\ j = 1, \ldots, N$:

$$\eta^j_{\alpha,a,x} \quad = \quad e^{2\pi i r} \quad , \tag{4.21}$$

where $\alpha = 1, \ldots, 4$ is the spinor index, $a = 1, 2, 3$ is the color index, $x$ is the spacetime coordinate and $j = 1, \ldots, N$ labels the $N$ different noise vectors. On the right hand side $r$ is a random number (uniformly) distributed within $[0, 1)$. For many classes of problems discrete values of $r$ are more suitable [79], e.g.,

$$\eta^j_{\alpha,a,x} \quad = \quad \frac{1}{\sqrt{2}}(v + iw) \quad , \tag{4.22}$$

with $v, w \in \{\pm 1\}$. This is called complex $\mathbb{Z}_2$ noise.
We define the *random contraction* of two vectors $\psi$ and $\phi$:

$$\frac{1}{N}\sum_i \psi^i_{\alpha,a,x}\phi^{i\,*}_{\beta,b,y}\,. \tag{4.23}$$

Since the random numbers in different components of a noise vector are uncorrelated (actually this is a demand on the random number generator in use), their random contraction gives:

$$\frac{1}{N}\sum_i \eta^i_{\alpha a x}\eta^{i\,*}_{\beta b y} = \delta_{xy}\delta_{ab}\delta_{\alpha\beta} + O\left(\frac{1}{\sqrt{N}}\right) \tag{4.24}$$

The size of the error follows from the *central limit theorem*.
By solving the Dirac operator $M$ on these sources we obtain $N$ solution vectors $s^i (i = 1, \ldots, N)$:

$$s^i = M^{-1}\eta^i, \quad i = 1, \ldots, N. \tag{4.25}$$

With these definitions it is easy to write down a naive estimate for an A2AP. We just have to perform the random contraction with the source and solution vectors:

$$\sum_i s^i \eta^{i\,\dagger} = \sum_i M^{-1}\eta^i\eta^{i\,\dagger} = M^{-1} + O\left(\frac{1}{\sqrt{N}}\right)\ . \tag{4.26}$$

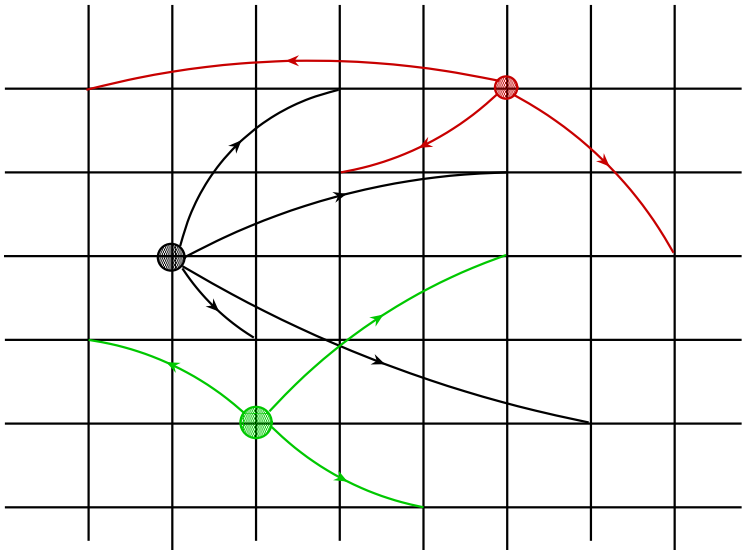

Figure 4.3: Two-dimensional sketch of an all-to-all propagator. The three source points are plotted in behalf of all the other points.

## 4.6 Noise Reduction Techniques

The good news is that we have an expression for an A2AP now, albeit with an inherent stochastic noise. The bad news is that the magnitude of this error in many applications will severely disturb the signal and thereby making results meaningless.

One origin of large uncertainties of the naive estimate is that we placed the noise source vectors all over the lattice. This is cheap, but not very efficient. The site, where the propagator ends, is surrounded by parts of the source vector, which do not contribute to the signal, but only to noise. To see this more clearly, consider the estimation of a propagator from the spacetime coordinate $x$ to $y$ (spinor and color indices suppressed):

$$\begin{aligned} s_y^i \eta_x^{i\,\dagger} &= \sum_z M_{yz}^{-1} \eta_z^i \eta_x^{i\,\dagger} \\ &= \sum_z M_{yz}^{-1} \left[ \delta_{zx} + (1-\delta_{zx}) O\left(\frac{1}{\sqrt{N}}\right) \right] \\ &= M_{yx}^{-1} + \sum_{z \neq x} M_{yz}^{-1} O\left(\frac{1}{\sqrt{N}}\right) \end{aligned} \tag{4.27}$$

We obtain the desired exact propagator plus some noise part which goes like $\frac{1}{\sqrt{N}}$. The latter one originates from all source locations $z \neq x$ (see Fig. 4.4).

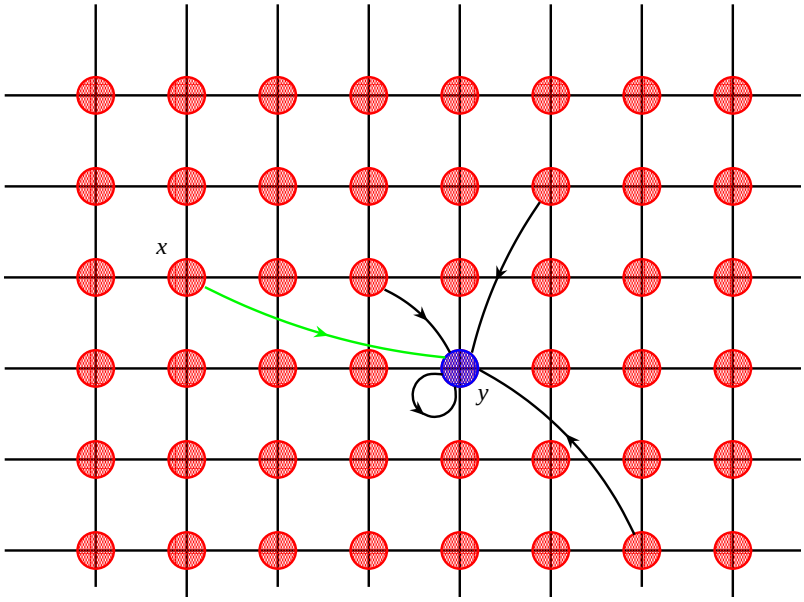


Figure 4.4: Two-dimensional sketch of a global noise source. For the propagator from $x$ to $y$ only the green curve contributes to the signal, the black ones are pure noise.

Since signals on the lattice decrease exponentially with the distance,

$$||M_{yz}^{-1}|| \propto e^{-|y-z|/a} \ , \tag{4.28}$$

the source components located in the nearest neighborhood of $y$ contribute most to the noise and thus removing them is desired.
The lattice community has come up with several sophisticated approaches to reduce the stochastic noise.

### 4.6.1 Dilution/Partitioning

Keeping the above discussion in mind, an obvious way to decrease the stochastic noise is to separate the sink as much as possible from the sources. *Dilution* (or *Partitioning*) of the source vectors means that only part of the lattice sites or spin-color components are occupied [80, 81].
Filling only one or a few timeslices of the lattice is very common for many

applications. The sink is then only affected by noise located at these timeslices (see Fig. 4.5). The downside is that we now only have a timeslice-to-all propagator. To get the full all-to-all propagator we have to invert $N_t$ times, where $N_t$ is the number of timeslices, each time on a source vector filled at a different timeslice. Checking if the error has reduced by more than $\frac{1}{\sqrt{N_t}}$ reveals if diluting this way is profitable.
Dilution schemes used in this work are spin and color dilution. Only one spin or color component is filled on each site. Of course both can be combined, which leads to 12 sets, where in each only one spincolor component is occupied.

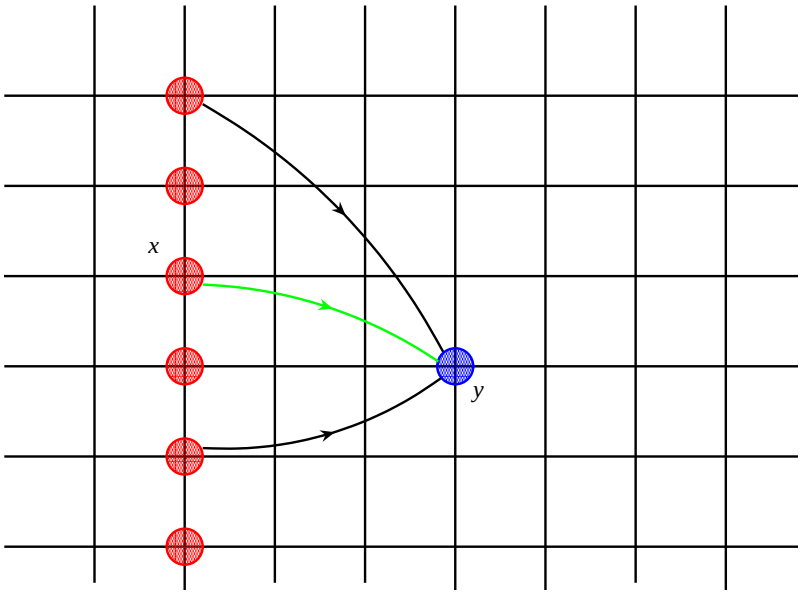


Figure 4.5: Two-dimensional sketch of a time diluted noise source (time axis from left to right). For the propagator from $x$ to $y$ only the green curve represents the signal, the black ones are pure noise.

### 4.6.2 Staggered Spin Dilution

In the standard spin dilution scheme non-zero noise spin components are the same for each site. So, for example, over the whole lattice only the first component in the first set, the second in the second set and so on (see Fig. 4.6).
Depending on the observable, however, it may be useful to alter the com-

| | | | | | | | |
|---|---|---|---|---|---|---|---|
| 1 | 1 | 1 | 1 | 1 | 1 | 1 | 1 |
| 1 | 1 | 1 | 1 | 1 | 1 | 1 | 1 |
| 1 | 1 | 1 | 1 | 1 | 1 | 1 | 1 |
| ... | | | | | | | |

Figure 4.6: Two-dimensional, schematic sketch of standard spin dilution for a specific set. The numbers indicate the spinor component filled at the specific lattice site.

ponent to be filled within a specific set. For heavy quarks, the coupling between the upper and the lower two components of the Dirac spinor is small. As we are simulating charm quarks, which can be regarded as heavy, we can benefit from this circumstance by choosing an advanced spin dilution scheme.

As we have seen above, the closer the source to the sink site, the more noise is induced. Based on this fact, we introduced the *Staggered Spin Dilution (SSD)* [82] scheme. The idea is to put those source spin components, which couple weakly, next to each other in spacetime. That is, we place upper next to lower components and vice versa. As stated above, the largest noise for a specific site is induced by the source sites in its nearest neighborhood. However, if this noise originates from a spin component from the other half of the spinor, it couples with an amplitude inversely dependent on the quark mass.

Two versions, *off-diagonal Staggered Spin Dilution (odSSD)* and *off-block-diagonal Staggered Spin Dilution (obdSSD)* are sketched in Fig. 4.7. Fig. 4.8 shows the corresponding coupling strengths in a $2 \times 2$ block. The red lines indicate strong couplings, the green ones weak couplings. Theoretically, the obdSSD version should result in the least noise as only weak couplings appear in the nearest neighborhood.

However, this estimation heavily depends on the structure of the Dirac matrix and the involved Gamma structure. Therefore an *a priori* prediction about the efficiency of a specific scheme is hardly possible.

An object frequently appearing in this work is the pseudoscalar loop $\mathrm{Tr}(\gamma_5 M^{-1})$. In the used spinor representation $\gamma_5$ is diagonal, which renders the above estimation reasonable for this quantity. For other, non-diagonal Gamma structures other staggered spin dilution schemes may turn out more

effective.

| | | | | | | | |
|---|---|---|---|---|---|---|---|
| 1 | 2 | 3 | 4 | 1 | 2 | 3 | 4 |
| 2 | 3 | 4 | 1 | 2 | 3 | 4 | 1 |
| 3 | 4 | 1 | 2 | 3 | 4 | 1 | 2 |
| ... | | | | | | | |

| | | | | | | | |
|---|---|---|---|---|---|---|---|
| 1 | 3 | 2 | 4 | 1 | 3 | 2 | 4 |
| 3 | 2 | 4 | 1 | 3 | 2 | 4 | 1 |
| 2 | 4 | 1 | 3 | 2 | 4 | 1 | 3 |
| ... | | | | | | | |

Figure 4.7: Two-dimensional, schematic sketch of off-diagonal staggered spin dilution (left) and off-block-diagonal staggered spin dilution (right), in each case for a specific set. The numbers indicate the spinor component filled at the specific lattice site.

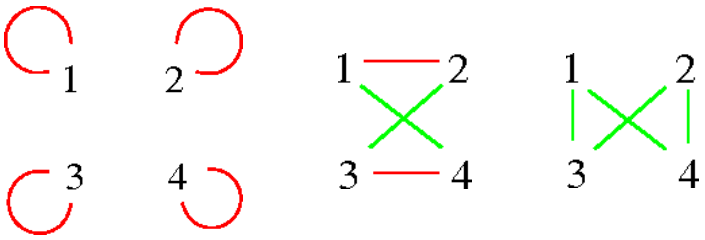


Figure 4.8: Sketch of the relative coupling strengths of standard (left), off-diagonal (middle) and off-block-diagonal (right) spin dilutions. The numbers ticket the different spinor components.

### 4.6.3 Hopping Parameter Acceleration

Especially for heavy quarks, the *Hopping Parameter Acceleration (HPA)* is a very efficient way to reduce noise from the nearby spacetime region around the sink [83]. It is based on the *Hopping Parameter Expansion* of a propagator of a Wilson-like Dirac operator

$$M_W = 1 - \kappa D\,, \tag{4.29}$$

where $D$ is the massless Dirac operator, which only couples nearest neighbors.
$\kappa$ is defined as

$$\kappa = \frac{1}{2(4 + m_0 a)} \tag{4.30}$$

where $m_0 a$ is the bare quark mass in lattice units (see (3.18)).
$M_W^{-1}$ can be expanded in powers of $\kappa$

$$\begin{aligned} M_W^{-1} &= (1-\kappa D)^{-1} = 1 + \kappa D + \ldots + (\kappa D)^{n-1} + \sum_{i=n}^{\infty} (\kappa D)^i \\ &= 1 + \kappa D + \ldots + (\kappa D)^{n-1} + (\kappa D)^n M_W^{-1} \\ &\Rightarrow (\kappa D)^n M_W^{-1} = M_W^{-1} - (1 + \kappa D + \ldots + (\kappa D)^{n-1}) \; . \end{aligned} \tag{4.31}$$

We see that by multiplying the propagator with the $n$-th power of $\kappa D$, we are left with the original propagator, minus terms that correspond to at most $n-1$ hops on the lattice. One can imagine a hypersphere with radius $n$ around the sink within which all contributions are cut out, see Fig. 4.9. One application of $\kappa D$ removes the blue contributions, two applications the green, three the yellow and so on. Actually, they are not completely removed, since they can travel a longer path to reach the sink, however, due to (4.28) these are then strongly suppressed.
Compared to dilution HPA is very cheap, since no extra inversions are necessary and the multiplication is relatively inexpensive in terms of computer time.
This method is best suited for heavy quarks, as the higher the quark mass the faster the hopping parameter expansion converges and thus the larger the eliminated noise contributions are.
Fig. 4.10 shows the effect of HPA for the Wilson operator on the stochastic variance of a pseudoscalar loop at the charm quark mass

$$\mathrm{Tr}(\gamma_5 M_W^{-1}) = \mathrm{Tr}\,(\gamma_5) + \kappa \mathrm{Tr}(\gamma_5 D) + \kappa^2 \mathrm{Tr}(\gamma_5 D^2) + \ldots \; . \tag{4.32}$$

Note that one application of $\kappa D$ has no effect, since $\mathrm{Tr}\,(\gamma_5)$ is zero anyway. The relative variance reduction decreases with increasing powers of $\kappa D$, which confirms that removal of nearby noise is crucial. Using the Wilson operator one is allowed to apply $(\kappa D)^8$ to $\mathrm{Tr}(\gamma_5 M_W^{-1})$, in order to subtract noise, only the ninth application affects the signal. For the Clover-Wilson action used in this work only two powers of $\kappa D$ leave the signal unchanged, as already $\mathrm{Tr}(\gamma_5 M^2_{\mathrm{Clover}}) \neq 0$[10].
HPA can help reducing the noise for many other observables, too. If one is interested in a correlator with time separation larger than some integer

[10] One can actually show that $\mathrm{Tr}(\gamma_5 M^2_{\mathrm{Clover}}) \propto F\widetilde{F}$. In principle these terms can be calculated by hand and added back again [84].

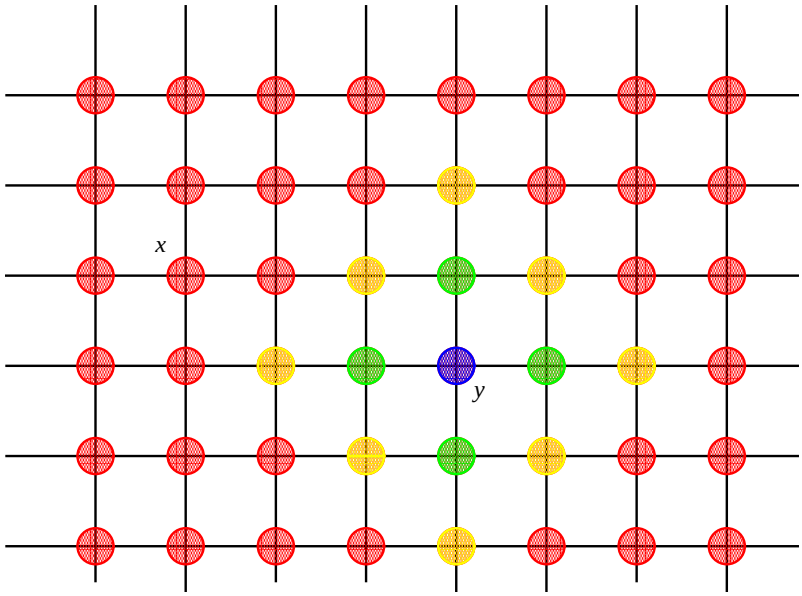


Figure 4.9: Two-dimensional sketch of the effect of HPA, where $y$ indicates the sink and $x$ some arbitrary source site. One application of $\kappa D$ removes the blue, two applications the green, three applications the yellow contributions.

$m$, contributions from regions $t < m$ are useless and just disturb the signal. Multiplying the involved propagators with $(\kappa D)^m$ removes a large portion of this unwanted noise [64].

### 4.6.4 Recursive Noise Subtraction

Another method that we introduced to minimize the stochastic variance is based on simple algebra and we called this *Recursive Noise Subtraction (RNS)* [82]. The idea is to calculate the off-diagonal terms of (4.26) by hand and to subtract them afterwards.
It is straightforward to write it down to first order with the following notation for the random contraction $\overline{|s\rangle\langle\eta|} \equiv \sum_i |s^i\rangle\langle\eta^i|$:

$$\begin{aligned} M^{-1}\overline{|\eta\rangle\langle\eta|} &= \overline{|s\rangle\langle\eta|} \\ M^{-1} &= \overline{|s\rangle\langle\eta|} + M^{-1}(1 - \overline{|\eta\rangle\langle\eta|}) \\ M^{-1} &\approx \overline{|s\rangle\langle\eta|} + \overline{|s\rangle\langle\eta|}(1 - \overline{|\eta\rangle\langle\eta|}) \\ &= \overline{|s\rangle\langle\eta|}\ (2 - \overline{|\eta\rangle\langle\eta|}) \end{aligned} \tag{4.33}$$

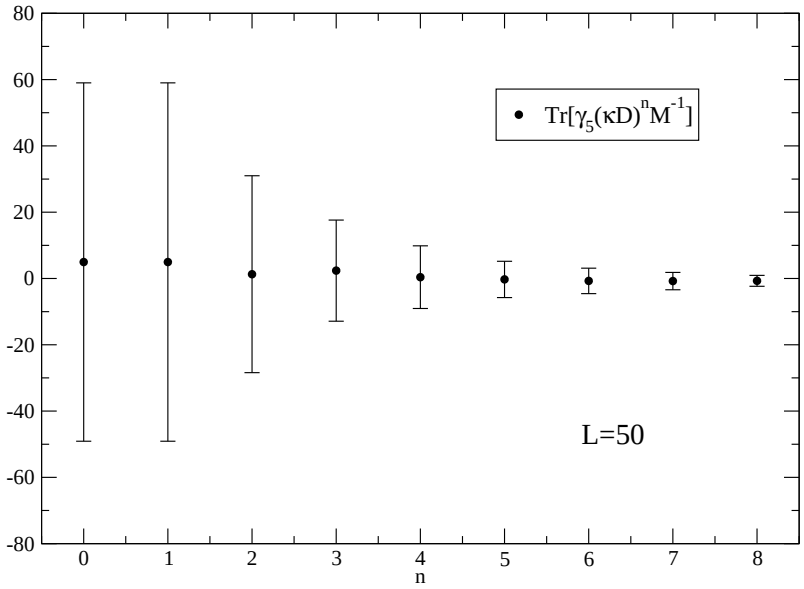


Figure 4.10: Plot of $\mathrm{Tr}(\gamma_5 M_W^{-1})$ (arbitrary scale) against the power of $\kappa D$ applied. The number of stochastic estimates is $L = 50$.

The scatter plot on the right side of Fig. 4.11 makes the correlation between the naive estimate and the first order noise term evident for the pseudoscalar loop. Since the two quantities plotted are anti-correlated, adding them together brings $\mathrm{Tr}(M^{-1}\gamma_5)$ closer to its obliged value of zero.
We assumed a correlation angle of $\pi/2$, but one could in principle do a fit to $\alpha\ \overline{|s\rangle\langle\eta|} + \beta\ (\overline{|s\rangle\langle\eta|} - \overline{|s\rangle\langle\eta|}\ \overline{|\eta\rangle\langle\eta|})$ and work with optimal $\alpha$ and $\beta$. This can naturally be generalized to any order.
Please note that also this method only requires cheap vector multiplications and no additional inversions.

### 4.6.5 Truncated Solver Method

Unlike the previous methods, the point of the *Truncated Solver Method (TSM)* is not to remove the offdiagonal noise terms, but to exploit the fact that solvers typically converge to the correct result within an accuracy of the size of the stochastic error after a relatively small number of iterations [85, 77]. The dependence of the scalar loop $\mathrm{Tr}(M^{-1})$ on the number of iteration steps is shown in Fig. 4.12 for the CG inverter and the BiCGStab inverter. The latter one is used throughout due to its superior performance.

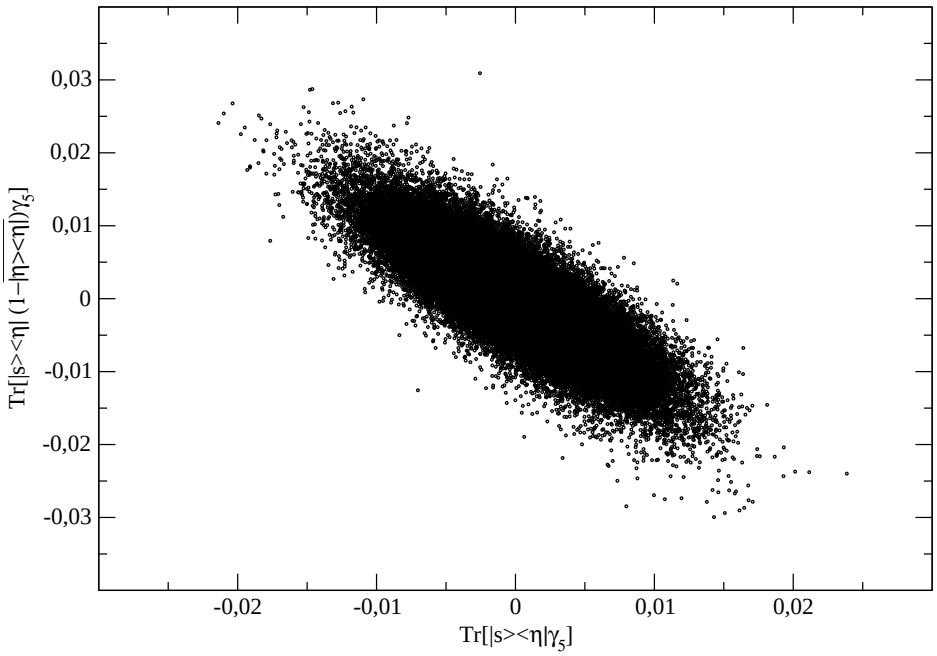


Figure 4.11: Scatter plot for the RNS to first order applied to the pseudoscalar loop.

Its non-monotone convergence is not precarious for our purposes.
However, stopping the inverter at some $n_t$ can lead to a systematic bias. To correct for this, the difference to the converged value is computed, but only with much less stochastic estimates, since this is a relatively small number:

$$M^{-1} \approx \frac{1}{N_1} \sum_{i=1}^{N_1} s_t^i \eta^{i\dagger} + \frac{1}{N_2} \sum_{i=N_1+1}^{N_1+N_2} (s_c^i - s_t^i) \eta^{i\dagger} \ , \tag{4.34}$$

where the subscripts $c$ and $t$ indicate the converged and the truncated vectors, respectively.
Ideally, one will generate a large number $N_1 \gg N_2$ of cheap estimates at small $n_t$ and then remove the bias by correcting with a small number $N_2$ of expensive solutions to machine precision. In order to guarantee this procedure is unbiased, the noise vectors for both parts have to be uncorrelated.
One main virtue of TSM is that it can be used for any fermion action, not only for ultra-local ones.

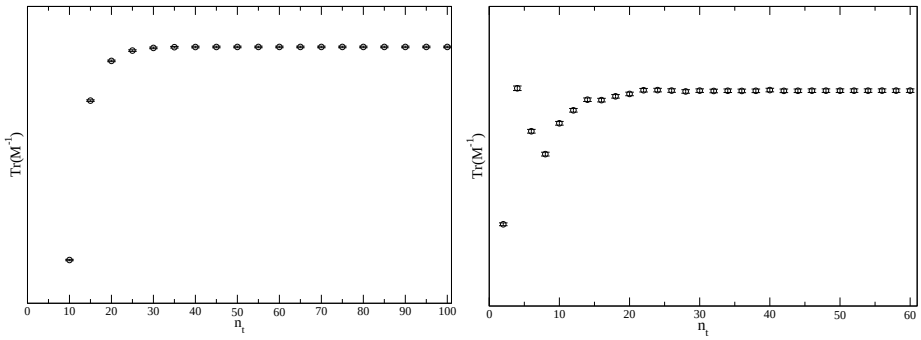


Figure 4.12: Dependence of the scalar loop on the number of iteration steps for the the CG inverters(left plot) and the BiCGStab inverter(right plot).

### 4.6.6 Overview

This section gives a brief overview over all tested improvement schemes (including standard dilution) for the disconnected part of the $\eta_c$ two-point function $\langle\, \mathrm{Tr}(M^{-1}\gamma_5)\, \mathrm{Tr}(M^{-1}\gamma_5)\, \rangle$. It is important to have two uncorrelated sets of estimates for the source and sink loops in order to avoid unwanted connected contributions.

Table 4.1 shows the effective gain for each method, i. e. the extra computational cost is already divided out (except for multiplying with $\kappa D$). $m$ is the power of $\kappa D$ applied to the sink vector. Using the Clover action to calculate $\mathrm{Tr}(M^{-1}\gamma_5)$ restricts $m < 3$ as mentioned above.

With color and staggered-spin dilution and two applications of $\kappa D$ we obtain a net gain factor of almost 12.

In Fig. 4.13 the $\eta_c$ disconnected correlator is shown both without any dilution and with color-off-blockdiagonal staggered-spin dilution on a single configuration. The number of estimates is 50. Although the signal is not good for either case, one can see the reduction of the variance and the smoothing of the correlator with dilution applied.

## 4.7 Smearing

The variational method, as the central tool of our analysis, works best if the operator basis is properly adjusted to the problem under consideration. This

| m | no | spin | color | color + spin | odSSD | obdSSD | obdSSD + color | RNS |
|---|---|---|---|---|---|---|---|---|
| 0 | 1 | 1.43 | 1.80 | 2.52 | 2.30 | 1.97 | 3.63 | 1.87 |
| 2 | 2.89 | 6.32 | 5.06 | 10.24 | 5.42 | 7.16 | 11.80 | 5.44 |

Table 4.1: Effective gain of noise reduction methods tested on the pseudoscalar disconnected correlator at the charm quark mass where the Clover action was used. $m$ denotes the number of $\kappa D$ applications.

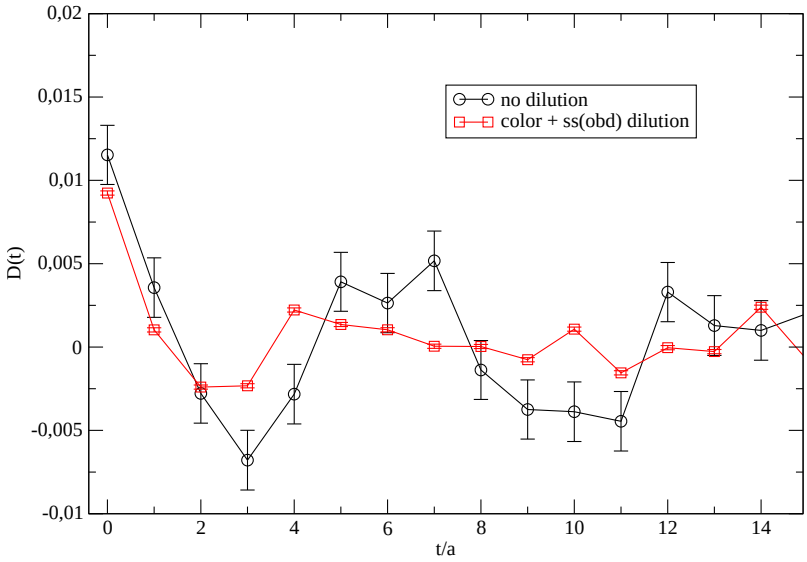


Figure 4.13: The pseudoscalar disconnected correlator at the charm quark mass without and with color-obdSS dilution. The number of stochastic estimates is 50.

means that we provide suitable building blocks, from which the diagonalization procedure is able to construct good approximations of the eigenstates. As the wavefunctions of physical eigenstates are (most likely) not ultralocal objects, including interpolators with finite spatial extent in the basis is appropriate. How to tinker these operators is shown in the subsequent sections.

### 4.7.1 Fermion Field Smearing

In order to generate extended operators we apply several steps of *Wuppertal smearing* [86] to the fermion field $\phi$:

$$\phi_x^{(n+1)} = \frac{1}{1+6\kappa}\left(\phi_x^{(n)} + \kappa \sum_{j=\pm 1}^{\pm 3} U_{x,j}\phi_{x+a\hat{\jmath}}^{(n)}\right), \tag{4.35}$$

where $n$ indicates the number of iterations, $\kappa$ the smearing parameter and $U$ the corresponding (smeared)[11] link variable. After one application the new fermion field at $x$ is a sum of the original field at $x$ plus nearest neighbor terms weighted by $\kappa$ and connected by corresponding link variables, see Fig. 4.14. The inclusion of the links is necessary to maintain gauge invariance.

For $n \to \infty$, $\phi$ approximates a Gaussian distribution.

By adjusting $\kappa$ and $n$ we can control the overlap of our trial wavefunctions with the physical states. Using a local operator for a two-point function in most cases leads to an effective mass with a significant curvature for small Euclidean times. A few iterations of smearing can help to flatten the effective mass (see (4.6)) from the beginning, which means that the overlap with higher excited states is suppressed, see Fig. 4.15. The black effective mass curve comes from a correlator with a local source and a local sink, the red one from a local source and a moderately smeared sink, the green one from a local source and a strongly smeared sink[12].

To understand the dependence of the coupling to the different excitations and the amount of smearing, consider Fig. 4.16. In each plot we sketch the three lowest lying radial excitations in a specific channel, labeled 1S, 2S and 3S, according to hydrogen eigenstates, which might serve as a reasonable approximation for heavy, dominantly $q\bar{q}$ systems like charmonia. Accordingly, the 1S has zero, the 2S one and the 3S two nodes in its wavefunction. Since a local operator corresponds to a Kronecker Delta at the origin, it has significant overlap with all three states, explaining the strong curvature of the effective masses coming from these operators. If we employ a trial wavefunction with non-zero spatial extent (labeled as "narrow"), the overlap with

[11] See next section.

[12] If one has the choice, smearing the sink instead of the source is much cheaper, as for different smearing parameters no additional inversions are necessary (when using one-to-all propagators).

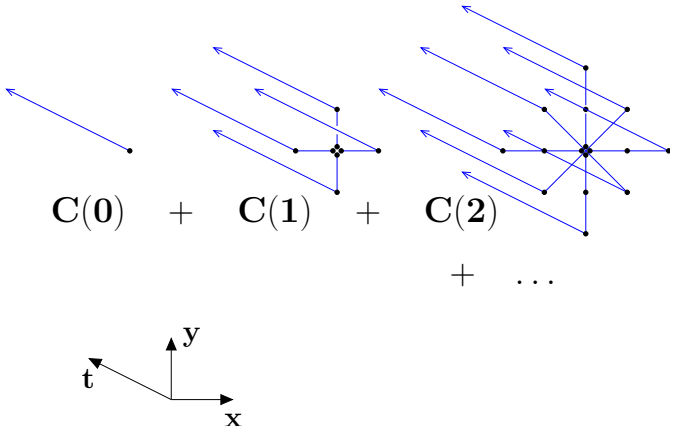


Figure 4.14: Visualization of the smearing process. Instead of using a point like source/sink $C(0)$, we allow the quark to jump one step ($C(1)$), two ($C(1)$), ... steps with a certain amplitude $\kappa$ before time propagation starts/after time propagation ends.

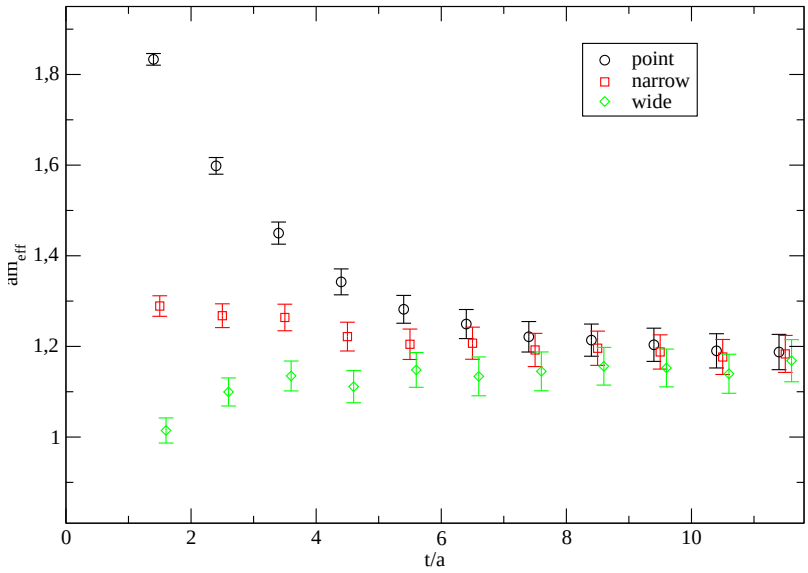


Figure 4.15: Effective masses of a correlator with a local source and a local, a narrow smeared and a wide smeared sink.

the ground state remains large, whereas the convolutions with the first and second excitation have opposing contributions, partly canceling each other. Using a smearing function with even larger extent (labeled as “wide”) leads

to an overall negative overlap with the first excitation, which explains the respective effective mass approaching from below in Fig. 4.16.
In general, a solid operator basis should contain operators resulting in all three types of effective mass curvatures, in order to grant the system enough freedom to reconstruct the eigenstates. The smearing parameters in our simulations are tuned to meet these requirements.

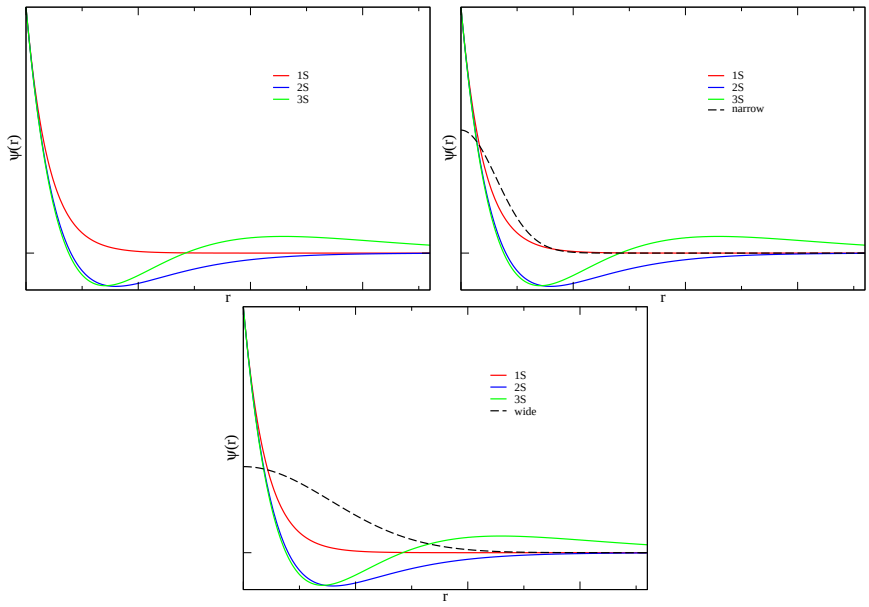


Figure 4.16: Sketch of the three lowest lying radial excitations of a dominantly $q\bar{q}$ state, together with a narrow (top right plot) and wide (bottom plot) smeared trial wavefunction.

### 4.7.2 Gauge Field Smearing

From (4.35) we know that smearing the fermion fields requires the inclusion of link variables to preserve gauge invariance. However, on a usual, unsmeared gauge configuration these are subject to rather large quantum fluctuations, which can disturb the shape of our trial wavefunction.
By *APE smearing* [87, 88, 89] the configurations we hope to average out these fluctuations. For spatial p-APE smearing the link is replaced by a sum over the original link and the six perpendicular staples connecting its

endpoints, and then projected back to $SU(3)$:

$$\begin{aligned} V_{x,i}^{(n+1)} &= U_{x,i}^{(n)} + \alpha \sum_{|j|\neq i} U_{x,j}^{(n)} U_{x+a\hat{\boldsymbol{\jmath}},i}^{(n)} U_{x+a\hat{\boldsymbol{\imath}},j}^{(n)\dagger} \\ U_{x,i}^{(n+1)} &= P_{SU(3)} V_{x,i}^{(n+1)} , \end{aligned} \tag{4.36}$$

where $\alpha$ is the weighting factor of the neighboring paths. The projection is done by maximizing $\mathrm{ReTr}[X V_{x,i}^{(n+1)}]$ for $X \in SU(3)$ and using $X$ as new link variable $U_{x,i}^{(n+1)}$.

A measure to find out when enough smearing has been applied to the parallel transporters is the average spatial plaquette $\langle P_s \rangle$. As a rule of thumb, if $\langle P_s \rangle$ is close to one, the smearing procedure can be stopped. In Fig. 4.17 $\langle P_s \rangle$ is plotted against the number of APE smearing iterations on lattice ① (see App. A.1). Stopping at 15 iterations seems reasonable and the exact value of $\alpha$ appears to be rather irrelevant within a certain range, so we choose $\alpha = 2.5$ .

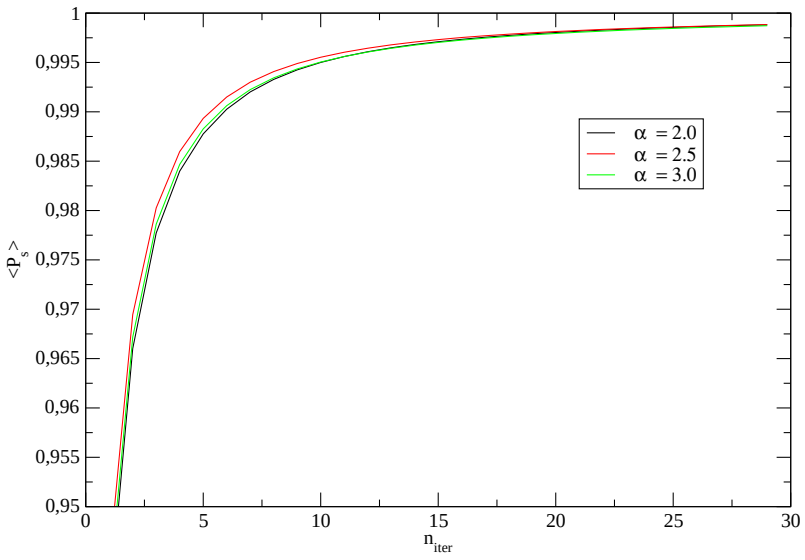


Figure 4.17: Plot of the average spatial plaquette against the number of APE smearing iteration steps on a $16^3 \times 32$ lattice for different values of $\alpha$.

Fig. 4.18 shows the effect of APE smearing on a trial smearing function for a single spin-color component. The left plot corresponds to an ordinary gauge field. There the wavefunction is ragged and seems quite unphysical,

whereas on the right plot, corresponding to an APE smeared field, it looks much smoother and is more likely to have good overlap with the physical states.
It is important to mention that the APE smeared fields are only used to improve our operators, but not to propagate the quarks. The inversions take place on the original gauge configuration. Otherwise the heavy quark-antiquark potential would be severely disturbed by the missing ultraviolet fluctuations averaged out by the smearing process.

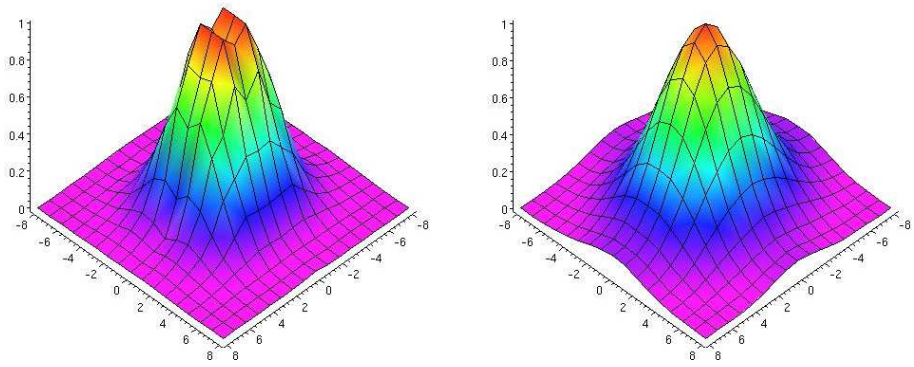

Figure 4.18: Plot of a single spin-color component of a smearing function on an ordinary gauge configuration (left hand side) and on an APE smeared gauge configuration (right hand side).

## 4.8 Setting the Quark Mass

In order to calculate the propagators necessary for the correlation functions, the inverter has to be fed with some parameters, amongst others the quark mass in lattice units.
To set the valence charm quark mass $m_{\text{charm}}$ or equivalently the charm $\kappa$ value $\kappa_{\text{charm}}$ (see (4.30)), we tune the linear combination $m_{\overline{1S}} = \frac{1}{4}m_{\eta_c} + \frac{3}{4}m_{J/\Psi}$ to its physical value, where the coefficients are due to the number of polarizations. Using only a single mass to tune to would have diminished our predictive power on the spectrum.
Fig. 4.19 shows the linear interpolation of $m_{\overline{1S}}$ to the physical value on lattice ③ (see App. A.1). $m_{\eta_c}$ and $m_{J/\Psi}$ have been obtained by single exponential fits to corresponding local-smeared correlators for two different values of $\kappa_c$.

The light quarks appearing in the mixing studies addressed in this work are simulated at the *unitary point*, i.e. $\kappa_l^{\text{valence}} = \kappa_l^{\text{sea}}$. Running at different $\kappa_l$ values in principle allows for a chiral extrapolation of the results. If valence light quarks are involved, we will explicitly comment on the impact of their masses.

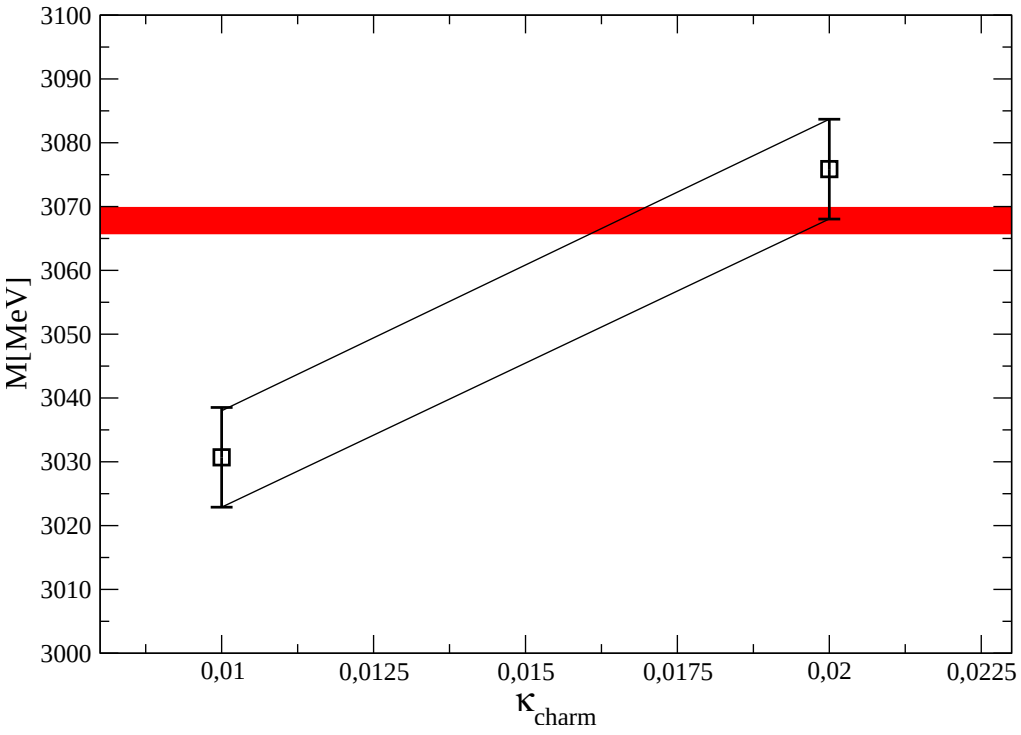


Figure 4.19: Plot to set the charm quark mass parameter. Dependence of $m_{\overline{1S}} = \frac{1}{4}m_{\eta_c} + \frac{3}{4}m_{J/\Psi}$ on $\kappa_{\text{charm}}$ together with the experimental value (red bar).

*Caution! Now there are only two possibilities: Either it works or it does not work.*
*– Jim Knopf und Lukas, der Lokomotivführer*
Michael Ende

# 5 Results

In this chapter all previously introduced methods and techniques are put in operation, in order to obtain information on the nature of charmonium states.
We start out by calculating the spectrum over almost the entire range of allowed quantum numbers accessible by lattice operators, including higher spin and exotic states. In this context we also address the 1S hyperfine splitting in detail.
The other main part of the analysis is devoted to the investigation of the inner structure of charmonium states. Some particularly interesting cases have been picked for a detailed discussion.

## 5.1 The Spectrum

Groundstate hadron masses are the simplest fermionic quantities one can compute on the lattice. As we have seen, calculating excited state masses is a more delicate undertaking. With the help of the variational method, see Sec. 4.2, which helps us to master this task, the spectrum of both ground and excited charmonia is computed in the following on lattice ① (see App. A.1). For each continuum state we construct a three by three cross correlator matrix containing only one kind[1] of operator, but with different smearings, where the quark and the antiquark are smeared in the same manner. The smearing parameters have been optimized for each state separately as described in Sec. 4.7. In a three dimensional operator basis only the two lowest lying eigenstates can be extracted reliably, as the last state contained in the basis may suffer from severe contaminations of higher lying states.

[1] Here "kind" refers to the spin and color structure.

### 5.1.1 Operator Basis

The operators we use are based on [59], however, derivatives were symmetrized to allow for charge conjugation eigenstates also at finite momenta. The quark bilinears which we report here are displayed in Tab. 5.1, together with their irreducible lattice representations and the lowest spin continuum state which they couple to (see Sec. 4.1).

| name | $O_h$ repr. | $J^{PC}$ | state | operator |
|---|---|---|---|---|
| $\pi$ | $A_1$ | $0^{-+}$ | $\eta_c$ | $\gamma_5$ |
| $\rho$ | $T_1$ | $1^{--}$ | $J/\psi$ | $\gamma_i$ |
| $b_1$ | $T_1$ | $1^{+-}$ | $h_c$ | $\gamma_i\gamma_j$ |
| $a_0$ | $A_1$ | $0^{++}$ | $\chi_{c0}$ | $1$ |
| $a_1$ | $T_1$ | $1^{++}$ | $\chi_{c1}$ | $\gamma_5\gamma_i$ |
| $(\rho \times \nabla)_{\mathrm{T}_2}$ | $T_2$ | $2^{++}$ | $\chi_{c2}$ | $s_{ijk}\gamma_j\nabla_k$ |
| $(\pi \times D)_{\mathrm{T}_2}$ | $T_2$ | $2^{-+}$ | | $\gamma_4\gamma_5 D_i$ |
| $(a_1 \times \nabla)_{\mathrm{T}_2}$ | $T_2$ | $2^{--}$ | | $\gamma_5 s_{ijk}\gamma_j\nabla_k$ |
| $(\rho \times D)_{\mathrm{A}_2}$ | $A_2$ | $3^{--}$ | | $\gamma_i D_i$ |
| $(b_1 \times D)_{\mathrm{A}_2}$ | $A_2$ | $3^{+-}$ | | $\gamma_4\gamma_5\gamma_i D_i$ |
| $(a_1 \times D)_{\mathrm{A}_2}$ | $A_2$ | $3^{++}$ | | $\gamma_5\gamma_i D_i$ |
| $(a_1 \times B)_{\mathrm{T}_2}$ | $T_2$ | $2^{+-}$ | exotic | $\gamma_5 s_{ijk}\gamma_j B_k$ |
| $(b_1 \times \nabla)_{\mathrm{T}_1}$ | $T_1$ | $1^{-+}$ | exotic | $\gamma_4\gamma_5\epsilon_{ijk}\gamma_j\nabla_k$ |

Table 5.1: Interpolating fields in use ($s_{ijk} = |\epsilon_{ijk}|$). For the operators the quark fields have been omitted.

$\nabla$ represents a covariant derivative, $D$ and $B$ symmetric and antisymmetric combinations of it:

$$D_i = s_{ijk}\nabla_j\nabla_k \tag{5.1}$$

$$B_i = \epsilon_{ijk}\nabla_j\nabla_k \tag{5.2}$$

with $s_{ijk} = |\epsilon_{ijk}|$.
The $B$ field can be interpreted as a valence gluonic component, supposedly resulting in a large coupling of the corresponding operator with hybrid

states. The exotic $2^{+-}$ state, for instance, can only be accessed through operators containing higher order derivatives.
Some lower spin states can be interpolated by operators with a fairly simple Gamma structure, leading to a superior signal to noise ratio compared to the higher spin states. The scalar, which is typically fairly noisy, constitutes an exception in this respect.
Some effective masses of correlators built from the operators in Tab. 5.1 are shown in Fig. 5.1. For each channel all three eigenvalues are plotted, however, we only fit to the two lowest lying ones. Fit ranges are indicated by the blue lines, where their widths correspond to the fit error, which was determined on 100 jackknife subsamples. The normalization timeslice $t_0$ is given, too.
The values of the fitted masses, together with the fit ranges, are given in Tab. 5.2.

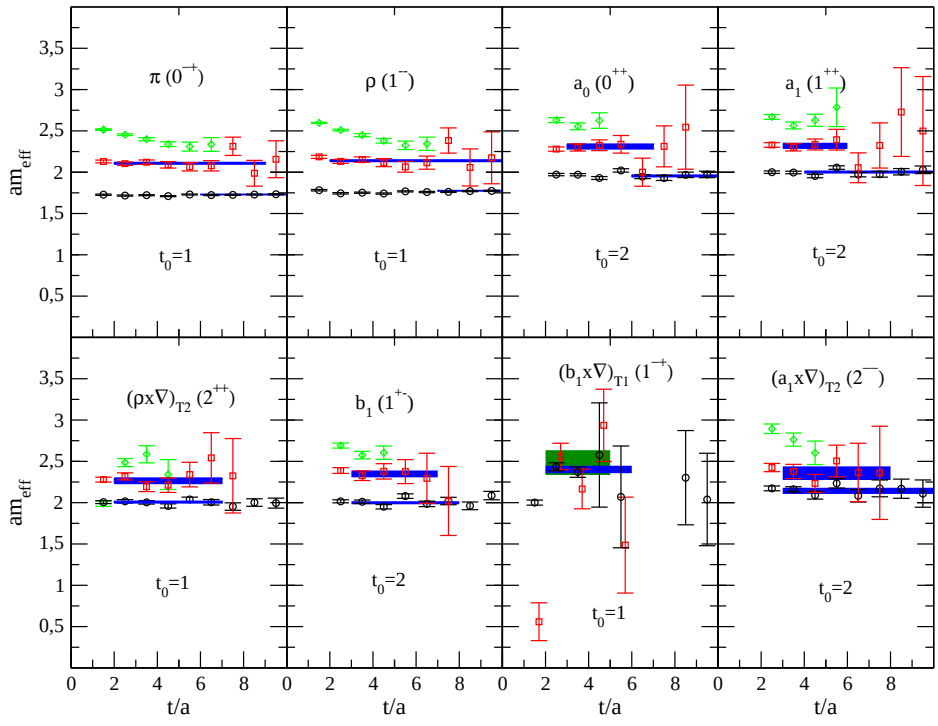


Figure 5.1: Effective masses from the three dimensional operator basis. Fit ranges and errors are indicated by horizontal lines. The $t_0$ values refer to the respective normalization timeslices.

| operator | $J^{PC}$ | $t_0$ | $m_{\lambda=1}$ | fit range | $m_{\lambda=2}$ | fit range |
|---|---|---|---|---|---|---|
| $\pi$ | $0^{-+}$ | 1 | 2993(4) | 5-12 | 3645(19) | 1-8 |
| $\rho$ | $1^{--}$ | 1 | 3070(6) | 7-12 | 3699(24) | 1-7 |
| $b_1$ | $1^{+-}$ | 2 | 3457(22) | 2-7 | 4060(65) | 1-5 |
| $a_0$ | $0^{++}$ | 2 | 3381(19) | 4-12 | 3996(48) | 1-5 |
| $a_1$ | $1^{++}$ | 2 | 3462(20) | 3-11 | 4011(52) | 1-5 |
| $(\rho \times \nabla)_{T_2}$ | $2^{++}$ | 1 | 3471(19) | 1-6 | 3917(46) | 1-6 |
| $(\pi \times D)_{T_2}$ | $2^{-+}$ | 1 | 3756(32) | 1-9 | 3995(141) | 1-6 |
| $(a_1 \times \nabla)_{T_2}$ | $2^{--}$ | 2 | 3706(27) | 1-10 | 4076(83) | 1-6 |
| $(\rho \times D)_{A_2}$ | $3^{--}$ | 1 | 3782(35) | 1-8 | 4815(92) | 1-6 |
| $(b1 \times D)_{A_2}$ | $3^{+-}$ | 1 | 3995(50) | 2-6 | 5365(76) | 1-3 |
| $(a_1 \times D)_{A_2}$ | $3^{++}$ | 2 | 3993(54) | 1-5 | 5008(287) | 1-4 |
| $(b_1 \times \nabla)_{T_1}$ | $1^{-+}$ | 1 | 4154(54) | 1-5 | 4297(181) | 1-4 |
| $(a1 \times B)_{T_2}$ | $2^{+-}$ | 1 | 4614(220) | 1-9 | 4643(254) | 1-8 |

Table 5.2: Fitted masses for the first two eigenvalues in each channel. The normalization timeslice $t_0$ and the corresponding fitting range are also given. Errors are only statistical.

Ground state and first excitation of the S- and P-waves display good signals with stable plateaus to fit. The effective masses of higher spin states are naturally noisier and thus make fitting more difficult.
An especially interesting channel is $1^{-+}$. Although this is an exotic quantum number, its states couple to the $(b_1 \times \nabla)_{\mathrm{T}_1}$ operator, which does not contain an explicit chromomagnetic field. However, already $\nabla$, due to its covariant construction, contains link variables, which can represent gluonic excitations. The putative best suited operator $(\epsilon_{ijk}\gamma_j B_k)_{\mathrm{T}_1}$, containing an explicit $B$ field, actually yields very poor signals.
The effective masses emerging when using the $(b_1 \times \nabla)_{\mathrm{T}_1}$ operator admittedly is not outstanding either, but can be fitted within reasonable errors. The two lowest lying states are very close, within the errors their effective masses are in fact overlapping. This might be a hint to the hybrid nature of this channel. Hybrid potentials are much flatter than $q\bar{q}$ potentials [90], leading to smaller energy gaps between the eigenstates. In order to clarify this issue satisfyingly, larger values of $t_0$ were necessary. Increasing values of $t_0$ unfortunately also result in larger errors, which makes a fit unfeasible

with the given statistics.
The computed spectrum is plotted in Fig. 5.2, together with the experimental values. It is important to note that we were not too careful when setting the charm quark mass parameter and we therefore underestimate $m_{\overline{1S}}$ by about 15 MeV. However, this is still well within the accuracy of the lattice spacing determination and moreover will cancel in level splittings. So the whole spectrum should be shifted higher a bit.
Keeping this in mind, we observe all spin-averaged states below threshold coming out fairly consistent with the experimental data[2]. The mass for the 1S pseudoscalar is a bit overestimated, the one for the 2S lies on top of the PDG value. Shifting the calculated $J/\Psi$ 15 MeV higher brings it very close to the PDG value. Groundstate masses of $1^{+-}, 0^{++}$, $1^{++}$ and $2^{++}$ P-waves are typically too low. Regarding some of the interesting $XYZ$-states, we notice that we were not able to reproduce the $X(3872)$ in this purely $c\bar{c}$ operator basis, however, the $Y(3940)$ or the $Z(3934)$ can be associated with the first excitation of the $\chi_{c_2}$.
Note the overlapping of the two lowest lying states in the exotic channels. As mentioned above, this may arise from large hybrid contributions to these channels.
As a general uncertainty, our results lack a continuum extrapolation. This may push each state in the one or the other direction. One should also keep in mind that our lattice $D\overline{D}$ threshold is about 1 GeV above the physical one, so possible decay states are not covered. Furthermore, our simulation is performed with only two, quite heavy sea quarks, what might explain the underestimation of the finestructure splittings. The rather small lattice volume can be mentioned as another systematic error affecting our results.
In [92] a very similar approach was used to calculate the spectra of excited states, i.e. applying the variational method using a basis of optimized interpolating fields based on [59]. Although the number of different operators in each channel is larger than in our calculation, our results are competitive and in most instances agree, albeit with larger error bars due to an order of magnitude lower statistics. Their study relies on the (anisotropic) Clover action, whereas they neglect all sea quark contributions, which the authors see as the main reason for the fact that their excited states systematically come out too high with respect to quark potential model predictions and,

[2]Taken from *Particle Data Group (PDG)*[91].

where they exist, experimental numbers.

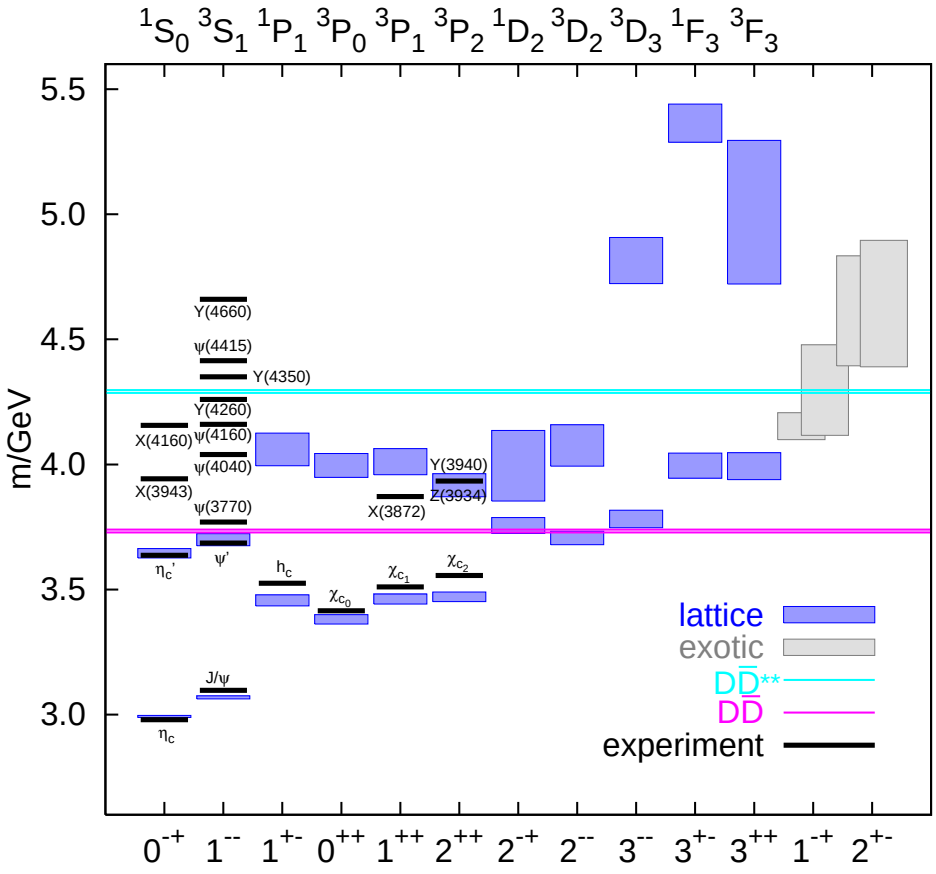


Figure 5.2: Predicted spectrum, together with the experimental values on lattice ① (see App. A.1). The $D\overline{D}$ threshold is the experimental one.

## 5.2 Pseudoscalar Wavefunctions

As argued in Sec. 4.2 couplings of the operators to the eigenstates can be calculated with the help of (4.13). These couplings can then in turn serve as coefficients in a linear combination of the trial wavefunctions in order to reconstruct the physical wavefunctions, or at least to approximate them.
Here we start from a four-dimensional basis of trial wavefunctions for the pseudoscalar channel $\Phi_j(\mathbf{x}) = \bar{c}(\mathbf{x})\gamma_5 c(\mathbf{x})$ with 0, 5, 10 and 40 (for each quark and antiquark) Gauss smearing iterations applied. By folding these with our eigenvectors we can attempt to construct the "wavefunctions" of

the physical states:

$$\Psi^{\alpha}(\mathbf{x}) = \sum_{j} \psi_j^{\alpha} \Phi_j(\mathbf{x}) \,, \tag{5.3}$$

where $\psi_j^{\alpha}$ is the $j$-th component of the eigenvector corresponding to state $\alpha$. In fact, only the (gauge invariant) probability densities are meaningful quantities. The used lattice unfortunately is too coarse to resolve the node structure of $|\Psi|^2$. However, observing that $|\Psi|^2$ for our APE smeared fields and $|\Psi|^2$ in the free case are very similar and additionally performing a consistency check on a Coulomb gauge fixed configuration, we plot the wavefunctions for the free case, where the nodes are clearly visible due to the sign change.

Fig. 5.3 shows one spin-color component of the normalized wavefunctions on a two-dimensional hyperplane for the lowest three pseudoscalar states. We neglect the statistical errors.

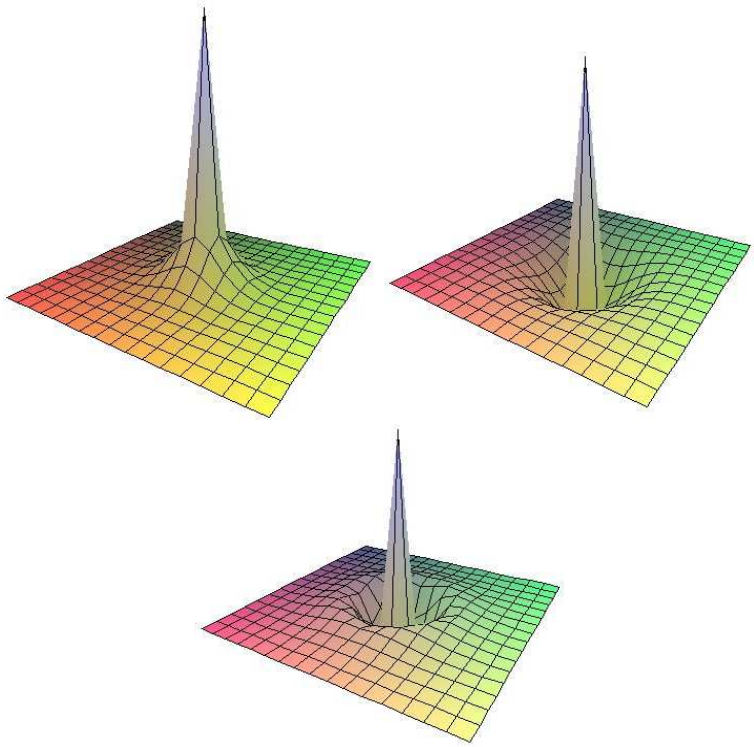

Figure 5.3: The 1S, 2S and 3S pseudoscalar "wavefunctions".

In spite of the small basis and lattice volume, the node structure is consistent with the 1S, 2S and 3S assignment, with no visible pollution from higher

Fock states or D-waves. For the 1S we obtain a root mean square $\langle r \rangle_{\mathrm{rms}} = \sqrt{\sum_V r^2 |\Psi|^2}$ of ca. 0.39 fm. This compares reasonably well with the infinite volume continuum potential model expectation of about 0.4 fm [93].
As a caveat, it is necessary to mention that the four dimensional basis of trial smearing functions obviously can only represent a relatively tiny number of all possible configurations. However, prior to the actual simulation these smearing functions are optimized as described in Sec. 4.7 to cover as much as possible of the physical wavefunction.
Furthermore pure charm quark-antiquark configurations of charmonia were assumed, which might be quite imprecise, especially for excited states. Later on we partly remove this bias by including other flavors (Sec. 5.5) and higher Fock states (Sec. 5.6) in our operator basis.

## 5.3 Mixing in the Vector Channel

Due to its direct production in electron-positron annihilation, the vector channel is rich in experimentally confirmed resonances, as can be seen from Fig. 5.2. Of great interest is the inner structure of these states, especially of the $\psi(2S)$ (or $\psi'$) and the $\psi(3770)$, which have a mass difference of only about 90 MeV. Whereas $J/\psi$ is supposed to be dominated by 1S quark-antiquark configurations, its excitations might exhibit a more complex structure.
As the name suggests, the $\psi(2S)$ is thought to be a radial excitation. Since $\psi(3770)$ is so close in mass, it is very improbable that it is excited in a further, higher radial vibration mode. One possibility which we investigate here is an orbital excitation where the quark-antiquark pair is in a relative D-wave.[3]
To this end, we tinker an operator basis consisting of three S-wave and two D-wave interpolators:

$$(c\gamma_i\bar{c})_0, (c\gamma_i\bar{c})_{20}, (c\gamma_i\bar{c})_{80}, (c\ s_{ijk}\gamma_j D_k\bar{c})_0, (c\ s_{ijk}\gamma_j D_k\bar{c})_{80} \qquad (5.4)$$

with $s_{ijk} = |\epsilon_{ijk}|$.
The subscripts indicate the number of smearing iteration steps. Originally,

[3] Remember that these statements cannot be understood in an absolute way, as mixing with other configurations is always present (see Sec. 2.4). Also $L$ is only a "good" quantum number in the $m \to \infty$ limit.

we also had in mind to include hybrid operators like $c\gamma_5 B_i \bar{c}$, but unfortunately these provided very poor signals throughout, independent of their smearing level.
The whole analysis was performed on lattice ② (see App. A.1) with $t_0 = 1$. A plot of the effective masses of the lowest four eigenvalues found in this basis are shown in Fig. 5.4. As expected, the second and third eigenvalues lie very close. The fourth eigenvalue might be identified with the $\psi(4040)$.
An inspection of the eigenvectors reveals the magnitude of overlap between the trial operators and the eigenstates, see (4.13). The Figures 5.5, 5.6 and 5.7 contain the corresponding plots.

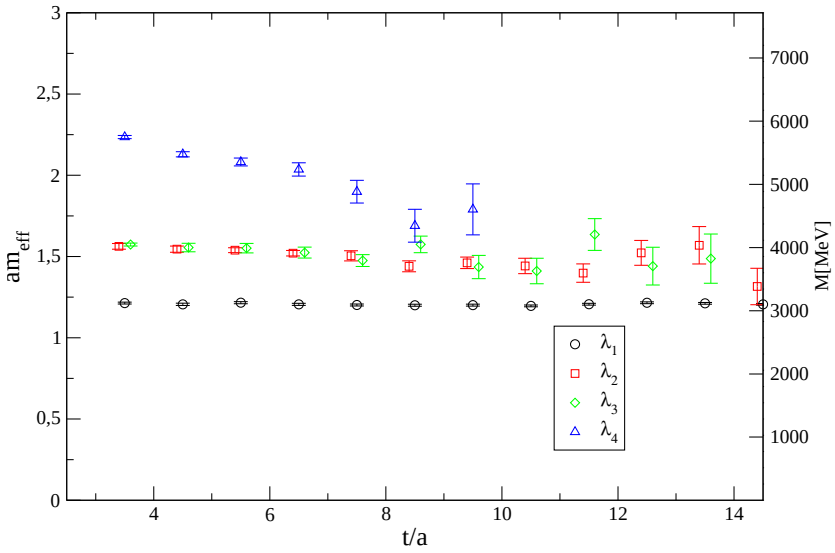


Figure 5.4: Effective masses of the four lowest lying states in the vector channel.

As the groundstate, the $J/\Psi$ not surprisingly has vanishing contributions from the two D-wave operators and exhibits pure S-wave character, where the extended S-wave operators dominate over the local one. Also the second eigenvalue has no contributions from the D-wave operators within the errors, but significant contributions from all three S-wave interpolators. Note the relative sign change between the local/narrow and the wide smeared operator leading to a node in the spatial wavefunction, similar to Fig. 5.3. This information suggests the $\psi(2S)$ assignment for this state.
On the other hand, the third eigenvalue only couples to the wide smeared D-wave operator, which obviously leaves it as a candidate for the $\psi(3770)$.
Our results compare reasonably well with the ones from [92]. Besides the

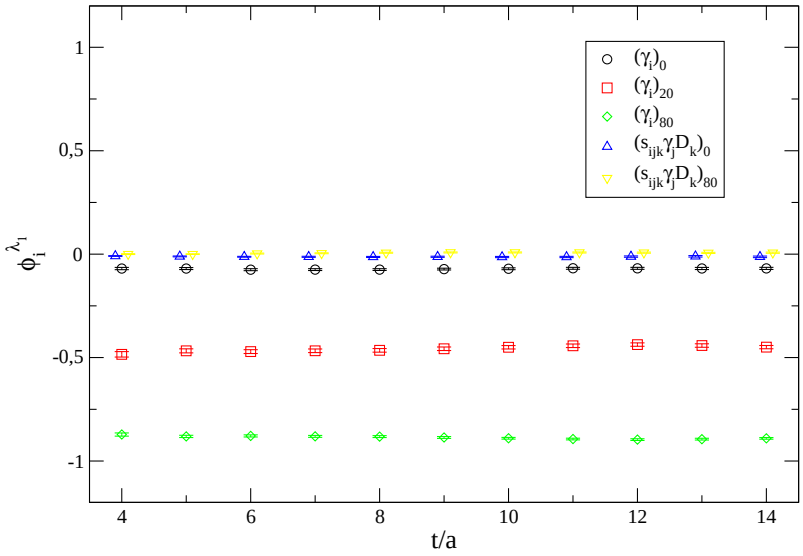


Figure 5.5: Eigenvector components of the first eigenvalue in the vector channel.

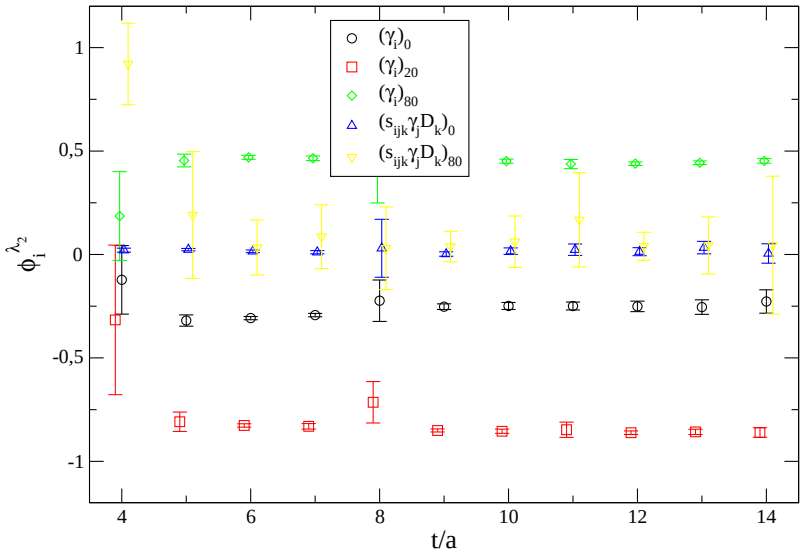


Figure 5.6: Eigenvector components of the second eigenvalue in the vector channel.

groundstate they also find a band of three almost degenerate states around 3800 MeV in the $T_1$ channel. Two of them are associated with $1^{--}$, whereas the third excited state is supposed to have $3^{--}$ continuum quantum numbers, since the used $T_1$ operators can have overlap with $3^{--}$ at finite lattice

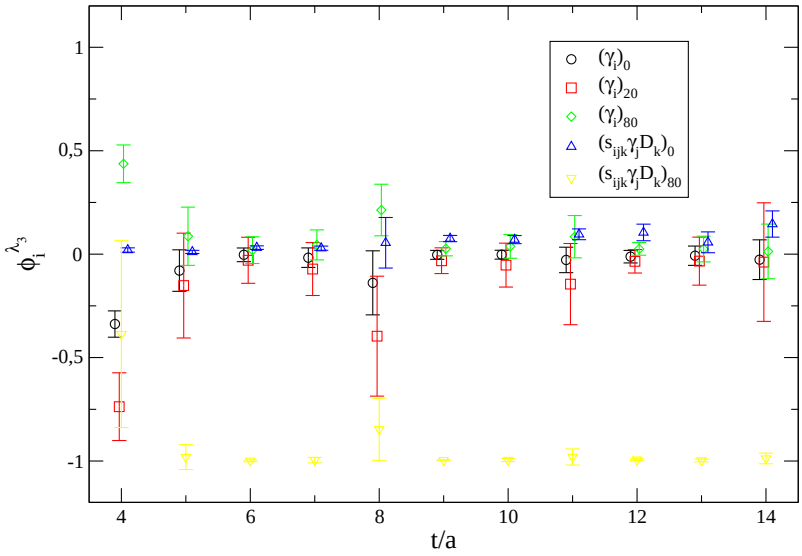


Figure 5.7: Eigenvector components of the third eigenvalue in the vector channel.

spacing (see 4.7).
Although the knowledge about the mixing in the vector channel is pretty interesting on its own, this represents only a beginning of the mixing studies of the subsequent sections.

## 5.4 Hyperfine Splitting

The hyperfine splitting, that is the mass difference between the $J/\Psi$ and the $\eta_c$, is still an open issue in the lattice community. In spite of great efforts (see [94, 95], for instance), all results are still short of the experimental value of $\Delta m_{1S} \approx 117$ MeV. Some progress has been achieved recently [96, 97], but the justification of the methods used there is still partly pending.
There are several systematics potentially responsible for the discrepancy between experiment and simulations.
First of all, taking the continuum limit may turn out to be crucial [97]. NRQCD calculations predict the splitting to be $\Delta m_{1S} = c_F/(6m_c^2)\langle\psi|V_4|\psi\rangle + \ldots$ , where $c_F V_4 = (32\pi/3)\alpha_s\delta^3(\mathbf{r})$ to leading order in perturbative QCD, making the strong short distance sensitivity of this quantity evident [12].
From this equation one can also tell the importance of the correct sea quark content. Simulations with too few or too heavy sea quark flavors exhibit

a wrong curvature of the running $\alpha_s(q)$ at high momenta, which in turn results in a relatively lower value for $\Delta m_{1S}$ [93]. Lattice ① was generated with two light quark flavors with a corresponding pion mass of about 1 GeV, which is not beneficial in this respect.
Another source of systematic error is the lack of disconnected diagrams. Due to the OZI rule, the state primarily affected by this is supposed to be the $\eta_c$ [98]. The impact of these diagrams on both the pseudoscalar and the vector channel has been found to be insignificant within errors of about 20 MeV [95]. The spectrum plotted in Fig. 5.2 does not contain such quark-antiquark annihilation diagrams; however, they will be included explicitly in the next section. In this context, the effect of the $\eta_c$ mixing with states having the same quantum numbers is investigated using the example of the $\eta'$. Mixing with glueballs may play an important role [99], too, but is not addressed in this work[4]. Presumably tiny, but maybe not negligible, effects from the axial anomaly to the pseudoscalar might favor a lattice formulation that respects exact chiral symmetry.
Keeping all the above shortcomings in mind, our values for the hyperfine splitting of $\Delta m_{1S} = 73(2)$ MeV on lattice ① and $\Delta m_{1S} = 88(4)$ MeV on lattice ② are not surprising.
In principle, a continuum extrapolation with the results for two different lattice spacings is possible, but fails due to the differing light quark masses. For the 2S hyperfine splitting we obtain $\Delta m_{2S} = 47(6)$ MeV on lattice ① and $\Delta m_{2S} = 56(8)$ MeV on lattice ②, in agreement with the experimental value of 49(5) MeV. Our failure to consistently underestimate this value as well might be explainable by $D\overline{D}$ threshold effects [100, 97] which we neglect due to our heavy sea quarks.

## 5.5 The $\eta_c - \eta'$ Mixing

As stated in the previous section, lattice calculations of the charmonium $S$-wave hyperfine splitting tend to underestimate the experimental value of 117 MeV. Now we take into account two potential sources of the discrepancy: quark annihilation diagrams and mixing with the $\eta'$ [82].
Before proceeding we want to point out a subtlety connected to the $\eta'$. The lightest pseudoscalar mesons can be arranged in $SU(3)$ flavor multiplets (see

[4] Actually, implicit glueball mixing is taken into account in Sec. 5.5.

Fig. 5.8). As we know from (2.30), combining a quark and an antiquark leads to one singlet and eight octet states. From the three states with strangeness $S = 0$ and electric charge $Q = 0$, the $\pi_0$ has isospin 1 and belongs to the octet. The remaining octet state is $\eta$ and the symmetric singlet is $\eta'$[5], whose wavefunction is given by [16][6]:

$$|\eta'\rangle = \frac{1}{\sqrt{3}} \left\{ |u^{\uparrow}\bar{u}^{\downarrow}\rangle + |d^{\uparrow}\bar{d}^{\downarrow}\rangle + |s^{\uparrow}\bar{s}^{\downarrow}\rangle \right\} , \tag{5.5}$$

where the arrows indicate the relative spin orientations.
This is the state $\eta_c$ is allowed to mix with.
However, since all configurations in use were generated with $N_f = 2$ sea quarks and furthermore valence strange quarks are not taken into consideration, we are effectively working in the $SU(2)$ flavor symmetry domain, whose $2 \times 2$ combinations can be grouped in three triplet states and one singlet state. This singlet is then just called $\eta$ or sometimes also $\eta_2$. Thus the lack of strange quarks in our simulations restricts us to the investigation of the mixing of $\eta_c$ and $\eta$.

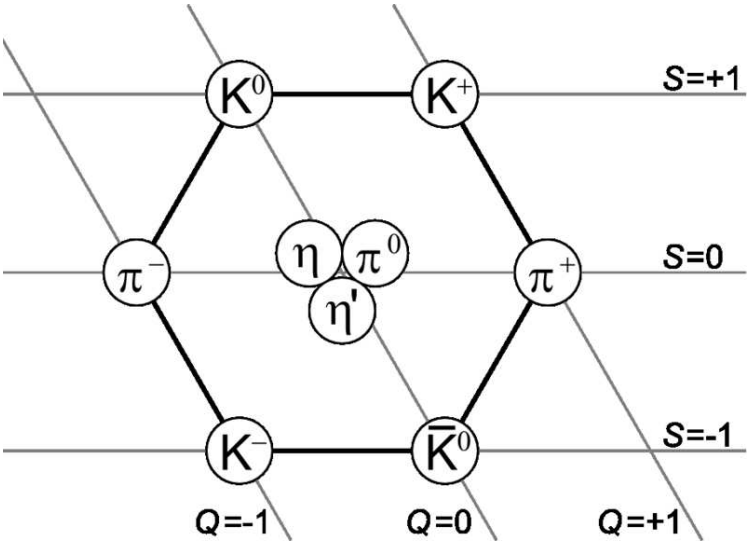


Figure 5.8: Lightest pseudoscalar mesons, classified according to their strangeness $S$ and electric charge $Q$ [101].

[5]Strictly speaking these are $\eta_8$ and $\eta_1$, respectively, which are allowed to mix due to the broken $SU(3)$ flavor symmetry.

[6]Of course, many other configurations can in principle contribute, see Sec. 2.4.

Another caveat is the nomenclature "$\eta_c - \eta$ mixing" itself. As both $\eta_c$ and $\eta$ are QCD eigenstates they do not mix via the strong interaction. So what we actually mean with this slightly careless terminology is the mixing between states created by $c\gamma_5\bar{c}$-type operators and states created by $q\gamma_5\bar{q}$.[7]
Let us for the time being pretend to be able to do a kind of perturbation theory for this mixing problem. Assuming a Hamiltonian $H = H_0 + \lambda H_1$, where $H_1$ is responsible for the mixing and $\lambda$ is some small coupling parameter[8], we can estimate the $|\eta_c\rangle$ wavefunction to first order[9]:

$$|\eta_c\rangle = \frac{1}{\mathcal{N}} \left( |c\bar{c}\rangle + \lambda \frac{\langle q\bar{q}|H_1|c\bar{c}\rangle}{E(c\bar{c}) - E(q\bar{q})} |q\bar{q}\rangle \right) , \qquad (5.6)$$

with a normalization factor $\mathcal{N}$.
While we do not know the functional form of $H_1$ or of the unperturbed wavefunctions, we can evaluate all the relevant matrix elements on the lattice. Figure 5.9 shows one possible lowest order graph responsible for this mixing. Note that two gluons are necessary as an intermediate state for conservation of quantum numbers. One important thing to note here is

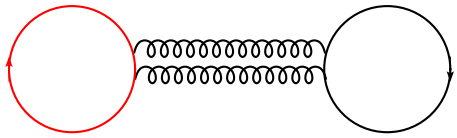

Figure 5.9: One possible lowest order graph responsible for the $\eta_c - \eta'$ mixing. The red lines correspond to charm quarks, the black to light quarks, the twiddled ones to gluons.

the dependence of the mixing on the light quark mass. With decreasing $m_q$, the denominator obviously becomes larger at constant $m_c$. However, also the mixing matrix element in the numerator is expected to increase since the probability for creating a light quark-antiquark pair should be inversely dependent on the light quark mass. Thus, it is *a priori* not clear which effect prevails and simulating at a smaller light quark mass would be necessary to clarify this issue.
We aim to calculate the coefficients in the expansion of the QCD eigenstates

[7] Naturally, all types of Fock states with the correct quantum numbers could be stated here. However the chosen ones are expected to dominate the respective wavefunctions.
[8] We cannot suppose $\lambda$ to be small *a priori* in the nonperturbative regime.
[9] Gamma structures are omitted for convenience.

in the trial interpolating fields nonperturbatively, by diagonalizing a matrix of cross correlators including both charmonium and light meson interpolators, three in each sector:
$(c\gamma_5\bar{c})_0$, $(c\gamma_5\bar{c})_{10}$, $(c\gamma_5\bar{c})_{80}$, $(q\gamma_5\bar{q})_0$, $(q\gamma_5\bar{q})_5$, $(q\gamma_5\bar{q})_{40}$,
where the subscripts indicate the number of fermion field smearing iterations.
In Fig. 5.10 we sketch the structure of the mixing matrix. The different smearing levels are omitted for the sake of clarity. Red lines represent charm quark propagators and blue lines light quark propagators. The prefactors are due to the two mass degenerate light sea quark flavors. The upper left corner contains the $c\bar{c}$, the lower right corner $q\bar{q}$ sector. Non-vanishing off-diagonal elements indicate mixing.

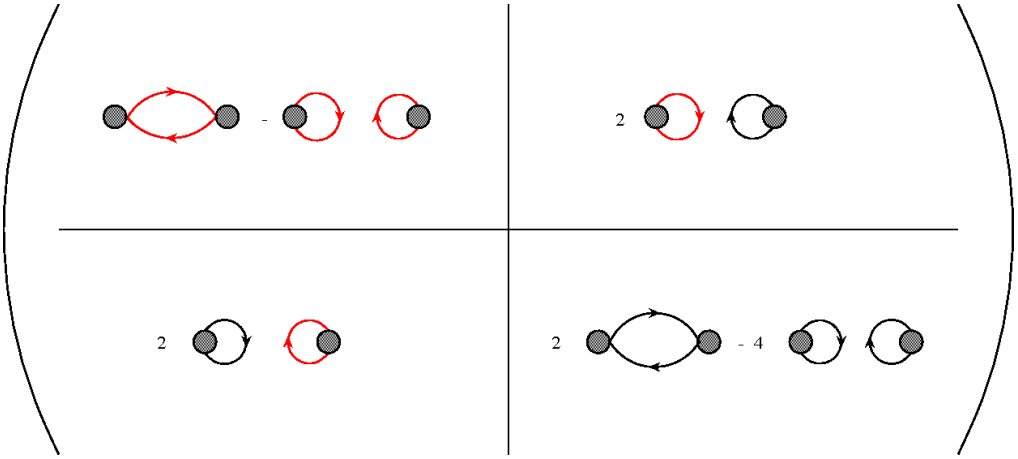


Figure 5.10: Cross correlator matrix for $\eta_c - \eta'$ mixing. Red lines represent charm quarks, black lines light quarks.

Note that already in the pure charmonium sector higher order mixing in the disconnected part might occur due to the existence of intermediate light quark loops (see Fig. 5.11). This is called implicit mixing [64], in contrast to the explicit mixing we construct in the off-diagonal elements. As a consequence, even in the $c\bar{c}$ correlator the light meson state will dominate asymptotically. Due to its naturally small coupling to charmonium interpolators and the poor signal to noise ratio at large Euclidean times, it is, however, very unlikely and in our case not possible to observe this.

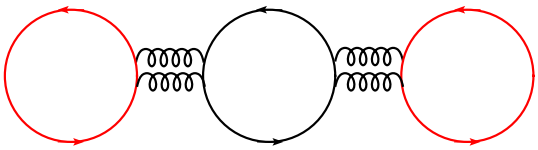

Figure 5.11: One possible graph responsible for implicit $\eta_c - \eta'$ mixing via light sea quark loops. The red lines correspond to charm quarks, the black to light quarks, the twiddled ones to gluons.

The variational method is applied to the mixing matrix by solving a generalized eigenvalue problem as discussed in Sec. 4.2.
Our strategy differs from that of many previous studies that utilized the variational method, insofar as our primary interest lies in the couplings and not only in the resulting spectrum.
We first determine the eigenvalues of the three by three submatrices within each of the flavor sectors, separately, in order to obtain an "unperturbed" spectrum. This is then used to identify the affiliation of the eigenvectors to the eigenstates. Finally, we will compare spectrum and eigenvector components, with the mixing elements switched on, to this unmixed reference point.
The estimation of the all-to-all propagators needed for both the charm and light disconnected loops has been improved by HPA, obdSS and color dilution, and first order RNS, see Sec. 4.6. For the light propagators TSM with $n_t = 25$ has been applied, additionally.
So we proceed as follows: we first determine the eigenvalues of the 3 by 3 submatrices separately within each of the flavor sectors, where for the moment we ignore the disconnected contribution in the charmonium sector, see Fig. 5.12. The light $\eta$ and its first excitation[10] $\eta'$ are the lowest two eigenvalues of the submatrix containing only light interpolators and $\eta_c$ and $\eta_c'$ within the charmonium sector. We find a diagonalization of the full 6 by 6 matrix to be numerically unstable and hence restrict ourselves to the basis of the states $(c\gamma_5\bar{c})_{10}$, $(c\gamma_5\bar{c})_{80}$, $(q\gamma_5\bar{q})_5$ and $(q\gamma_5\bar{q})_{40}$ for the full-fledged mixing analysis.
In the right hand side of Fig. 5.13 the effective masses of the lowest three eigenvalues obtained from this basis are shown together with the eigenvalues obtained above, ignoring the mixing effects.

[10] Not to be confused with the meson singlet in $SU(3)$ flavor.

The eigenvectors contain the detailed information about the mixing. We display the components of the ground state $\eta$ eigenvector in Fig. 5.14 and those of the $\eta_c$ eigenvector in Fig. 5.15.

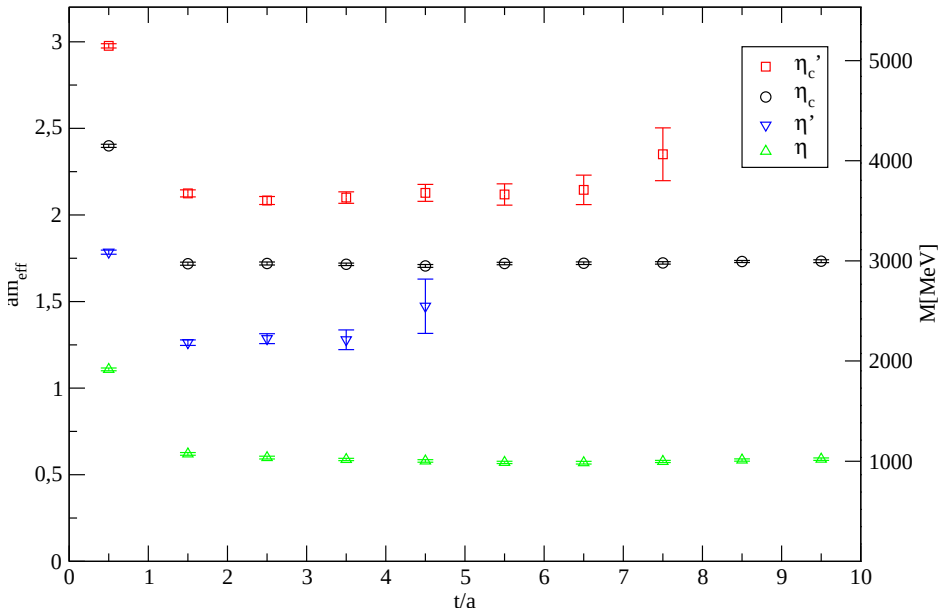


Figure 5.12: Effective masses of the eigenvalues of the submatrices.

Table 5.3 shows the fitted eigenvector components in the truncated basis. Indeed, the $\eta$ does not contain any statistically significant admixture from the $c\bar{c}$ sector and vice versa. The summed contribution from $c\bar{c}$ to the $\eta$ is 0.019(65), the one from $q\bar{q}$ to the $\eta_c$ is 0.021(51), thus both consistent with zero.

Just as well there is no significant shift of the $\eta_c$ mass when explicit mixing is turned on, the jackknifed mass difference is $m_{\eta_c}(\text{mixed}) - m_{\eta_c}(\text{unmixed}) = 11(24)$ MeV.

However, the unrealistically heavy pion mass might have affected our conclusion and runs at lattices with a lower pion mass must clarify this issue. Furthermore, mixing with other states like glueballs or higher Fock states deserves future attention. The latter one is addressed in the next section. Coupling to glueballs are, however, rather unlikely, if effects of diagrams like in Fig. 5.9 are small.

As a side result, we want to compare the submatrices spectra with and with-

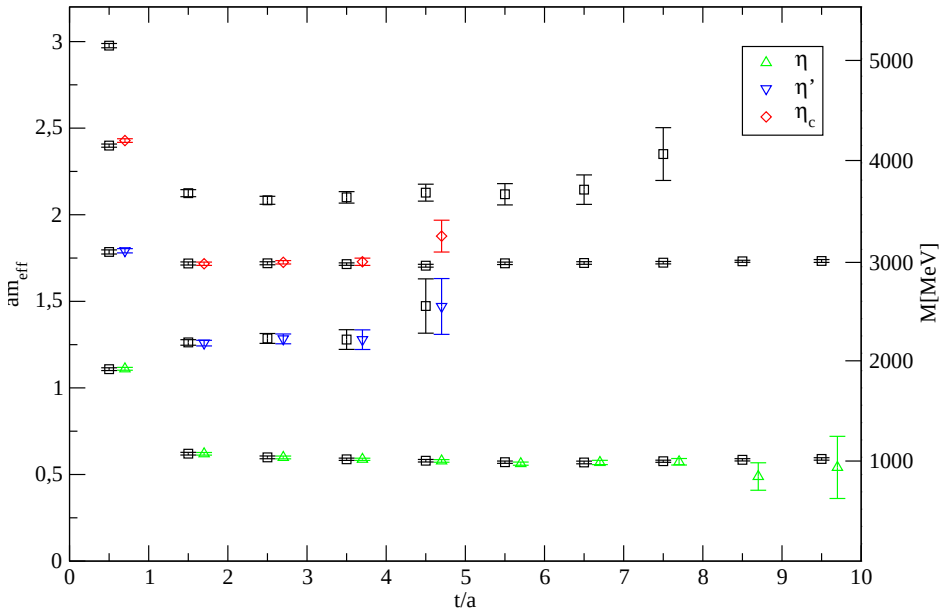


Figure 5.13: Effective masses of the eigenvalues of the full matrix. As a reference point the effective masses from the submatrices are plotted, too (black points).

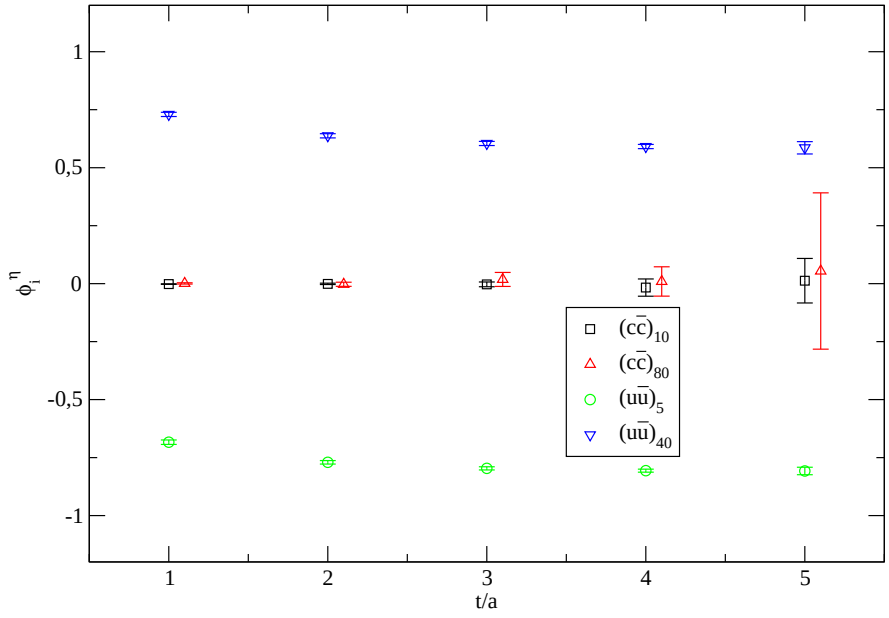


Figure 5.14: Eigenvector components of $\eta$ in the full basis.

out the inclusion of the respective quark-antiquark annihilation diagrams. Taking the disconnected part into account in the charmonium sector leads

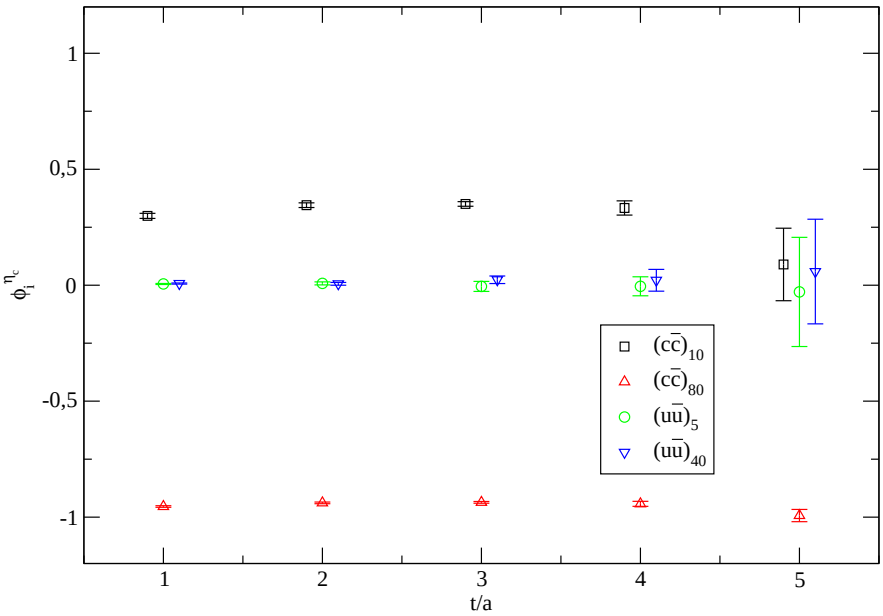


Figure 5.15: Eigenvector components of $\eta_c$ in the full basis.

| | $(c\bar{c})_{10}$ | $(c\bar{c})_{80}$ | $(q\bar{q})_5$ | $(q\bar{q})_{40}$ |
|---|---|---|---|---|
| $\eta$ | -0.017(37) | 0.009(63) | -0.806(1) | 0.591(9) |
| $\eta_c$ | 0.333(30) | 0.943(11) | -0.000(41) | 0.021(47) |

Table 5.3: Fitted eigenvector components of $\eta$ and $\eta_c$ coming from the diagonalization of the full matrix.

to tremendous errors already from timeslice two. As a consequence we were not able to discover any statistically significant flavor singlet effects on the hyperfine splitting.
The quality of the signal improves strongly for the light quark disconnected diagrams. Their inclusion results in a significant shift in the effective mass, see Fig. 5.16, which is quantified by a $\pi$-$\eta$ mass splitting of 52(13) MeV.

## 5.6 S-Wave Charmonia - $D\overline{D}$ Molecule Mixing

This section is closely related to the previous one, as we again want to investigate the allegedly subleading contributions to charmonia. Instead of the effects of annihilation and mixing with other flavors, now we have a look at higher Fock state contributions, namely molecules [102].

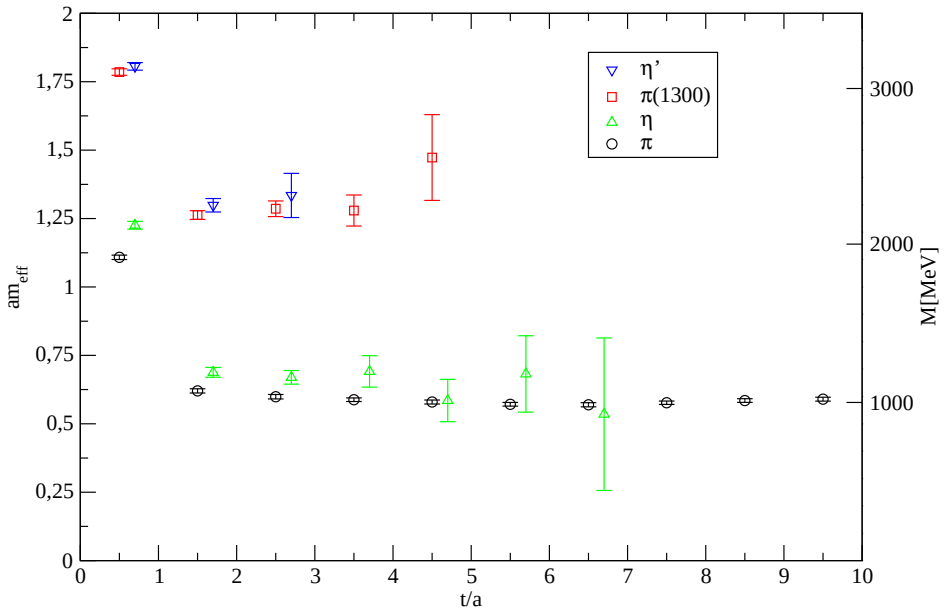


Figure 5.16: Effective masses of the eigenvalues from the light submatrix. Black and red points indicate the flavor non-singlet masses, green and blue the corresponding flavor singlet masses.

Charmonium states can decay into pairs of $D$ and $\overline{D}$ mesons if their masses are above the allowed decay thresholds [100]. In general $c\bar{c}$ states near threshold will also undergo mixing with $D\overline{D}$ molecular (or tetraquark) states, by creation and annihilation of light quark-antiquark pairs. We address this mixing in three different channels of phenomenological interest, $0^{-+}$, $1^{--}$ and $1^{++}$.

As in the previous section, the nomenclature has to be clarified. To take the pseudoscalar channel as an example, "$\eta_c$-$D_1\overline{D}^*$-mixing" virtually means mixing between states created by a $c\gamma_5\bar{c}$-type operator and by a $(c\gamma_5\gamma_i\bar{q})(\bar{c}\gamma_i q)$ molecule operator.

Again we can estimate the physical states by a fictitious perturbative treatment. We expect the physical $\eta_c$ wavefunction at first order to read,

$$|\eta_c\rangle = \frac{1}{\mathcal{N}}\left(|c\bar{c}\rangle + \lambda\frac{\langle c\bar{q}q\bar{c}|H_1|c\bar{c}\rangle}{E(c\bar{c}) - E(c\bar{q}q\bar{c})}|c\bar{q}q\bar{c}\rangle\right), \qquad (5.7)$$

with a normalization factor $\mathcal{N}$ and a (hopefully) small coupling constant $\lambda$ appearing in the mixing vertex of the Hamiltonian $H_1$, see Fig. 5.17.

In contrast to the $\eta_c - \eta'$ mixing, the dependence of the mixing strength on the light quark mass is evident. The mass difference obviously becomes

smaller with decreasing $m_q$, whereas the mixing amplitude gets enhanced, since it is easier to create a lighter quark-antiquark pair from the vacuum. Taking this into account we perform these runs on the lattice with the smallest pion mass available, namely on lattice ③, where $m_\pi \approx 300$ MeV.

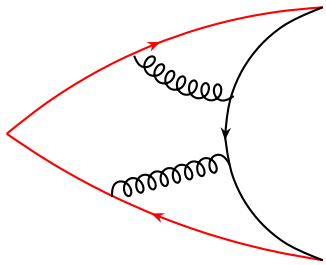

Figure 5.17: One possible first order graph responsible for mixing of charmonia with $D\overline{D}$ molecules. The red lines correspond to charm quarks, the black to light quarks, the twiddled ones to gluons.

Our standard procedure is applied in each channel: variational method with a set of optimized operators. The six dimensional operator basis contains three $c\bar{c}$ and three molecule fields, in each case differing by their spatial extent, labeled as local(l), narrow(n) and wide(w).
The generic form of our meson interpolators, centered around a position $x$, reads,

$$M(x) = (\bar{c}\Gamma_M c)_x \,, \tag{5.8}$$

while the molecular interpolators with separation $\mathbf{r}$ look like,

$$Y(x,\mathbf{r}) = \frac{1}{\sqrt{2}}\left((\bar{q}\Gamma_Y^1 c)_x(\bar{c}\Gamma_Y^2 q)_{x+\mathbf{r}} + (-)^s(\bar{c}\Gamma_Y^1 q)_x(\bar{q}\Gamma_Y^2 c)_{x+\mathbf{r}}\right) . \tag{5.9}$$

The explicit Gamma structures for the $J^{PC} = 0^{-+}, 1^{--}$ and $1^{++}$ channels are displayed in Tab. 5.4 (see also [103]).

In Fig. 5.18 we sketch the structure of the mixing matrix. The different smearing levels are again omitted for the sake of clarity. Solid lines represent charm quark propagators and wiggly lines light quark propagators. The prefactors are due to the two mass degenerate light sea quark flavors. The upper left corner contains the $c\bar{c}$, the lower right corner the molecular sector. The off-diagonal elements are responsible for explicit mixing.
For an explicit calculation of the diagrams appearing in Fig. 5.18, see App. A.4.

| $J^{PC}$ | $\Gamma_M$ | $\Gamma_Y^1$ | $\Gamma_Y^2$ | $s$ |
|---|---|---|---|---|
| $0^{-+}$ | $\gamma_5$ | $\gamma_i$ | $\gamma_i\gamma_5$ | 0 |
| $1^{--}$ | $\gamma_i$ | $\gamma_5$ | $\gamma_i\gamma_5$ | 1 |
| $1^{++}$ | $\gamma_i\gamma_5$ | $\gamma_5$ | $\gamma_i$ | 1 |

Table 5.4: Gamma structures of meson and molecule interpolating fields.

A similar matrix was constructed in [104] in order to investigate the $\rho$ meson decay width.

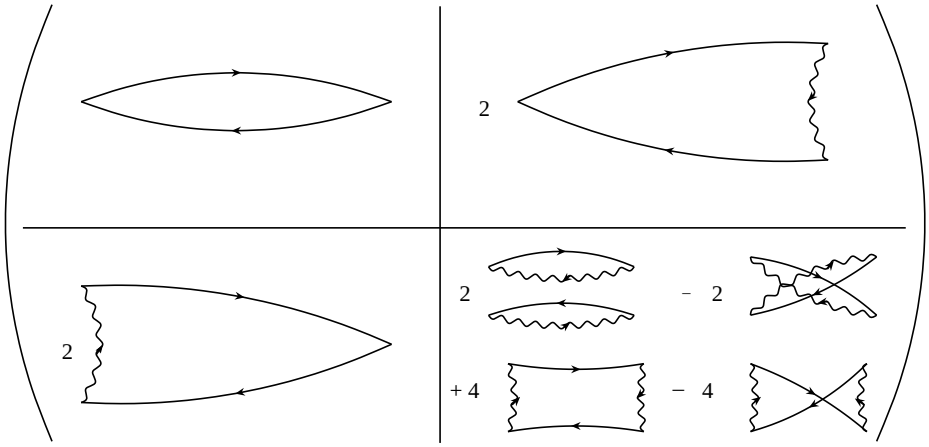


Figure 5.18: Cross correlator matrix for mixing of charmonia with $D\overline{D}$ molecules. Solid lines represent charm quarks, wiggled lines light quarks.

The spatial separation within the molecular operators was tuned by maximizing the magnitude of the off-diagonal element. The optimal value was $r = 4a \approx 0.3\,\text{fm}$. The charm-anticharm annihilation diagrams were omitted in this study due to the experience from the last section, where they turned out to be negligible.

For the evaluation of the last two diagrams of the molecular sector light all-to-all propagators are necessary. $O(100)$ complex $\mathbb{Z}_2$ stochastic estimates per configuration were calculated for this purpose, with the application of the noise reduction methods obdSSD and HPA. For the latter one the number of

allowed $\kappa D$ applications depends on the time separation $t$ of the correlator. Up to $t$ multiplications of $\kappa D$ can be applied in order to subtract noise, but leaving the signal unchanged.

Our strategy is the same as in the previous section, i.e. first diagonalizing the submatrices to obtain a reference spectrum which is then used to identify the eigenvectors of the full matrix.

An extra benefit of our analysis is the mass spectrum in the investigated channels. The separate diagonalization of the three by three submatrices provides us with at least four reliable eigenvalues, two for each subsector. However, since the molecular channels typically are rather noisy, we are only able to extract the ground states there, within reasonable errors. So we are left with three states in each $J^{PC}$ channel, plotted in Fig. 5.19. For the molecular masses we give two data points: the left ones are from the diagonalization procedure, the right ones represent the sums of the masses of the corresponding pairs of non-interacting $D$ mesons. Note that in the $1^{++}$ channel, the radially excited $\chi_{c1}$ is heavier than the molecular state, in contrast to the other channels. If we consider the fact that our pion is about 130-140 MeV too heavy, the mass of the molecular state is indeed consistent with the $X(3872)$, which most likely has $J^{PC} = 1^{++}$ [105]. In this sector the mass difference between the molecule and the two corresponding single mesons is the largest. For its jackknifed value we obtain $m(D^*\overline{D}_0) - m(D^*) - m(\overline{D}_0) = 88(26)$ MeV, which can be explained by a significant attraction between the $D$ mesons within the molecule. Equipped with the reference eigenvalues from the submatrices, we go for the diagonalization of the full six by six matrix. However, due to limited statistics, we find this to be numerically unstable and restrict ourselves to the sub-basis $M_{\text{local}}, M_{\text{narrow}}, Y_{\text{local}}, Y_{\text{narrow}}$. The normalization timeslice is $t_0 = 2$ for all channels.

We discuss the vector state as one example. In Fig. 5.20 we display the effective masses from the diagonalization of the two submatrices. The data points for $J/\Psi$ and its radial excitation are from the $c\bar{c}$ submatrix, the ones for the $D_1\overline{D}_0$ from the molecular sector.

The unmixed reference points can also be found in black color in Fig. 5.21. In addition, the two lowest lying effective masses from the diagonalization of the full matrix are shown there. We are able to identify these two states with $J/\Psi$ and $D_1\overline{D}_0$, respectively. Interestingly, the $\Psi'$ state is not found

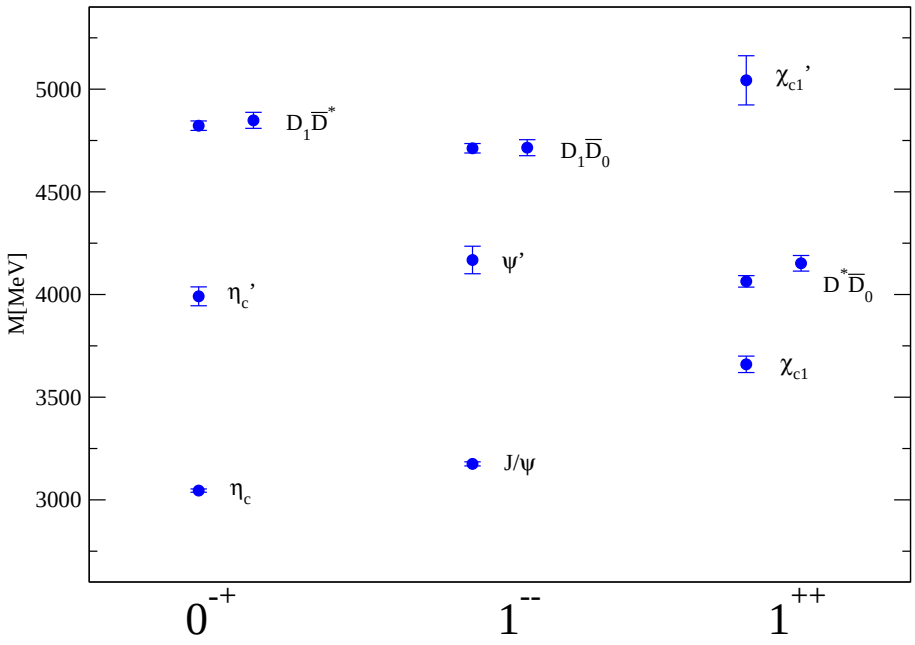


Figure 5.19: Mass spectra from the separate diagonalization of the submatrices within each sector.

in the diagonalization of the four by four system.
The corresponding eigenvector components are plotted in Fig. 5.22 for the $J/\psi$ and in Fig. 5.23 for the $D_1\overline{D}_0$ molecule. The $J/\Psi$ receives the dominant contribution from the local $c\bar{c}$ operator. However, the molecular configurations seem to contribute significantly, too. The $D_1\overline{D}_0$ state in contrast only contains small (but non-vanishing) $c\bar{c}$ admixtures. This is very similar to the observation in [64] that for $r < r_{SB}$ ($r_{SB}$ is the separation of the quarks, where the string breaks) the ground state of the static potential has a large tetraquark component, but the excited state has no two-quark admixture.
The effective masses and eigenvector components of the other channels are plotted in Figs. 5.24, 5.25, 5.26, 5.27, 5.28, 5.29, 5.30, 5.31 and 5.32.
In Tab. 5.5 we summarize the results for all channels that we investigated. In each of them we detect significant mixing effects between $c\bar{c}$ and four-quark states.

The large molecular contribution to the $\chi_{c1}$ is particularly noteworthy. Since this channel is especially interesting, primarily because of the $X(3872)$, we perform a further analysis appropriate to the needs of experimentalists. To this end, we define two states $|\tilde{\chi}_1\rangle$ and $|\tilde{\chi}_1'\rangle$, which correspond to the projections of $|\chi_1\rangle$ and $|\chi_1'\rangle$ onto the $c\bar{c}$ flavor subspace, respectively:

$$|\tilde{\chi}_1\rangle = \langle (c\bar{c})_l|\chi_1\rangle\,|(c\bar{c})_l\rangle + \langle (c\bar{c})_n|\chi_1\rangle\,|(c\bar{c})_n\rangle \quad (5.10)$$

$$|\tilde{\chi}_1'\rangle = \langle (c\bar{c})_l|\chi_1'\rangle\,|(c\bar{c})_l\rangle + \langle (c\bar{c})_n|\chi_1'\rangle\,|(c\bar{c})_n\rangle\ . \quad (5.11)$$

Note that we are able to extract the eigenvector components of $|\chi_1'\rangle$ since, in contrast to the other channels, its mass lies above the one of the molecule and is therefore not skipped.
The question of interest for experimentalists is to which extent the molecular state is built up from the following two projections:

$$\langle D\overline{D}^*|\tilde{\chi}_1\rangle = \langle (c\bar{c})_l|\chi_1\rangle\langle D\overline{D}^*|(c\bar{c})_l\rangle + \langle (c\bar{c})_n|\chi_1\rangle\langle D\overline{D}^*|(c\bar{c})_n\rangle \quad (5.12)$$

$$\langle D\overline{D}^*|\tilde{\chi}_1'\rangle = \langle (c\bar{c})_l|\chi_1'\rangle\langle D\overline{D}^*|(c\bar{c})_l\rangle + \langle (c\bar{c})_n|\chi_1'\rangle\langle D\overline{D}^*|(c\bar{c})_n\rangle \quad (5.13)$$

With the numbers from Tab. 5.5 we obtain $|\langle D\overline{D}^*|\tilde{\chi}_1\rangle| = 0.25(6)$ and $|\langle D\overline{D}^*|\tilde{\chi}_1'\rangle| = 0.44(7)$.

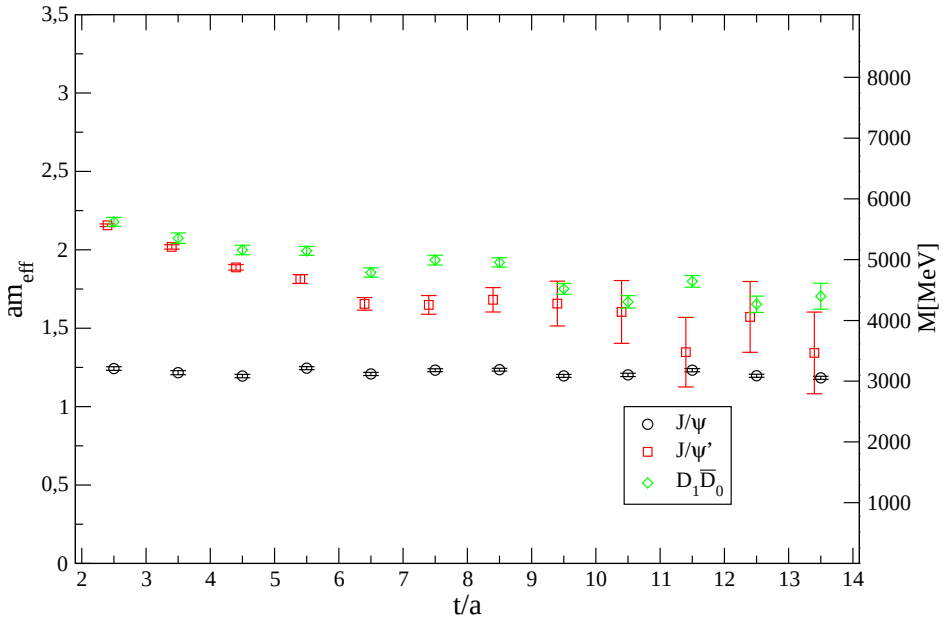


Figure 5.20: Effective masses of the eigenvalues of the submatrices in the $1^{--}$ channel.

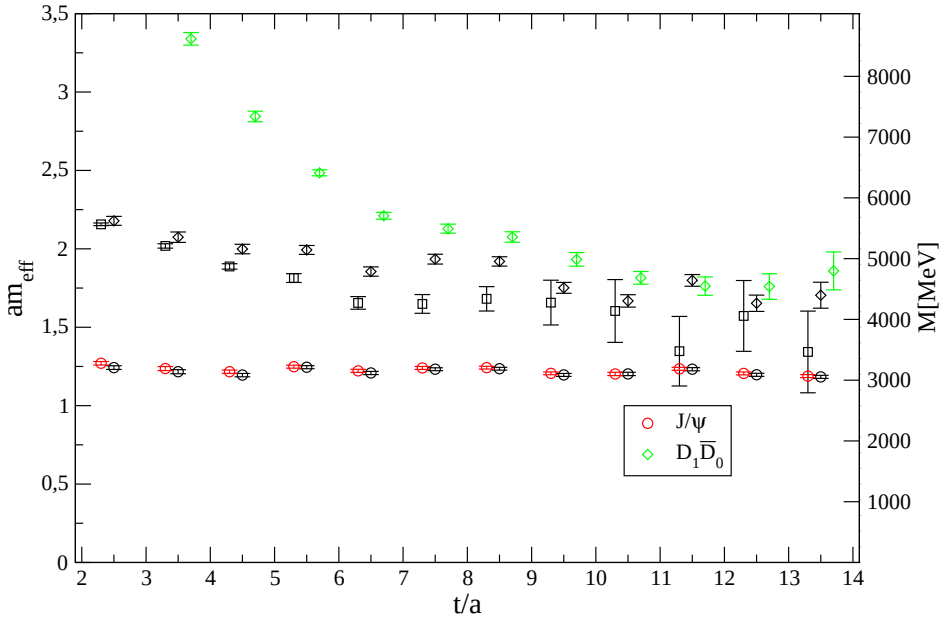


Figure 5.21: Effective masses of the eigenvalues of the full matrix in the $1^{--}$ channel. As a reference point the effective masses from the submatrices are plotted, too (black points).

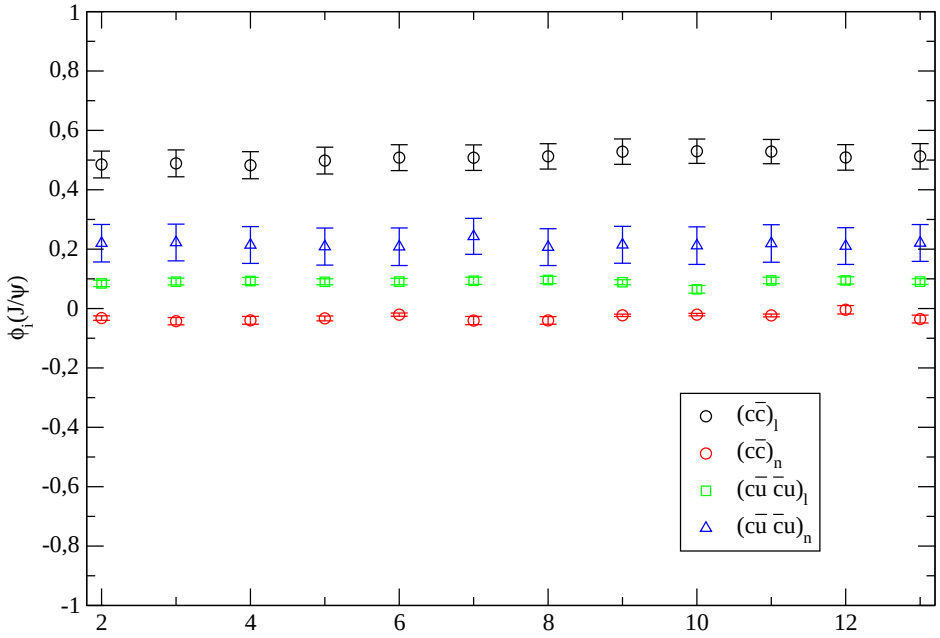


Figure 5.22: Eigenvector components of $J/\Psi$ in the full basis.

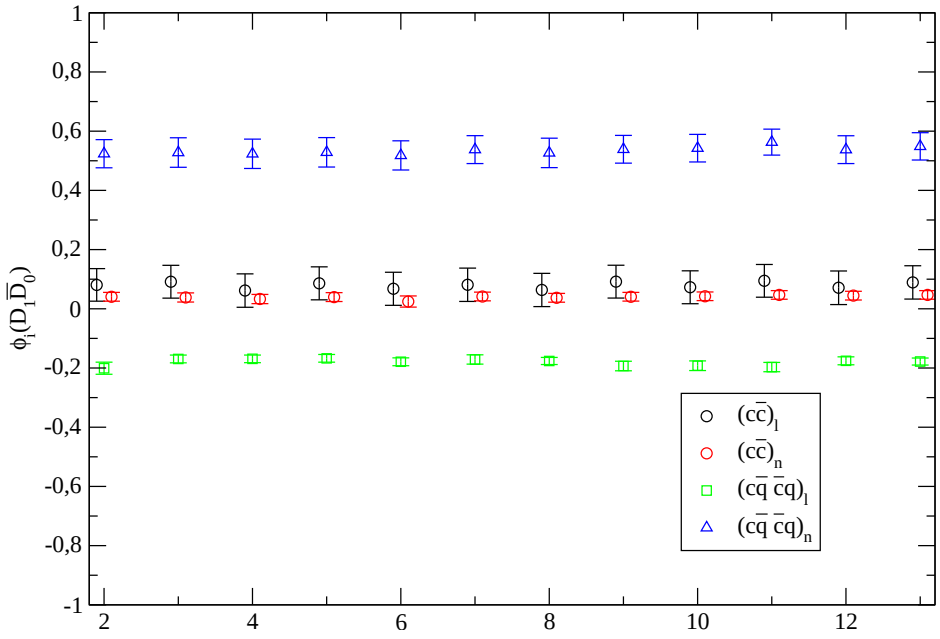


Figure 5.23: Eigenvector components of $D\overline{D}_1$ in the full basis.

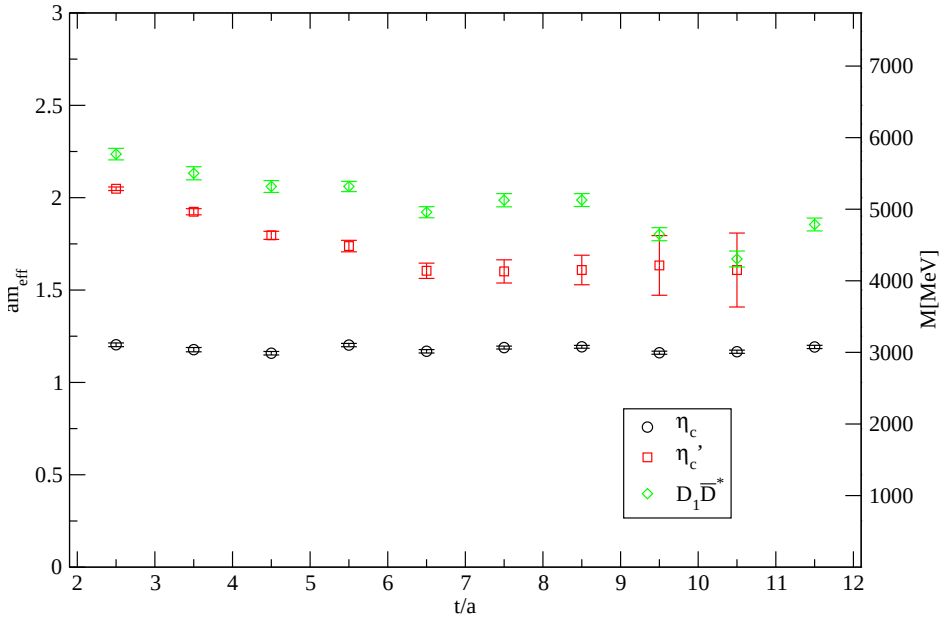


Figure 5.24: Effective masses of the eigenvalues of the submatrices in the $0^{-+}$ channel.

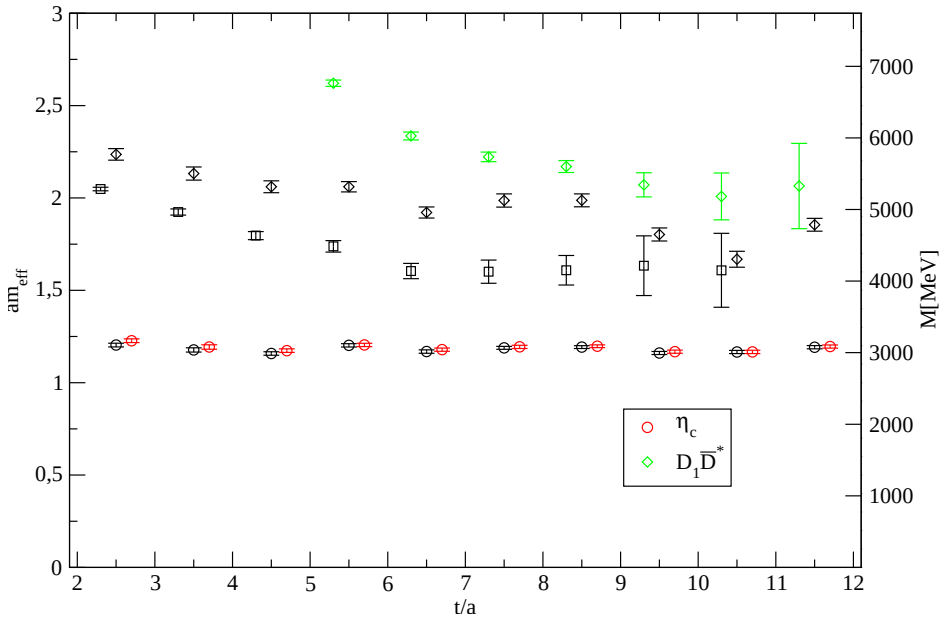


Figure 5.25: Effective masses of the eigenvalues of the full matrix in the $0^{-+}$ channel. As a reference point the effective masses from the submatrices are plotted, too (black points).

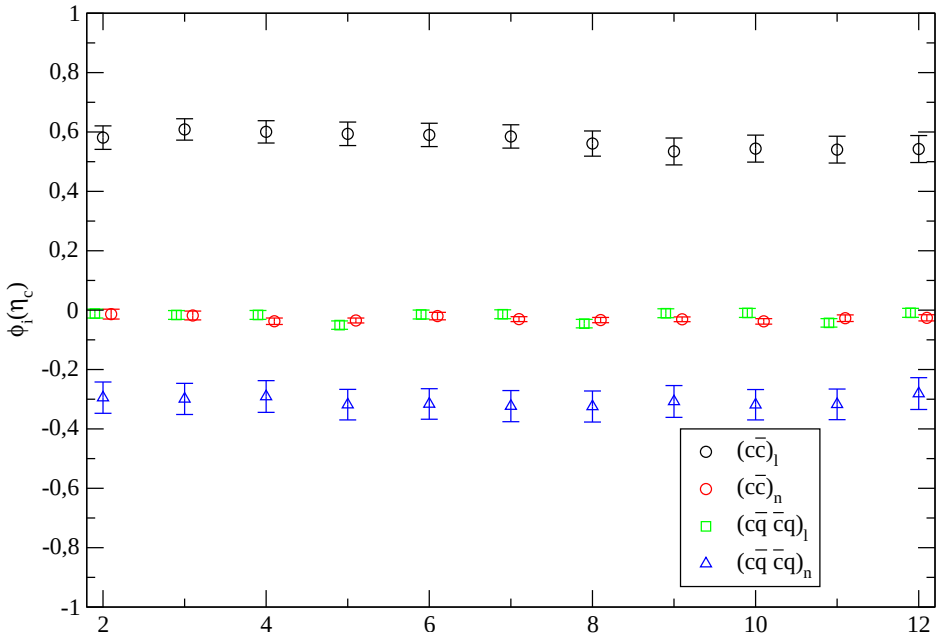


Figure 5.26: Eigenvector components of $\eta_c$ in the full basis.

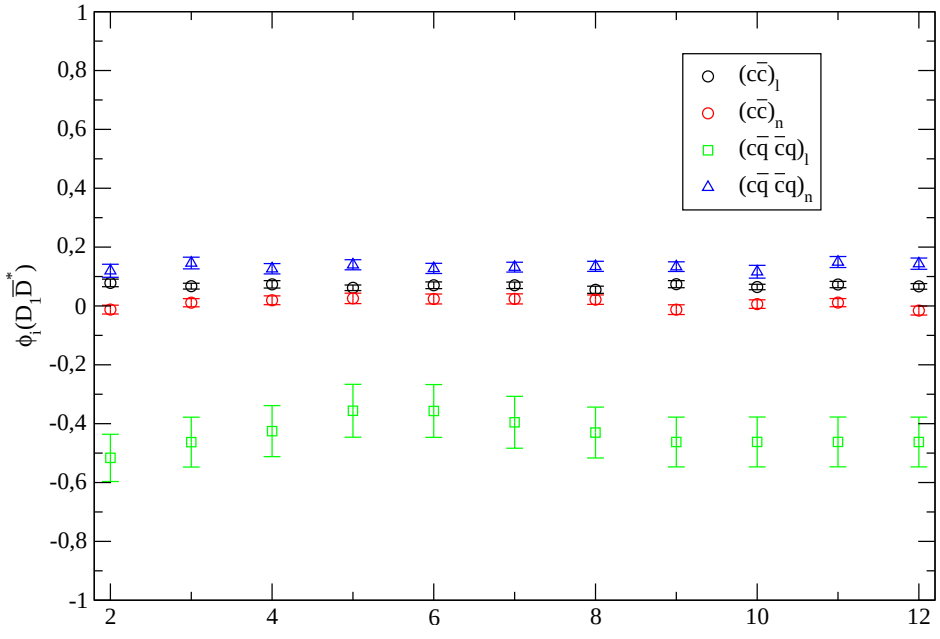


Figure 5.27: Eigenvector components of $D_1\overline{D}^*$ in the full basis.

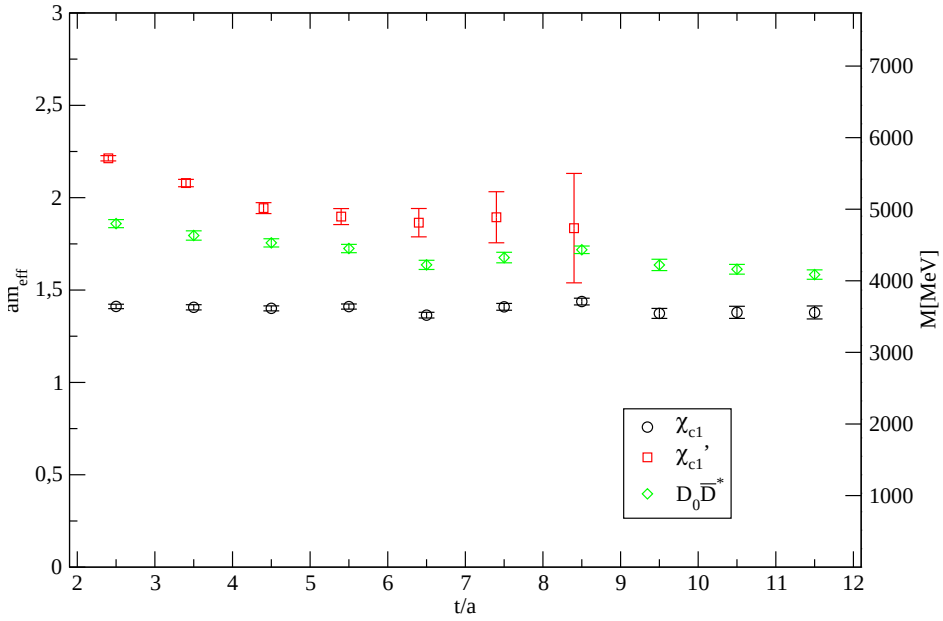


Figure 5.28: Effective masses of the eigenvalues of the submatrices in the $1^{++}$ channel.

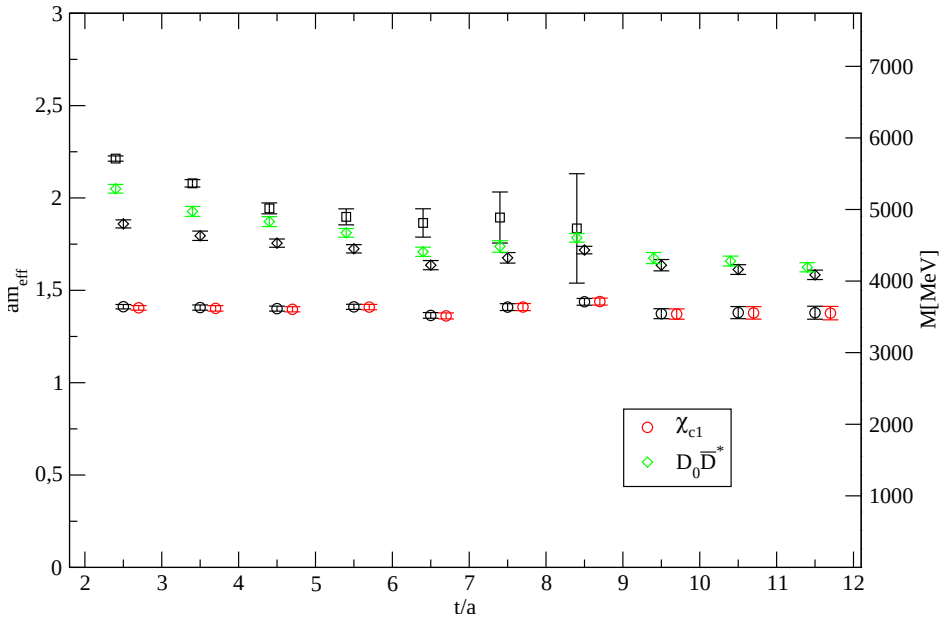


Figure 5.29: Effective masses of the eigenvalues of the full matrix in the $1^{++}$ channel. As a reference point the effective masses from the submatrices are plotted, too (black points).

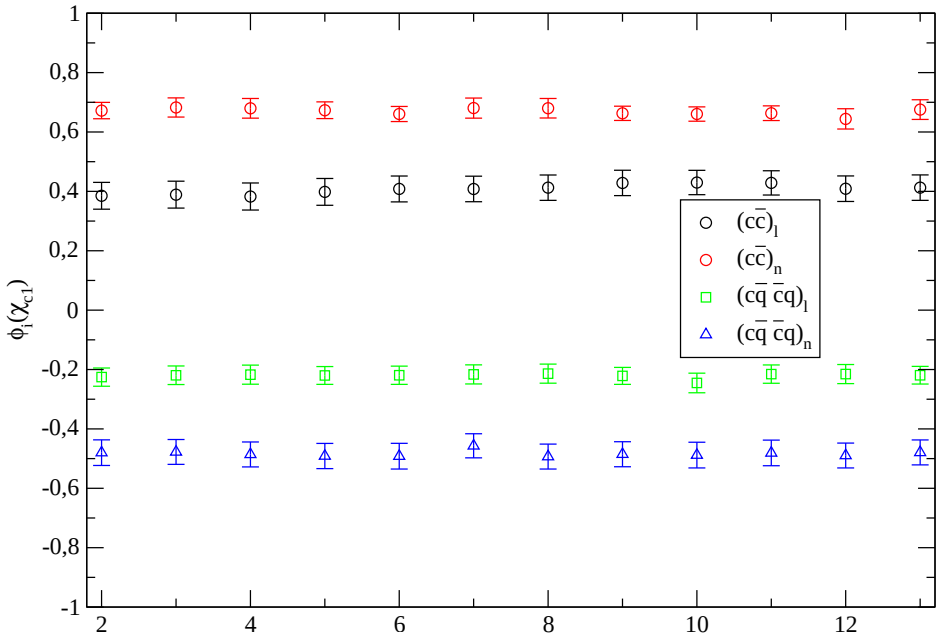


Figure 5.30: Eigenvector components of $\chi_{c1}$ in the full basis.

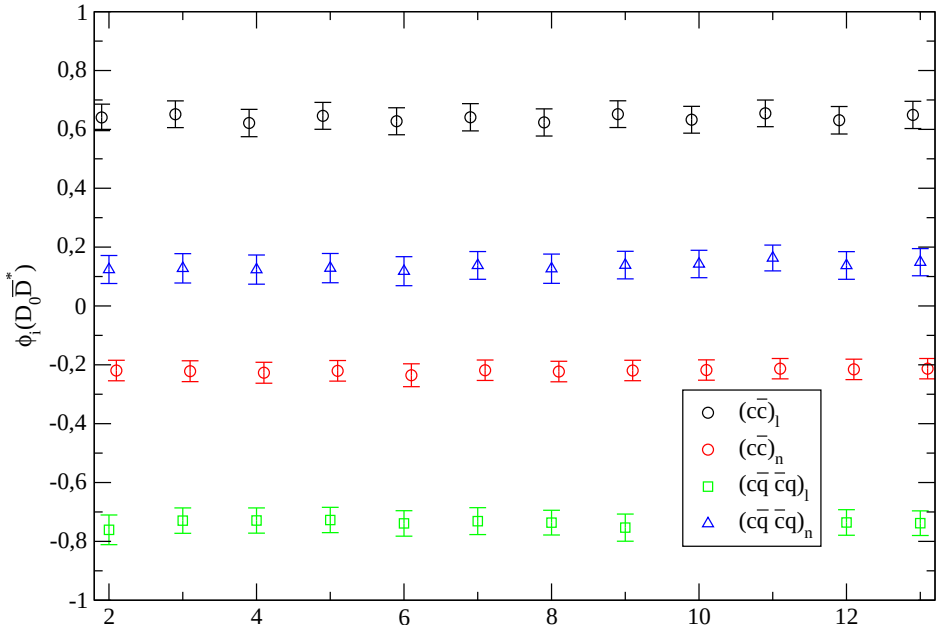


Figure 5.31: Eigenvector components of $D\overline{D}^*$ in the full basis.

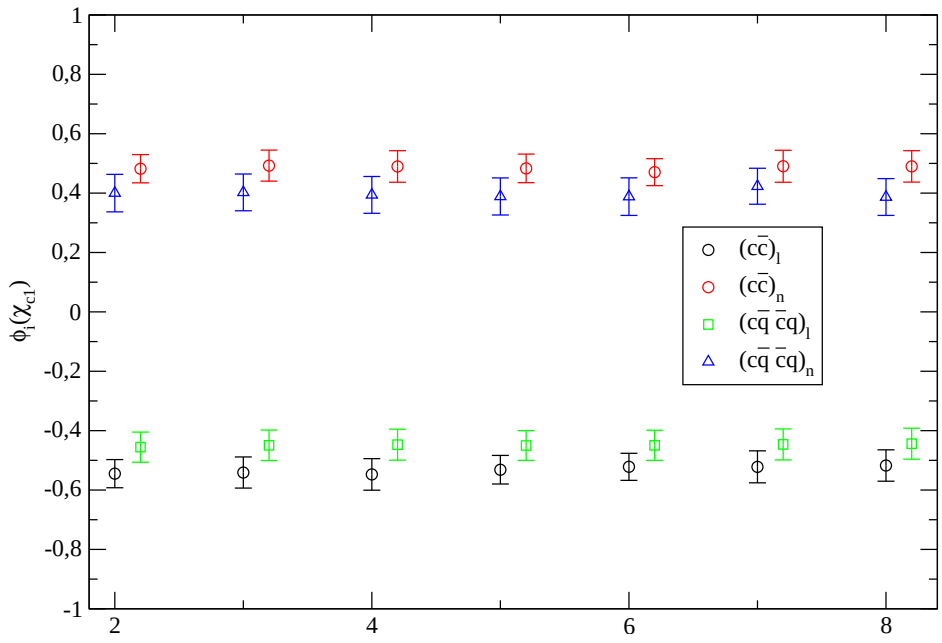


Figure 5.32: Eigenvector components of $\chi'_{c1}$ in the full basis.

| | $(c\bar{c})_l$ | $(c\bar{c})_n$ | $(c\bar{q}\bar{c}q)_l$ | $(c\bar{q}\bar{c}q)_n$ |
|---|---|---|---|---|
| $\eta_c$ | 0.54(3) | -0.02(1) | -0.1(1) | -0.31(5) |
| $D_1\overline{D}^*$ | 0.07(1) | 0.01(1) | -0.46(8) | 0.14(2) |
| $J/\psi$ | 0.51(4) | -0.03(1) | 0.09(1) | 0.21(6) |
| $D_1\overline{D}$ | 0.08(6) | 0.04(1) | -0.18(1) | 0.53(4) |
| $\chi_{c1}$ | 0.39(4) | 0.69(3) | -0.22(3) | -0.49(4) |
| $D\overline{D}^*$ | 0.63(4) | -0.23(3) | -0.73(4) | 0.12(3) |
| $\chi'_{c1}$ | -0.52(6) | 0.50(5) | -0.46(5) | 0.39(6) |

Table 5.5: Eigenvector components in the full basis.

*Science cannot solve the ultimate mystery of nature. And that is because, in the last analysis, we ourselves are a part of the mystery that we are trying to solve.* – *Unsourced*

Max Planck

# 6 Conclusion & Outlook

We started out with an overview of the experimental status of the charmonium sector. Research facilities and their experiments were briefly addressed in order to motivate the undertaking of this work.
The quarks composing charmonia are predominantly governed by the strong interaction, whose theoretical description QCD was discussed in chapter two. Subsequently, we formulated the implementation of QCD on finite lattices and saw what complications arise and how to cope with them.
In the fourth chapter we introduced the tools necessary to perform and analyze our lattice QCD calculations. The focus lay on the variational method as the basic instrument to investigate masses and couplings of both ground and excited states reliably. A careful optimization of the operator basis is crucial in this context.
Indispensable for most of the quantities is the sophisticated estimation of all-to-all propagators. Established techniques like standard dilution or HPA were discussed, but also new approaches like SSD, RNS and TSM have been introduced.
Finally these tools were put in action in order to yield information on the spectrum and composition of charmonia.
The calculated spectrum fits the experimental data fairly well, except for the 1S and 1P hyperfine splittings. The possible reasons for this shortcoming have been discussed in detail. The small mass gap between the two lowest lying states in the exotic channels is also remarkable, suggesting a primarily hybrid constitution. A continuum extrapolation would be worthwhile, but is unfortunately not feasible with the available lattices.
By reconstructing the spatial wavefunctions of the pseudoscalar state from the eigenvectors of the corresponding cross correlator matrix, we were able

to resolve the node structure of the three lowest lying states in agreement with the 1S, 2S and 3S assignments.
Our attention then turned to several mixing studies. First, mixing between S- and D-waves in the vector channel was explored, confirming the PDG assignment of the three lowest lying states.
Motivated by the underestimation of the hyperfine splitting, the mixing of $\eta_c$ and $\eta'$ was addressed in detail by diagonalizing a cross correlator matrix containing both charm and light quark interpolating fields. The outcome was negative, we saw no significant mixing effect between the two states. We can set an upper limit on the $\eta_c$ mass shift of 11 MeV. A potential uncertainty in this analysis was the quite high pion mass of about 1 GeV. Since the dependence of the mixing magnitude on the light quark mass is *a priori* not predictable, runs on configurations with lighter pions are desired.
In the last section we applied a variational method with an operator basis including both conventional meson and charm-light molecule interpolators in three channels, $0^{-+}$, $1^{--}$ and $1^{++}$, on a lattice with significant lower pion mass. The mixing between the different Fock states through creation/annihilation of a light quark-antiquark pair turned out to be large for all quantum numbers under consideration. Especially for $1^{++}$, where we furthermore detected attraction between the two mesons in the molecule. For this channel an additional operator representing a molecule in a relative P-wave would be of great interest, since this is the supposably dominant constituent of the famous, but still cryptic $X(3872)$.
In general, larger lattice volumes, lighter sea quark masses and the possibility to perform a continuum extrapolation are desired for future studies.
Although the precise values of the eigenvector components should not be taken too seriously, since the operator basis is rather small and thus may miss non-negligible parts of the physical wavefunction, our analysis clearly substantiates the assumption of charmonium states having a rich Fock structure.
Our analysis shows the striking ability of the variational method to disclose the inner structure of not only charmonium, but in principle all hadronic states, when an elaborate set of interpolating fields is used.

*Machines take me by surprise with great frequency.* – *Computing Machinery and Intelligence.*

Alan Turing

# A

# Numerical Simulation Details

## A.1 Gauge Configurations

All simulations are performed on gauge configurations provided by the QCDSF collaboration [106].
Based on the Clover formulation the two light flavors have been included as sea quarks. Gauge degrees of freedom are represented by the Wilson plaquette action. The lattice spacing was determined from the value $r_0 \approx 0.46$ fm such that the nucleon reaches its experimental mass when extrapolated to physical $m_\pi$.
Tab. A.1 gives the details of the used lattices together with an identifier which we refer to in this thesis.

| ID | $\beta$ | $\kappa$ | volume | $m_\pi$[GeV] | $a$[fm] | $L$[fm] | $\kappa_c$ | $N_{\text{conf}}$ |
|---|---|---|---|---|---|---|---|---|
| ① | 5.20 | 0.13420 | $16^3 \times 32$ | 1.007(2) | 0.1145 | 1.83 | 0.1163 | 100 |
| ② | 5.29 | 0.13620 | $24^3 \times 48$ | 0.400(1) | 0.0770 | 1.84 | 0.1245 | 130 |
| ③ | 5.29 | 0.13632 | $24^3 \times 48$ | 0.280(1) | 0.0767 | 1.84 | 0.1244 | 100 |

Table A.1: Details of the lattices in use, together with an identifying ID.

The configurations have been downloaded from the *International Lattice Data Grid (ILDG)*, an international database to share lattice QCD data files with defined standards among research groups around the world [107, 108].

## A.2 The Chroma Software Suite

The lattice community is growing both larger and closer together. In spite of the competitive incentive among the different groups, it was inevitable

that a common software foundation was developed sooner or later. The broadness of common ground is just too significant that rewriting code (often in different programming languages) over and over again does not make sense. A joint effort would furthermore increase the reproduceability and credibility of results.
There is no certified standard yet, several candidates are on the market, of which some seem to be more favorable than others.
We rely on the LQCD software suite *Chroma* [109, 110] written in C++. Its main contributers are Balint Joó and Robert G. Edwards, however, today a significant part of the code is written by users all over the world.
Chroma is designed completely object orientated in order to provide maximal reusability and clear distinction between the different building blocks of programming logic. State of the art programming techniques, realized through the use of design patterns inspired by Andrei Alexandrescu's book "Modern C++ Design" [111], elevate Chroma to the archetype of LQCD software.
Even scientists without any programming knowledge can run Chroma as a black box device, rendered possible by the usage of straightforwardly structured input files.
To compensate for any overhead induced by the class structure its developers implemented PETE, a generic programming library based on expression templates. This generates a performance comparable to Fortran code for matrix-vector multiplication, for instance.
In this work we partly used already existing chroma routines, for example to generate the numbers for the spectra. The majority of our results are however obtained by running self-written code, which either used Chroma as a library to link to, or the whole code was included in the Chroma source tree. Amongst others, we integrated Wuppertal smearing or the possibility to use modified wavefunctions as sources.
To summarize, Chroma provides an open, reliable, flexible and fast LQCD software library, which gradually gains more and more devotees.

## A.3 Used Machines/Architectures

Our runs were performed on three different machines: on the *QCDOC* machine in Regensburg [112], on the Blue Gene/P system *JUGENE* located at

Forschungszentrum Jülich [113] and on the high performance cluster *Athene* at the Rechenzentrum of the University of Regensburg [114].
The QCDOC is a special purpose machine designed to fit the requirements of Lattice QCD simulations through a highly scalable and massively parallel implementation. The nodes are based on 64 bit PowerPC RISC processors with a peak speed of 1 GFlop/s and interconnected in a 6-dimension mesh with the topology of a torus. Fortunately, Chroma comes with an optimized module for the QCDOC to take full advantage of its capacities [115].
The by far most powerful system we simulated on is the JUGENE at Forschungszentrum Jülich, which is actually based on the QCDOC architecture. With a peak performance of 825,5 TFlops/s[1] this BlueGene/P machine ranks at third place of the fastest supercomputers [116] and is the best performing machine used for civil purposes worldwide. The 294.912 PowerPC nodes including 144 terrabyte memory are housed in 72 racks, see Fig. A.1. Another notable advantage of the Jugene is its extremely low power consumption compared to other systems. *Green IT* becomes more and more an issue among today's computer architects.
Another large portion of our computational load was processed at the DELL cluster Athene at the local Rechenzentrum, put into operation as recently as spring 2009. The 187 computing nodes are each equipped with two AMD Opteron Barcelona Quad Core processors, 16 GB local memory and both Ethernet and InfiniBand interfaces. Two external fileservers provide a disk space capacity of 64 TB.

[1] After its upgrade in May 2009.


Figure A.1: Picture of the updated Jugene installation at Forschungszentrum Jülich.

## A.4 Evaluation of Mixing-Matrix Diagrams

Consider Fig. 5.18 (For convenience we omit prefactors and work in Minkowski space.)
The upper left corner, corresponding to the meson sector, is given by

$$\begin{aligned}
\langle M(x)\overline{M}(y)\rangle &= \langle(\bar{c}\Gamma_M c)_x(\bar{c}\Gamma_M c)_y\rangle \\
&= \left\langle (\overline{c}\Gamma_M c)_x(\overline{c}\Gamma_M c)_y \right\rangle - \left\langle (\overline{c}\Gamma_M c)_x\,(\overline{c}\Gamma_M c)_y \right\rangle \\
&= \mathrm{Tr}\left(D_c^{-1}(x,y)\Gamma_M D_c^{-1}(y,x)\right) - \mathrm{Tr}\left(D_c^{-1}(x,x)\Gamma_M\right)\mathrm{Tr}\left(D_c^{-1}(y,y)\Gamma_M\right) \\
&\approx \mathrm{Tr}\left(D_c^{-1}(x,y)\Gamma_M D_c^{-1}(y,x)\right)\ .
\end{aligned}$$

In the third line the Wick contractions have been performed. The diagram with charm quark-antiquark annihilation has been neglected in the last step.
The upper right corner responsible for explicit mixing is given by

$$\begin{aligned}
\langle M(x)\overline{Y}(y,r)\rangle &= \left\langle(\bar{c}\Gamma_M c)_x\left((\bar{c}\Gamma_Y^1 q)_y(\bar{q}\Gamma_Y^2 c)_{y+r} + (\bar{c}\Gamma_M c)_x(\bar{q}\Gamma_Y^1 c)_y(\bar{c}\Gamma_Y^2 q)_{y+r}\right)\right\rangle \\
&= \left\langle(\bar{c}\Gamma_M c)_x(\bar{c}\Gamma_Y^1 q)_y(\bar{q}\Gamma_Y^2 c)_{y+r}\right\rangle + \left\langle(\bar{c}\Gamma_M c)_x(\bar{q}\Gamma_Y^1 c)_y(\bar{c}\Gamma_Y^2 q)_{y+r}\right\rangle \\
&= \left\langle (\overline{c}\Gamma_M c)_x\,(\overline{c}\Gamma_Y^1 q)_y(\overline{q}\Gamma_Y^2 c)_{y+r} \right\rangle + \left\langle (\overline{c}\Gamma_M c)_x(\overline{c}\Gamma_Y^1 q)_y(\overline{q}\Gamma_Y^2 c)_{y+r} \right\rangle \\
&+ \left\langle (\overline{c}\Gamma_M c)_x\,(\overline{q}\Gamma_Y^1 c)_y(\overline{c}\Gamma_Y^2 q)_{y+r} \right\rangle + \left\langle (\overline{c}\Gamma_M c)_x(\overline{q}\Gamma_Y^1 c)_y(\overline{c}\Gamma_Y^2 q)_{y+r} \right\rangle \\
&= \mathrm{Tr}\left(D_c^{-1}(x,x)\Gamma_M\right)\mathrm{Tr}\left(D_c^{-1}(y,y+r)\Gamma_Y^2 D_q^{-1}(y+r,y)\Gamma_Y^1\right) \\
&+ \mathrm{Tr}\left(D_c^{-1}(x,y+r)\Gamma_Y^2 D_q^{-1}(y+r,y)\Gamma_Y^1 D_c^{-1}(y,x)\Gamma_M\right) \\
&+ \mathrm{Tr}\left(D_c^{-1}(x,x)\Gamma_M\right)\mathrm{Tr}\left((D_c^{-1}(y+r,y)\Gamma_Y^1 D_q^{-1}(y,y+r)\Gamma_Y^2\right) \\
&+ \mathrm{Tr}\left(D_c^{-1}(x,y)\Gamma_Y^1 D_q^{-1}(y,y+r)\Gamma_Y^2 D_c^{-1}(y+r,x)\Gamma_M\right) \\
&\approx \mathrm{Tr}\left(D_c^{-1}(x,y+r)\Gamma_Y^2 D_q^{-1}(y+r,y)\Gamma_Y^1 D_c^{-1}(y,x)\Gamma_M\right) \\
&+ \mathrm{Tr}\left(D_c^{-1}(x,y)\Gamma_Y^1 D_q^{-1}(y,y+r)\Gamma_Y^2 D_c^{-1}(y+r,x)\Gamma_M\right)\ .
\end{aligned}$$

Again, in the last step diagrams containing charm quark-antiquark annihilation loops have been neglected. The remaining two terms only differ by their orientation, which is a consequence of the molecule operator being a charge conjugation eigenstate.

The lower right corner, corresponding to the molecule sector, is given by

$$
\begin{aligned}
\langle Y(x,r)\overline{Y}(y,r)\rangle &= \left\langle \left((\bar{q}\Gamma_Y^1 c)_x(\bar{c}\Gamma_Y^2 q)_{x+r} + (\bar{c}\Gamma_Y^1 q)_x(\bar{q}\Gamma_Y^2 c)_{x+r}\right)\left((\bar{c}\Gamma_Y^1 q)_y(\bar{q}\Gamma_Y^2 c)_{y+r} + (\bar{q}\Gamma_Y^1 c)_y(\bar{c}\Gamma_Y^2 q)_{y+r}\right)\right\rangle \\
&= \left\langle (\bar{q}\Gamma_Y^1 c)_x(\bar{c}\Gamma_Y^2 q)_{x+r}(\bar{c}\Gamma_Y^1 q)_y(\bar{q}\Gamma_Y^2 c)_{y+r}\right\rangle + \left\langle (\bar{q}\Gamma_Y^1 c)_x(\bar{c}\Gamma_Y^2 q)_{x+r}(\bar{q}\Gamma_Y^1 c)_y(\bar{c}\Gamma_Y^2 q)_{y+r}\right\rangle \\
&+ \left\langle (\bar{c}\Gamma_Y^1 q)_x(\bar{q}\Gamma_Y^2 c)_{x+r}(\bar{c}\Gamma_Y^1 q)_y(\bar{q}\Gamma_Y^2 c)_{y+r}\right\rangle + \left\langle (\bar{c}\Gamma_Y^1 q)_x(\bar{q}\Gamma_Y^2 c)_{x+r}(\bar{q}\Gamma_Y^1 c)_y(\bar{c}\Gamma_Y^2 q)_{y+r}\right\rangle \\
&= \left\langle \overline{(\bar{q}\Gamma_Y^1 c)_x(\bar{c}\Gamma_Y^2 q)_{x+r}}\ \overline{(\bar{c}\Gamma_Y^1 q)_y(\bar{q}\Gamma_Y^2 c)_{y+r}}\right\rangle + \left\langle \overline{(\bar{q}\Gamma_Y^1 c)_x(\bar{c}\Gamma_Y^2 q)_{x+r}(\bar{c}\Gamma_Y^1 q)_y(\bar{q}\Gamma_Y^2 c)_{y+r}}\right\rangle \\
&+ \left\langle \overline{(\bar{q}\Gamma_Y^1 c)_x(\bar{c}\Gamma_Y^2 q)_{x+r}(\bar{c}\Gamma_Y^1 q)_y(\bar{q}\Gamma_Y^2 c)_{y+r}}\right\rangle + \left\langle \overline{(\bar{q}\Gamma_Y^1 c)_x(\bar{c}\Gamma_Y^2 q)_{x+r}(\bar{c}\Gamma_Y^1 q)_y(\bar{q}\Gamma_Y^2 c)_{y+r}}\right\rangle \\
&+ \ldots \\
&= \mathrm{Tr}\left(D_q^{-1}(x,x+r)\Gamma_Y^2 D_c^{-1}(x+r,x)\Gamma_Y^1\right)\mathrm{Tr}\left(D_c^{-1}(y,y+r)\Gamma_Y^2 D_q^{-1}(y+r,y)\Gamma_Y^1\right) \\
&+ \mathrm{Tr}\left(D_q^{-1}(x,y)\Gamma_Y^1 D_c^{-1}(y,y+r)\Gamma_Y^2 D_q^{-1}(y+r,y+r)\Gamma_Y^2 D_c^{-1}(x+r,x)\Gamma_Y^1\right) \\
&+ \mathrm{Tr}\left(D_q^{-1}(x,y)\Gamma_Y^1 D_c^{-1}(y,x)\right)\mathrm{Tr}\left(\Gamma_Y^2 D_c^{-1}(x+r,y+r)\Gamma_Y^2 D_q^{-1}(y+r,x+r)\Gamma_Y^2\right) \\
&+ \mathrm{Tr}\left(D_q^{-1}(x,x+r)\Gamma_Y^2 D_c^{-1}(x+r,y+r)\Gamma_Y^2 D_q^{-1}(y+r,y)\Gamma_Y^1 D_c^{-1}(y,x)\Gamma_Y^1\right) + \ldots \\
&\approx \mathrm{Tr}\left(D_q^{-1}(x,y)\Gamma_Y^1 D_c^{-1}(y,x)\right)\mathrm{Tr}\left(\Gamma_Y^2 D_c^{-1}(x+r,y+r)\Gamma_Y^2 D_q^{-1}(y+r,x+r)\Gamma_Y^2\right) \\
&+ \mathrm{Tr}\left(D_q^{-1}(x,x+r)\Gamma_Y^2 D_c^{-1}(x+r,y+r)\Gamma_Y^2 D_q^{-1}(y+r,y)\Gamma_Y^1 D_c^{-1}(y,x)\Gamma_Y^1\right) + \ldots
\end{aligned}
$$

Again, diagrams where charm quarks are created and annihilated at the same timeslice are neglected in the last step. The remaining two terms correspond to the first and third diagram of the lower right corner of Fig. 5.18, respectively.

Note that only the Wick contractions of the first term in the first line are shown explicitly. The contractions of the other terms lead to the same diagrams but with different orientation and to the corresponding crossed ones (contributing with negative sign).

# B

# Notations and Conventions

Throughout this thesis we work in natural units; i. e., we set $\hbar = c = 1$.

## B.1 Euclidean Space

Throughout this thesis we work in Euclidean space; that is, we are using an imaginary time variable. Mathematically this just represents a substitution:

$$t \to it. \tag{B.1}$$

The proper time is then given by $ds^2 = dt^2 + dx^2 + dy^2 + dz^2$; time and space are treated on the same footing. Therefore the metric tensor is diagonal, $g_{\mu\nu} = \delta_{\mu\nu}$. So we do not have to distinguish between upper and lower Lorentz indices, in other words we do not make a difference between co- and contravariant objects.
The purpose of this substitution is that the path integral then becomes accessible to Monte Carlo methods. The exponential function is not oscillating any more, but acts as an exponential suppression, which favors configurations with a minimal value for the action.

## B.2 Conventions for the $\gamma$-Matrices

Throughout the whole thesis we use the chiral representation of Euclidean $\gamma$-matrices:

$$\gamma_1 = \begin{pmatrix} 0 & 0 & 0 & \mathrm{i} \\ 0 & 0 & \mathrm{i} & 0 \\ 0 & -\mathrm{i} & 0 & 0 \\ -\mathrm{i} & 0 & 0 & 0 \end{pmatrix} \qquad \gamma_2 = \begin{pmatrix} 0 & 0 & 0 & 1 \\ 0 & 0 & -1 & 0 \\ 0 & -1 & 0 & 0 \\ 1 & 0 & 0 & 0 \end{pmatrix}$$

$$\gamma_3 = \begin{pmatrix} 0 & 0 & \mathrm{i} & 0 \\ 0 & 0 & 0 & -\mathrm{i} \\ -\mathrm{i} & 0 & 0 & 0 \\ 0 & \mathrm{i} & 0 & 0 \end{pmatrix} \qquad \gamma_4 = \begin{pmatrix} 0 & 0 & 1 & 0 \\ 0 & 0 & 0 & 1 \\ 1 & 0 & 0 & 0 \\ 0 & 1 & 0 & 0 \end{pmatrix} \quad \text{B.2}$$

$$\gamma_5 = \gamma_1\gamma_2\gamma_3\gamma_4 = \begin{pmatrix} 1 & 0 & 0 & 0 \\ 0 & 1 & 0 & 0 \\ 0 & 0 & -1 & 0 \\ 0 & 0 & 0 & -1 \end{pmatrix}. \quad \text{B.3}$$

## B.3 The SU(3) Group

Mathematical groups are perfectly suited for describing symmetries.
In the case of QCD the symmetry is the invariance of the Lagrangian under local color rotations. These transformations are elements of the *SU(3) color group*. It represents a Lie group, whose elements are unitary and have a determinant of plus one.
The elements $\Lambda$ can be written in terms of the *generators* of the group $t^a$:

$$\Lambda = e^{i\omega^a t^a}, \quad \text{B.4}$$

where $\vec{\omega}$ is the parameter vector.
The number of generators in a SU(N) group equals $N^2 - 1$. So for $N = 3$ we obtain 8.
The generators obey the su(3) algebra:

$$[t^a, t^b] = i f^{abc} t^c. \quad \text{B.5}$$

The $f^{abc}$ are called *structure constants*. Furthermore (due to the properties of the group elements):

$$\mathrm{Tr}[t^a] = 0 \qquad \text{(traceless)}, \quad \text{B.6}$$

$$(t^a)^\dagger = t^a \qquad \text{(hermitian)}, \quad \text{B.7}$$

$$\mathrm{Tr}[t^a t^b] \;=\; \frac{1}{2}\delta^{ab} \quad \text{(normalized)}. \tag{B.8}$$

In the fundamental representation, the *Gell-Mann* matrices are commonly used as explicit representations for the generators:

$$t^a \;=\; \frac{\lambda^a}{2}, \qquad a = 1, 2, \ldots, 8. \tag{B.9}$$

They are given by

$$\lambda^1 = \begin{pmatrix} 0 & 1 & 0 \\ 1 & 0 & 0 \\ 0 & 0 & 0 \end{pmatrix}, \quad \lambda^2 = \begin{pmatrix} 0 & -\mathrm{i} & 0 \\ \mathrm{i} & 0 & 0 \\ 0 & 0 & 0 \end{pmatrix},$$

$$\lambda^3 = \begin{pmatrix} 1 & 0 & 0 \\ 0 & -1 & 0 \\ 0 & 0 & 0 \end{pmatrix}, \quad \lambda^4 = \begin{pmatrix} 0 & 0 & 1 \\ 0 & 0 & 0 \\ 1 & 0 & 0 \end{pmatrix},$$

$$\lambda^5 = \begin{pmatrix} 0 & 0 & -\mathrm{i} \\ 0 & 0 & 0 \\ \mathrm{i} & 0 & 0 \end{pmatrix}, \quad \lambda^6 = \begin{pmatrix} 0 & 0 & 0 \\ 0 & 0 & 1 \\ 0 & 1 & 0 \end{pmatrix},$$

$$\lambda^7 = \begin{pmatrix} 0 & 0 & 0 \\ 0 & 0 & -\mathrm{i} \\ 0 & \mathrm{i} & 0 \end{pmatrix}, \quad \lambda^8 = \begin{pmatrix} \frac{1}{\sqrt{3}} & 0 & 0 \\ 0 & \frac{1}{\sqrt{3}} & 0 \\ 0 & 0 & \frac{-2}{\sqrt{3}} \end{pmatrix}. \tag{B.10}$$

In the adjoint representation the generators are represented by the structure constants.

# C

# Statistical Analysis

## C.1 Statistical Errors

To be able to draw conclusions from our calculations we have to estimate the statistical errors of our results. A nice introduction for dealing with statistical errors and fitting techniques can be found in [117].
Assuming we performed $N$ measurements on a quantity $y$, we obtain a data set $(y_1, y_2, ..., y_N)$. The *sample mean value* of the quantities $y_i$ is then given by

$$\overline{y} = \frac{1}{N}\sum_{i=1}^{N} y_i \tag{C.1}$$

and the *variance* by

$$\sigma^2 = \frac{1}{N-1}\sum_{i=1}^{N}(\overline{y} - y_i)^2 \tag{C.2}$$

The *standard deviation* is given by

$$s = \sqrt{\frac{\sigma^2}{N}[1 + O(\frac{1}{N})]} \tag{C.3}$$

So for large enough $N$ we obtain for the mean value

$$\langle y \rangle = \overline{y} \pm \frac{\sigma}{\sqrt{N}} \tag{C.4}$$

This implies that if we want to halve our error, we have to quadruple our statistics.

## C.2 Fitting Techniques

In the cases where we not only measure a single quantity but $L$ different quantities, we obtain a data set

$$(x_i, \overline{y}_i \pm \sigma_i), \qquad i = 1, \ldots, L \tag{C.5}$$

For instance, $x_i$ could label the timeslice and $\overline{y}_i$ the corresponding correlator at that timeslice.
Given this set we want to determine so-called secondary observables, e.g. masses or amplitudes. To do so we have to fit a trial function $f(x_i, \mathbf{a}) = f(x_i, a_1, ..., a_n)$ to our data points with parameters $a_j$ to be determined.
Assuming Gaussian errors, we use the method of *least-squares fitting*.
The starting point is the $\chi^2$-functional:

$$\chi^2(\mathbf{a}) = \sum_{i,j=1}^{L} [\overline{y}_i - f(x_i, \mathbf{a})] V_{ij}^{-1} [\overline{y}_j - f(x_j, \mathbf{a})]. \tag{C.6}$$

where

$$V_{ij} = \frac{1}{N(N-1)} \sum_{s=1}^{N} (y_i^s - \overline{y}_i)(y_j^s - \overline{y}_j), \tag{C.7}$$

is the covariance matrix, which characterizes the correlations between the measured quantities.
By minimizing the $\chi^2$-functional with respect to the parameters we obtain the optimal values $\bar{a}_j$ for our parameters. If our data were uncorrelated, the covariance matrix would reduce to the diagonal matrix $V_{ij} = \delta_{ij} \frac{s_i^2}{N}$ and (C.6) to

$$\chi^2(\mathbf{a}) = \sum_{i=1}^{L} \frac{(\overline{y}_i - f(x_i, \mathbf{a}))^2}{\sigma_i^2}. \tag{C.8}$$

Here it is easy to see that the larger the error for a data point, the less weight it contributes to the functional.
Unfortunately, our data points are correlated due to the nature of the Monte Carlo updating algorithm. Therefore, we have to use (C.6) for our minimization procedure:

$$\left. \frac{\partial \chi^2}{\partial a_l} \right|_{\mathbf{a}=\bar{\mathbf{a}}} = 2 \sum_{i,j=1}^{L} \frac{\partial f(x_i, \bar{\mathbf{a}})}{\partial a_l} V_{ij}^{-1} [f(x_j, \bar{\mathbf{a}}) - \overline{y}_j] \tag{C.9}$$

$$\stackrel{!}{=} \quad 0 \tag{C.10}$$

This system of equations can be solved numerically, e.g. by Newton's method for root finding or the Levenberg-Marquardt algorithm.
Errors on secondary quantities are obtained by methods like *Jackknife* (see Sec. C.3) or *Bootstrap*.
To rate the confidence of our fit we have to consider the number of degrees of freedom, which is given by

$$\nu \quad = \quad L - n \tag{C.11}$$

For a reliable fit the ratio $\frac{\chi^2}{\nu}$ should be close to one:

$$\frac{\chi^2}{\nu} \quad \approx \quad 1 \tag{C.12}$$

## C.3 The Jackknife Method

An elegant way to estimate the errors of a secondary observable, obtained by fitting correlated data, is the *Jackknife method*. This is especially true if one does not have a large number of samples available.
*Single Elimination Jackknife* proceeds as follows:
Let us assume we have $N$ data points for a single quantity, for example the value of a correlator at a particular time. At the very first one creates $N$ *Jackknife subsamples*. This is done by making $N$ subsamples, each including $N-1$ data points, each time omitting a different one.
Hence, one can calculate the sample mean value for each subsample:

$$\overline{y}_s \quad = \quad \frac{1}{N-1} \sum_{\substack{i=1 \\ i \neq s}}^{N} y_i, \tag{C.13}$$

where $\overline{y}_s$ stands for the average of the subsample for which the $s$th data point has been left out.
If we have a data set of $L$ different quantities, we can perform a fit according to the previous section for each subsample; i. e., fitting the points

$$(x_{i,s}; \overline{y}_{i,s} \pm \sigma_{i,s}), \qquad i = 1, \ldots, L, \quad s = 1, \ldots, N. \tag{C.14}$$

Thereby we obtain $N$ so-called *Jackknife estimators* $\mathbf{a}_s$ of the secondary quantities.

Their average is

$$\overline{\mathbf{a}_{(J)}} = \frac{1}{N}\sum_{s=1}^{N}\mathbf{a}_s, \tag{C.15}$$

with the statistical variance

$$\sigma^2_{(J)} = \frac{N-1}{N}\sum_{s=1}^{N}\left(\mathbf{a}_s - \overline{\mathbf{a}_{(J)}}\right)^2. \tag{C.16}$$

A sensible estimator of the secondary quantity is then finally given by

$$\mathbf{a}_{(J)} = \overline{\mathbf{a}_{(J)}} \pm \sigma_{(J)}. \tag{C.17}$$

# Bibliography


[1] I. Lehmann [PANDA Collaboration], "Physics Programme of PANDA at FAIR," arXiv:0909.4237 [hep-ex].

[2] J. J. Aubert *et al.* [E598 Collaboration], "Experimental Observation Of A Heavy Particle J," Phys. Rev. Lett. **33**, 1404 (1974).

[3] J. E. Augustin *et al.* [SLAC-SP-017 Collaboration], "Discovery Of A Narrow Resonance In $e^* - e^-$-Annihilation," Phys. Rev. Lett. **33**, 1406 (1974).

[4] E. S. Swanson, "The New heavy mesons: A Status report," Phys. Rept. **429**, 243 (2006) [arXiv:hep-ph/0601110].

[5] N. Brambilla *et al.* [Quarkonium Working Group], "Heavy quarkonium physics," arXiv:hep-ph/0412158.

[6] P. Colangelo, F. De Fazio, R. Ferrandes and S. Nicotri, "New open and hidden charm spectroscopy," arXiv:hep-ph/0609240.

[7] T. Barnes and S. Godfrey, "Charmonium Options for the $X(3872)$," Phys. Rev. D **69** (2004) 054008.

[8] S. Godfrey and S. L. Olsen, "The Exotic $XYZ$ Charmonium-like Mesons," Ann. Rev. Nucl. Part. Sci. **58** (2008) 51.

[9] M. B. Voloshin, "Charmonium," Prog. Part. Nucl. Phys. **61**, 455 (2008) [arXiv:0711.4556 [hep-ph]].

[10] J. A. Appel, "Heavy-flavor production overview," Acta Phys. Polon. B **35**, 77 (2004) [arXiv:hep-ex/0311042].

[11] T. Matsui and H. Satz, "J/psi Suppression by Quark-Gluon Plasma Formation," Phys. Lett. B **178**, 416 (1986).

[12] G. S. Bali, "Charmonia from lattice QCD," Int. J. Mod. Phys. A **21**, 5610 (2006) [arXiv:hep-lat/0608004].

[13] P. Pascual and R. Tarrach, "QCD: Renormalization for the Practitioner," Springer-Verlag, (1984).

[14] M. E. Peskin and D. V. Schröder, "An Introduction to Quantum Field Theory," Westview Press, (1995).

[15] C. Itzykson and J. B. Zuber, "Quantum Field Theory," Dover Publication Inc; Dover Ed, (2006).

[16] B. Povh, K. Rith, C. Scholz, F. Zetsche, "Particles and Nuclei," Springer-Verlag, (2004).

[17] M. Gell-Mann, "The Eightfold Way: A Theory Of Strong Interaction Symmetry" (1961).

[18] R. D. Peccei and H. R. Quinn, "Constraints Imposed By CP Conservation In The Presence Of Instantons," Phys. Rev. D **16**, 1791 (1977).

[19] J. Goldstone, A. Salam and S. Weinberg, "Broken Symmetries," Phys. Rev. **127**, 965 (1962).

[20] H. Leutwyler, "On The Foundations Of Chiral Perturbation Theory," Annals Phys. **235**, 165 (1994) [arXiv:hep-ph/9311274].

[21] G. P. Lepage, L. Magnea, C. Nakhleh, U. Magnea and K. Hornbostel, "Improved nonrelativistic QCD for heavy quark physics," Phys. Rev. D **46**, 4052 (1992) [arXiv:hep-lat/9205007].

[22] A. G. Grozin, "Introduction to the heavy quark effective theory. I," arXiv:hep-ph/9908366.

[23] G. 't Hooft and M. J. G. Veltman, "Regularization And Renormalization Of Gauge Fields," Nucl. Phys. B **44**, 189 (1972).

[24] M. Creutz, "Quarks, Gluons and Lattices," Cambridge University Press, (1983).

[25] I. Montvay and G. Münster, "Quantum Fields on a Lattice," Cambridge University Press, (1994).

[26] C. Gattringer and C. B. Lang, "Quantum Chromodynamics on the Lattice (An Introductory Presentation)," Springer-Verlag, (2009).

[27] T. DeGrand and C. DeTar "Lattice Methods for Quantum Chromodynamics," World Scientific, (2007).

[28] K. G. Wilson, "Quarks And Strings On A Lattice," New Phenomena In Subnuclear Physics, Part A. Proceedings of the First Half of the 1975 International School of Subnuclear Physics, Erice, Sicily, July 11 -

August 1, 1975, ed. A. Zichichi, Plenum Press, New York, 1977, p. 69, CLNS-321.

[29] H. B. Nielsen and M. Ninomiya, "No Go Theorem For Regularizing Chiral Fermions," Phys. Lett. B **105**, 219 (1981).

[30] P. H. Ginsparg and K. G. Wilson, "A Remnant Of Chiral Symmetry On The Lattice," Phys. Rev. D **25**, 2649 (1982).

[31] R. Narayanan and H. Neuberger, "Chiral fermions on the lattice," Phys. Rev. Lett. **71**, 3251 (1993) [arXiv:hep-lat/9308011].

[32] R. Narayanan and H. Neuberger, "A Construction of lattice chiral gauge theories," Nucl. Phys. B **443**, 305 (1995) [arXiv:hep-th/9411108].

[33] M. Bochicchio, L. Maiani, G. Martinelli, G. C. Rossi and M. Testa, "Chiral Symmetry On The Lattice With Wilson Fermions," Nucl. Phys. B **262**, 331 (1985).

[34] K. G. Wilson, "Confinement Of Quarks," Phys. Rev. D **10**, 2445 (1974).

[35] G. Curci, P. Menotti and G. Paffuti, "Symanzik's Improved Lagrangian For Lattice Gauge Theory," Phys. Lett. B **130**, 205 (1983) [Erratum-ibid. B **135**, 516 (1984)].

[36] M. Lüscher and P. Weisz, "Computation Of The Action For On-Shell Improved Lattice Gauge Theories At Weak Coupling," Phys. Lett. B **158**, 250 (1985).

[37] D. B. Kaplan, "A Method for simulating chiral fermions on the lattice," Phys. Lett. B **288**, 342 (1992) [arXiv:hep-lat/9206013].

[38] Y. Shamir, "Chiral fermions from lattice boundaries," Nucl. Phys. B **406**, 90 (1993) [arXiv:hep-lat/9303005].

[39] J. B. Kogut and L. Susskind, "Hamiltonian Formulation Of Wilson's Lattice Gauge Theories," Phys. Rev. D **11**, 395 (1975).

[40] L. Susskind, "Lattice Fermions," Phys. Rev. D **16**, 3031 (1977).

[41] T. Banks, S. Raby, L. Susskind, J. B. Kogut, D. R. T. Jones, P. N. Scharbach and D. K. Sinclair, "Strong Coupling Calculations

Of The Hadron Spectrum Of Quantum Chromodynamics," Phys. Rev. D **15**, 1111 (1977).

[42] A. Bazavov *et al.* [The MILC Collaboration and The MILC Collaboration and The MILC Collabo], "MILC results for light pseudoscalars," PoS CD09, 007 (2009) [arXiv:0910.2966 [hep-ph]].

[43] C. W. Bernard *et al.* [MILC Collaboration], "Quenched Hadron Spectroscopy With Improved Staggered Quark Action," Phys. Rev. D **58**, 014503 (1998) [arXiv:hep-lat/9712010].

[44] C. Bernard, "Staggered chiral perturbation theory and the fourth-root trick," Phys. Rev. D **73**, 114503 (2006) [arXiv:hep-lat/0603011].

[45] M. Creutz, "Comment on "'t Hooft vertices, partial quenching, and rooted staggered QCD"," Phys. Rev. D **78**, 078501 (2008) [arXiv:0805.1350 [hep-lat]].

[46] C. Bernard, M. Golterman, Y. Shamir and S. R. Sharpe, "'t Hooft vertices, partial quenching, and rooted staggered QCD," Phys. Rev. D **77**, 114504 (2008) [arXiv:0711.0696 [hep-lat]].

[47] C. Gattringer, "A new approach to Ginsparg-Wilson fermions," Phys. Rev. D **63**, 114501 (2001) [arXiv:hep-lat/0003005].

[48] P. Hasenfratz, "Prospects for perfect actions," Nucl. Phys. Proc. Suppl. **63**, 53 (1998) [arXiv:hep-lat/9709110].

[49] T. Burch, K. Orginos and D. Toussaint, "Measurement of hybrid content of heavy quarkonia using lattice NRQCD," Phys. Rev. D **64**, 074505 (2001) [arXiv:hep-lat/0103025].

[50] T. Burch and C. Ehmann, "Couplings of hybrid operators to ground and excited states of bottomonia," Nucl. Phys. A **797**, 33 (2007) [arXiv:hep-lat/0701001].

[51] B. Sheikholeslami and R. Wohlert, "Improved Continuum Limit Lattice Action For QCD With Wilson Fermions," Nucl. Phys. B **259**, 572 (1985).

[52] K. Symanzik, "Continuum Limit And Improved Action In Lattice Theories. 1. Principles And Phi**4 Theory," Nucl. Phys. B **226**, 187 (1983).

[53] R. Sommer, "Non-perturbative QCD: Renormalization, O(a)-improvement and matching to heavy quark effective theory," arXiv:hep-lat/0611020.

[54] A. X. El-Khadra, A. S. Kronfeld and P. B. Mackenzie, "Massive Fermions in Lattice Gauge Theory," Phys. Rev. D **55**, 3933 (1997) [arXiv:hep-lat/9604004].

[55] S. A. Gottlieb, W. Liu, D. Toussaint, R. L. Renken and R. L. Sugar, "Hybrid Molecular Dynamics Algorithms for the Numerical Simulation of Quantum Chromodynamics," Phys. Rev. D **35**, 2531 (1987).

[56] N. Metropolis, A. W. Rosenbluth, M. N. Rosenbluth, A. H. Teller, E. Teller, "Equation of State Calculations by Fast Computing Machines," The Journal of Chemical Physics **21,6**, 1087 (1953).

[57] S. Duane and J. B. Kogut, "The Theory of Hybrid Stochastic Algorithms," Nucl. Phys. B **275**, 398 (1986).

[58] M. Hamermesh, "Group Theory and Its Application to Physical Problems," Dover Publications, (1989).

[59] X. Liao and T. Manke, "Excited charmonium spectrum from anisotropic lattices," arXiv:hep-lat/0210030.

[60] Y. Chen *et al.*, "The Sequential Empirical Bayes Method: An adaptive constrained-curve fitting algorithm for lattice QCD," arXiv:hep-lat/0405001.

[61] K. Sasaki, S. Sasaki, T. Hatsuda and M. Asakawa, "Excited nucleon spectrum from lattice QCD with maximum entropy method," Nucl. Phys. Proc. Suppl. **129**, 212 (2004) [arXiv:hep-lat/0309177].

[62] C. Michael, "Adjoint Sources In Lattice Gauge Theory," Nucl. Phys. B **259**, 58 (1985).

[63] M. Lüscher and U. Wolff, "How To Calculate The Elastic Scattering Matrix In Two-Dimensional Quantum Field Theories By Numerical Simulation," Nucl. Phys. B **339**, 222 (1990).

[64] G. S. Bali, H. Neff, T. Düssel, T. Lippert and K. Schilling [SESAM Collaboration], "Observation of string breaking in QCD," Phys. Rev. D **71**, 114513 (2005) [arXiv:hep-lat/0505012].

[65] J. J. Dudek, R. G. Edwards, M. J. Peardon, D. G. Richards and C. E. Thomas, "Highly excited and exotic meson spectrum from dynamical lattice QCD," arXiv:0909.0200 [hep-ph].

[66] T. Burch, C. Ehmann, C. Hagen, M. Hetzenegger and A. Schäfer, "Excited mesons on dynamical clover-Wilson lattices," PoS **LAT2007**, 103 (2007) [arXiv:0709.0664 [hep-lat]].

[67] T. Burch, C. Gattringer, L. Y. Glozman, C. Hagen, D. Hierl, C. B. Lang and A. Schäfer, "Excited hadrons on the lattice: Baryons," Phys. Rev. D **74**, 014504 (2006) [arXiv:hep-lat/0604019].

[68] B. Blossier, M. Della Morte, G. von Hippel, T. Mendes and R. Sommer, "On the generalized eigenvalue method for energies and matrix elements in lattice field theory," JHEP **0904** (2009) 094.

[69] T. Burch, C. Gattringer, L. Y. Glozman, C. Hagen and C. B. Lang, "Variational method for lattice spectroscopy with ghosts," Phys. Rev. D **73**, 017502 (2006) [arXiv:hep-lat/0511054].

[70] H. A. van der Vorst, "Templates for the Solution of Linear Systems: Building Blocks for Iterative Methods," SIAM, Philadelphia, (1994).

[71] H. A. van der Vorst, "Bi-CGSTAB: A fast and smoothly converging variant of Bi-CG for the solution of nonsymmetric linear systems," SIAM Journal on Scientific and Statistical Computing 13(2), 631 (1992).

[72] S. Dürr *et al.*, "Ab-Initio Determination of Light Hadron Masses," Science **322**, 1224 (2008) [arXiv:0906.3599 [hep-lat]].

[73] T. A. DeGrand, A. Hasenfratz and T. G. Kovacs, "Instantons and exceptional configurations with the clover action," Nucl. Phys. B **547**, 259 (1999) [arXiv:hep-lat/9810061].

[74] J. Foley, K. Jimmy Juge, A. O'Cais, M. Peardon, S. M. Ryan and J. I. Skullerud, "Practical all-to-all propagators for lattice QCD," Comput. Phys. Commun. **172**, 145 (2005) [arXiv:hep-lat/0505023].

[75] C. Michael and J. Peisa [UKQCD Collaboration], "Maximal variance reduction for stochastic propagators with applications to the static quark spectrum," Phys. Rev. D **58**, 034506 (1998) [arXiv:hep-lat/9802015].

[76] W. Wilcox, "Noise methods for flavor singlet quantities," arXiv:hep-lat/9911013.

[77] G. S. Bali, S. Collins and A. Schäfer, "Effective noise reduction techniques for disconnected loops in Lattice QCD," arXiv:0910.3970 [hep-lat].

[78] T. Burch and C. Hagen, "Domain decomposition improvement of quark propagator estimation," Comput. Phys. Commun. **176**, 137 (2007) [arXiv:hep-lat/0607029].

[79] C. Thron, S. J. Dong, K. F. Liu, H. P. Ying, "Padé-$Z2$ estimator of determinants," Phys. Rev. D **57**, 1642 (1998).

[80] S. Bernardson, P. McCarty and C. Thron, "Monte Carlo methods for estimating linear combinations of inverse matrix entries in lattice QCD," Comput. Phys. Commun. **78**, 256 (1993).

[81] A. O'Cais, K. J. Juge, M. J. Peardon, S. M. Ryan and J. I. Skullerud [TrinLat Collaboration], "Improving algorithms to compute all elements of the lattice quark propagator," arXiv:hep-lat/0409069.

[82] C. Ehmann and G. S. Bali, "$\eta'$-$\eta_c$-mixing with improved stochastic estimators," arXiv:0903.2947 [hep-lat].

[83] W. Wilcox, "Perturbative subtraction methods," Nucl. Phys. Proc. Suppl. **83**, 834 (2000) [arXiv:hep-lat/9908001].

[84] N. Mathur and S. J. Dong, "Study of stochastic estimates of quark loops with unbiased subtraction," Nucl. Phys. Proc. Suppl. **119**, 401 (2003) [arXiv:hep-lat/0209055].

[85] S. Collins, G. Bali and A. Schäfer, "Disconnected contributions to hadronic structure: a new method for stochastic noise reduction," PoS **LAT2007**, 141 (2007) [arXiv:0709.3217 [hep-lat]].

[86] S. Güsken, "A Study of smearing techniques for hadron correlation functions," Nucl. Phys. Proc. Suppl. **17**, 361 (1990).

[87] M. Albanese *et al.* [APE Collaboration], "Glueball Masses and String Tension in Lattice QCD," Phys. Lett. B **192**, 163 (1987).

[88] M. Teper, "An Improved Method for Lattice Glueball Calculations," Phys. Lett. B **183**, 345 (1987).

[89] A. Hasenfratz, R. Hoffmann and S. Schäfer, "Hypercubic Smeared Links for Dynamical Fermions," JHEP **0705**, 029 (2007) [arXiv:hep-lat/0702028].

[90] S. Perantonis and C. Michael, "Static potentials and hybrid mesons from pure SU(3) lattice gauge theory," Nucl. Phys. B **347**, 854 (1990).

[91] C. Amsler *et al.* [Particle Data Group], "Review of particle physics," Phys. Lett. B **667**, 1 (2008).

[92] J. J. Dudek, R. G. Edwards, N. Mathur and D. G. Richards, "Charmonium excited state spectrum in lattice QCD," Phys. Rev. D **77**, 034501 (2008) [arXiv:0707.4162 [hep-lat]].

[93] G. S. Bali and P. Boyle, "A lattice potential investigation of quark mass and volume dependence of the Upsilon spectrum," Phys. Rev. D **59**, 114504 (1999) [arXiv:hep-lat/9809180].

[94] P. de Forcrand *et al.* [QCD-TARO Collaboration], "Contribution of disconnected diagrams to the hyperfine splitting of charmonium," JHEP **0408**, 004 (2004) [arXiv:hep-lat/0404016].

[95] C. McNeile and C. Michael [UKQCD Collaboration], "An estimate of the flavour singlet contributions to the hyperfine splitting in charmonium," Phys. Rev. D **70**, 034506 (2004) [arXiv:hep-lat/0402012].

[96] L. Levkova and C. E. DeTar, "Contributions of charm anihilation to the hyperfine splitting in charmonium," arXiv:0809.5086 [hep-lat].

[97] T. Burch *et al.*, "Quarkonium mass splittings in three-flavor lattice QCD," arXiv:0912.2701 [hep-lat].

[98] N. Isgur and H. B. Thacker, "On the origin of the OZI rule in QCD," Phys. Rev. D **64**, 094507 (2001) [arXiv:hep-lat/0005006].

[99] C. McNeile and C. Michael [UKQCD Collaboration], "Mixing of scalar glueballs and flavour-singlet scalar mesons," Phys. Rev. D **63**, 114503 (2001) [arXiv:hep-lat/0010019].

[100] E. J. Eichten, K. Lane and C. Quigg, "New states above charm threshold," Phys. Rev. D **73**, 014014 (2006) [Erratum-ibid. D **73**, 079903 (2006)] [arXiv:hep-ph/0511179].

[101] `http://en.wikipedia.org/wiki/Pseudoscalar_meson`

[102] G. Bali and C. Ehmann, "Mixing of S-Wave Charmonia with $D\overline{D}$ Molecule States," arXiv:0911.1238 [hep-lat].

[103] T. W. Chiu and T. H. Hsieh [TWQCD Collaboration], "The spectrum of charmonium-like vector mesons in lattice QCD," PoS **LAT2006**, 170 (2007) [arXiv:hep-lat/0612025].

[104] S. Aoki *et al.* [CP-PACS Collaboration], "Lattice QCD Calculation of the $\rho$ Meson Decay Width," Phys. Rev. D **76**, 094506 (2007) [arXiv:0708.3705 [hep-lat]].

[105] A. Abulencia *et al.* [CDF Collaboration], "Analysis of the quantum numbers J(PC) of the X(3872)," Phys. Rev. Lett. **98**, 132002 (2007) [arXiv:hep-ex/0612053].

[106] V. M. Braun *et al.* [QCDSF Collaboration], "Nucleon distribution amplitudes and proton decay matrix elements on the lattice," Phys. Rev. D **79**, 034504 (2009) [arXiv:0811.2712 [hep-lat]].

[107] G. Beckett, B. Joó, C. M. Maynard, D. Pleiter, O. Tatebe and T. Yoshie, "Building the International Lattice Data Grid," arXiv:0910.1692 [hep-lat].

[108] C. E. DeTar, "Sharing lattices throughout the world: an ILDG status report," PoS **LAT2007**, 009 (2007) [arXiv:0710.1660 [hep-lat]].

[109] R. G. Edwards and B. Joó [SciDAC Collaboration and LHPC Collaboration and UKQCD Collaboration], "The Chroma software system for lattice QCD," Nucl. Phys. Proc. Suppl. **140**, 832 (2005) [arXiv:hep-lat/0409003].

[110] C. McClendon, "Optimized Lattice QCD Kernels for a Pentium 4 Cluster", Jlab preprint, JLAB-THY-01-29, `http://www.jlab.org/~edwards/qcdapi/reports/dslash_p4.pdf` (2001).

[111] A. Alexandrescu, "Modern C++ Design - Generic Programming and Design Patterns Applied," Addison-Wesley, (2006).

[112] P. A. Boyle *et al.*, "QCDoc: Project Status And First Results," J. Phys. Conf. Ser. **16**, 129 (2005).

[113] `http://www.fz-juelich.de/portal/index.php?index=163&cmd=show&mid=537`

[114] `http://www.physik.uni-regensburg.de/edv/linux/cluster_rz.phtml`

[115] P. A. Boyle, `http://www.ph.ed.ac.uk/ paboyle/bagel/Bagel.html` (2005).

[116] `http://www.top500.org`

[117] L. Lyons, "A practical guide to data analysis for physical science students," Cambridge University Press, Cambridge (1991).

*Do not fear death so much, but rather the inadequate life.* – *The Mother.*

Berthold Brecht

# Acknowledgements

The first person to mention here is my advisor Prof. Dr. Gunnar Bali.
I rarely encountered someone with such creative talent and profound knowledge in the broad field of physics. His open and uncomplicated manner lead to an unreserved relationship and a very pleasant atmosphere within our group. I appreciate his useful suggestions, both from the physical and technical viewpoint. Furthermore I want to thank him for providing me the opportunity to report on the progress of my research all over the world by allowing me to attend the annual Lattice conferences and Quarkonium Working Group workshops, which took me to some very interesting places.
I am also very grateful to the other professors of our group, namely Prof. Dr. Vladimir Braun, Prof. Dr. Andreas Schäfer and Prof. Dr. Tilo Wettig, amongst many other things for giving excellent introductory lectures on quantum field theory and its applications. Through their unquestionable competence and ambition, they managed to land the Sonderforschungsbereich SFB/TR55 "Hadron Physics from Lattice QCD" for Regensburg, in cooperation with Bern, Graz and Wuppertal, which discloses many new opportunities to our group.
I am very much indebted to two people who mainly taught me the fundamental tools for Lattice QCD calculations. At first I want to allude to my advisor for my diploma thesis, Dr. Tommy Burch. I admire his longstanding patience when answering my numerous stupid questions and his pedagogic ability to explain complicated issues. He is an expert in his field and I was lucky to be able to benefit from this. The very same gratitude I owe to Dr. Christian Hagen for fruitful discussions of physical ideas and their implementation on computers. His stamina was amazing, since he was the only guy (at least I know) being at his office from eight in the morning till eight in the evening five (six) days a week.
I thank Dr. Sara Collins for her advises and support in both conceptual and practical subjects.

Dr. Jürgen Rohrwild refreshed my sometimes fading theoretical fundament of QCD. I also thank him for the distraction from the daily work by wipping me out in uneven chess matches.
Many thanks go to my roommates Dr. Franceso Hautmann, Dr. Dieter Hierl, Martin Hetzenegger and Johannes Najjar for a relaxed social intercourse and enjoyable conversations, the last three also for the collegial teamwork to keep the computer systems running.
The kind souls of our working group, Monika Maschek and Heidi Decock, toke care of all administrative issues and were never at a loss for a helpful hand.
Although the hitherto part of the thesis was challenging, the next lines seem to be the hardest ones for me.
I want to dedicate this work to my mother, who sadly left us much too early. After long illness, she passed away in October 2009. But sometimes death comes as a release. I cannot thank her enough for the love and and care she gave to me. She deserves all admiration for managing dialy life without lament while suffering from her disease. If all people were nearly pleasant and upright as she was, the world would be a much better place.
The other person I owe so much to is my father. I think he knows what he means to me and how much I appreciate his nurture, allowing me to bear a charmed life.
I am very proud of my brother Detlef, who never got tired of asking about the progress of my work.
Special thanks to all my friends for making live outside physics exciting and pleasureable.
Last but not least I want to thank my girlfriend Stefanie for her love and support, both in good and bad times.